GEOPHYSICAL SURVEY OF MDA-B WASTE DISPOSAL SITE
AT DP MESA, LOS ALAMOS, NM

APPROVED BY SUPERVISORY COMMITTEE:

John F. Ferguson, Chair

Robert J. Stern

Thomas H. Brikowski

10772

GEOPHYSICAL SURVEY OF MDA-B WASTE DISPOSAL SITE AT DP MESA, LOS ALAMOS, NM

By

Ioannis Thavoris

THESIS

Presented to the Faculty of

The University of Texas at Dallas

in Partial Fulfillment

of the Requirements

for the Degree of

MASTER OF SCIENCE IN GEOSCIENCES

THE UNIVERSITY OF TEXAS AT DALLAS

August, 2001

UNIVERSITY OF TEXAS AT DALLAS

Date: Aug 2001

Author: Ioannis Thavoris

Title: GEOPHYSICAL SURVEY OF MDA-B WASTE DISPOSAL SITE AT DP MESA, LOS ALAMOS, NM

Department: Geosciences

Degree: M.Sc. Convocation: Aug Year: 2001

Permission is herewith granted to University of Texas at Dallas to circulate and to have copied for non-commercial purposes, at its discretion, the above title upon the request of individuals or institutions.

Signature of Author

THE AUTHOR RESERVES OTHER PUBLICATION RIGHTS, AND NEITHER THE THESIS NOR EXTENSIVE EXTRACTS FROM IT MAY BE PRINTED OR OTHERWISE REPRODUCED WITHOUT THE AUTHOR'S WRITTEN PERMISSION.

THE AUTHOR ATTESTS THAT PERMISSION HAS BEEN OBTAINED FOR THE USE OF ANY COPYRIGHTED MATERIAL APPEARING IN THIS THESIS (OTHER THAN BRIEF EXCERPTS REQUIRING ONLY PROPER ACKNOWLEDGEMENT IN SCHOLARLY WRITING) AND THAT ALL SUCH USE IS CLEARLY ACKNOWLEDGED.

Στή μνήμη τοῦ

παπποῦ μου

Ἰωάννη Θαβώρη.

-

Στήν οικογένειά μου.

ACKNOWLEDGEMENTS

I wish first to thank Dr. John Ferguson, my supervisor, for suggesting this project, for his guidance during my graduate studies, and for his contribution, especially through the development of the seismic refraction modeling codes. Overall, I express my gratitude to the department of Geosciences for the financial support while I have been in UTD. I am also grateful to the members of my committee, Dr. Thomas Brikowski and Dr. Robert Stern, and to Professor George McMechan. Dr. Brikowski, was especially helpful with his final review of this work. I would like to express my appreciation to all the people involved during the acquisition of the data, at SAGE and Los Alamos.

I am grateful to Los Alamos National Laboratory (LANL) and specifically to Dr. W. Scott Baldridge, which contributed significantly to this research, providing along with environmental and geologic information, financial support as well.

I want to take this chance to thank two exceptional personalities. Dr. Basilios Papazachos, Professor in Aristotle University of Thessaloniki, and Dr. Gregory Tsokas Associate Professor at the same school, who first suggested and motivated me to continue my studies originally to that school.

Lastly, as usual, but most important, I want to thank my family, my parents Kimon, and Maria, my sisters Athena and Anna, and my uncles George Thavoris and Mark Katliakas, for their continuous encouragement and support.

Table of Contents

Table of Contents v

List of Tables vii

List of Figures viii

Abstract xii

1 Introduction 1

2 Background of the Studied Area 3
- 2.1 Site History and Description 3
- 2.2 Geology 6

3 Previous Geophysical Surveys 14

4 The Seismic Refraction Method 19
- 4.1 Refraction Traveltime Curves and Raypaths 20

5 Seismic Survey of MDA-B Site 24
- 5.1 Methodology 24
- 5.2 Survey Configuration: Selection of Seismic Lines and Data Acquisition 25
- 5.3 Seismic Noise and Picking of the first arrivals 28
  - 5.3.1 The Picking process 31

6 The Magnetic Method 34
- 6.1 The general magnetic interpretation problem 35
  - 6.1.1 Depth estimation of the magnetic bodies 37
  - 6.1.2 Anomaly of the trenches 38
- 6.2 The Magnetic Survey at MDA-B 39

6.2.1 Eastern Paved Area 40
6.2.2 Western Paved Area 48
6.2.3 L-Shaped Area 53
6.2.4 Eastern Unpaved Area 53
6.3 Magnetic Modeling Method 55
6.3.1 The modeling program 59

7 Seismic Modeling **61**

8 Interpretation **63**
8.1 The Magnetic data 63
8.1.1 Eastern Paved Area 63
8.1.2 Western paved Area 64
8.1.3 Eastern Unpaved Area 70
8.2 The Seismic data 75
8.2.1 Eastern Unpaved Area 76
8.2.2 Eastern Paved Area 78
8.2.3 Western Paved Area 92
8.2.4 Western Unpaved Area 102

9 Conclusions and Recommendations **105**

A Matlab code **120**

Bibliography **123**

List of Tables

8.1 Velocity model for line 8 79
8.2 Velocity model for seismic line 9. 79
8.3 Velocity model for line 10 79
8.4 Velocity model for line 11 80
8.5 Velocity model for line 13 80
8.6 Velocity model for line 14 80
8.7 Velocity model for line 15 80
8.8 Velocity model for line 16 81
8.9 Velocity model for line 18 81
8.10 Velocity model for line 28 94
8.11 Velocity model for line 7 94
8.12 Velocity model for line 27 94
8.13 Velocity model for line 26 95
8.14 Velocity model for line 25 95
8.15 Velocity model for line 24 95
8.16 Velocity model for line 23 102
8.17 Velocity model for line 22 102

9.1 Synopsis of trenches dimensions 111

List of Figures

2.1 General Map of TA-21 4

2.2 Aerial view of the TA-21 parcel and the MDA-B site, 1995. 5

2.3 Aerial view of excavated trench in 1947 after a snowfall. 7

2.4 Map of MDA-B showing possible layout of disposal beds and proposal locations of boreholes and surface samples. 8

2.5 Plan view and cross-section of study site in Area B. 9

2.6 Experimental site in eastern MDA-B without the latest cover. 10

2.7 Geological cross section at MDA-B, TA-21 11

2.8 Geologic map of MDA-B vicinity 13

3.1 Seismic lines 1-6 at MDA-B, SAGE 1997. 15

3.2 Magnetic Map at MDA-B, SAGE 1997. 16

3.3 Electromagnetic Map at MDA-B, BGA 1997. 17

4.1 Wavefront extrapolation using the Schneider's algorithm. 21

4.2 Ambiguities in seismic refraction method. 22

5.1 Configuration of seismic lines 26

5.2 Asphalt effect and airwave coupling. 28

5.2 (Con't) Asphalt effect and airwave coupling 29

5.3 Local velocity inversion because of the asphalt presence. 33

6.1 Calculation of the magnetic anomaly of an arbitrary shaped body . . 36

6.2 Magnetic anomaly at Eastern Paved Area. 41

6.3 Spectrum of Magnetic anomaly at EPA. 43
6.4 FIR bandpass filter implementation for EPA. Inpulse and frequency responses. 44
6.5 Filtered magnetic anomaly and its residual at EPA. 45
6.5 (Con't) Filtered magnetic anomaly and its residual at EPA. 46
6.6 Magnetic anomalies at EPA. 47
6.7 Upward continuation 2.5 ft of reduced to the pole magnetic anomaly at EPA. 48
6.8 Magnetic anomaly at Western Paved Area. 49
6.9 Spectrum of magnetic anomaly at WPA. 50
6.10 Upward continuation 8.2 ft of reduced to the pole magnetic anomaly at WPA. 51
6.11 Bandpass (25-40 ft) filtered anomaly at WPA. 52
6.12 Magnetic anomaly at LSA (-51500 nT). 54
6.13 Magnetic anomaly at Eastern Unpaved Area (-51500 nT). 56
6.14 Spectrum of magnetic anomaly at EUA. 57
6.15 Filtered map of magnetic anomaly at EUA. 58

8.1 Magnetic profiles along WPA. (see Fig. 6.8 for profile location) 65
8.1 (cont) Magnetic profiles along WPA. 66
8.2 Second derivative of magnetic field at WPA. This high pass filter emphasizes shallow sources and delineates their boundaries. 67
8.3 Filtered map (5-30ft) of magnetic field at WPA. 68
8.4 Residual of the previous filtered map [0 5) & (30 $+\infty$) ft, at WPA. . 69
8.5 Observed anomaly (4) at WPA. 71
8.6 Modeled anomaly (4) at WPA 72
8.7 Observed anomaly (E) at EUA. 73
8.8 Modeled anomaly (E) at EUA 74
8.9 Travel times (red symbol observed, blue line computed), and corresponding model for line 19. 77

8.10 Travel times (red symbol observed, blue line computed), and corresponding model for line 8. 82
8.11 Travel times (red symbol observed, blue line computed), and corresponding model for line 9. 83
8.12 Travel times (red symbol observed, blue line computed), and corresponding model for line 10. 84
8.13 Travel times (red symbol observed, blue line computed), and corresponding model for line 11. 85
8.14 Travel times (red symbol observed, blue line computed), and corresponding model for line 13. 86
8.15 Travel times (red symbol observed, blue line computed), and corresponding model for line 14. 87
8.16 Travel times (red symbol observed, blue line computed), and corresponding model for line 15. 88
8.17 Travel times (red symbol observed, blue line computed), and corresponding model for line 15r. 89
8.18 Travel times (red symbol observed, blue line computed), and corresponding model for line 16. 90
8.19 Travel times (red symbol observed, blue line computed), and corresponding model for line 18. 91
8.20 Travel times (red symbol observed, blue line computed), and corresponding model for line 28. 96
8.21 Travel times (red symbol observed, blue line computed), and corresponding model for line 7. 97
8.22 Travel times (red symbol observed, blue line computed), and corresponding model for line 27. 98
8.23 Travel times (red symbol observed, blue line computed), and corresponding model for line 26. 99

8.24 Travel times (red symbol observed, blue line computed), and corresponding model for line 25. 100
8.25 Travel times (red symbol observed, blue line computed), and corresponding model for line 24. 101
8.26 Travel times (red symbol observed, blue line computed), and corresponding model for line 23. 103
8.27 Travel times (red symbol observed, blue line computed), and corresponding model for line 22. 104

9.1 Magnetic model for magnetic anomaly E. (See also Fig 6.13) 107
9.2 Wood boxes, drums and access tubes for monitoring in Pit 8, area G. 108
9.3 Interpreted seismic model for EPA. 109
9.4 Magnetic model for magnetic anomaly 4. 110
9.5 Interpreted seismic model for WPA. 112
9.6 Interpreted seismic model for Eastern end WPA and WUA. 113
9.7 Fence diagram of the seismic models at MDA-B (Lines 7-29) 114
9.8 BGA interpretation of the trench boundary for MDA-B. Source: BGA report, 1998. 115
9.9 Final interpretation of the trench boundaries for MDA-B. 118
9.10 Three dimensional prospective view of the trench boundaries for MDA-B.119

Abstract

Several sites have been used at Los Alamos National Laboratory, NM, for the disposal of a variety of hazardous substances, both radioactive and chemical, which now require characterization and potential remediation. Documentation of some of the older sites was poor, and it was necessary to use geophysical techniques to define the locations and extent of these sites. Seismic refraction and magnetic methods were utilized to map these hazardous chemical and radioactive disposal areas in Material Disposal Area B (MDA-B) at Technical Area 21 (TA-21) at the Los Alamos National Laboratory. In order to map these trench sites, known to exist in the area, a new methodology for determining shallow local heterogeneities using the seismic refraction method was applied. The method is based on high-resolution surveys and forward modeling by polygonal bodies.

A multiple ash-flow sheet that forms the prominent cliffs at the Technical area 21, hosts the disposal trenches and paleochannels, which are now covered by top-soil and alluvial material. An existing total-field magnetic map provided a general guide to areas where magnetic material is present. Both seismic refraction and magnetic surveys, as well as electromagnetic investigations in these sites were used to reconstruct the geometry of Material disposal Area B (MDA-B), providing indispensable information for the environmental fate of the area.

The Los Alamos National Laboratory (LANL) contributed significantly to this research, providing along with environmental and geologic information, financial support as well.

Chapter 1

Introduction

Los Alamos National Laboratory at New Mexico (LANL) has been the site for radioactive material research for almost sixty years. Starting with the Manhattan Project, a mainly weapons-oriented program for nuclear explosive devices, and continuing with nuclear research in the post-World-War-II period, LANL has been a significant source of nuclear waste products. Technical Area 21 (TA-21) was used for plutonium research and production from 1945 to 1978 (Rogers, 1977). Weapons production, nuclear power research, and marine power production were the main government-sponsored activities generating radioactive waste (Nyhan and Barnes, 1989). In 1977, Rogers prepared a comprehensive report aiming to provide a readily available source of accurate, in depth information for reference by LANL personnel. According to Rogers, *"...the desire to determine the environmental impact of solid waste disposal forced to the re-examination of the concept of land burial as a means of permanent disposal..."*. For that purpose an evaluation of site monitoring practices has been in progress since September 1973, including Material Disposal Area B (MDA-B) at Technical Area-21 (TA-21) (Rogers, 1977; Nyhan and Barnes, 1989).

Existing information concerning the TA-21 site given in the Rogers report were without any further evaluation or certification of validity. All sources were presented, despite apparent contradictions, in hopes that bias would be minimized. Rogers recommended that the individual pits and shafts within each area should be clearly identified. Nyhan and Barnes (Nyhan and Barnes, 1989) came to the conclusion that future field research and hydrologic modeling in MDA-B is necessary. Since then, extended and detailed geological and hydrological studies had been conducted at TA-21, aiming to improve the exchange of information among scientists working at different fields by providing a common framework for discussing the influence of local geology and hydrology on contaminant transport. The need for locating and mapping accurately the disposal sites is imperative. At this time, there is a concern that waste trenches may be hydrologically connected to the modern streams. The uncertainty concerning environmental risk affects all facets of LANL's decision making process, whether it involves deciding on the best method of treatment or operation to reduce the chances of environmental impairment. The main purpose of this project was to find and reconstruct the geometry of all burial trenches in MBA-B using geophysical techniques, taking care at the same time not to interfere with the waste and disturb the hydrological balance. Previous work of the SAGE field course 1995-1997, (Pope et al., 1996; Ferguson et al., 1998; Smith and Ferguson, 2000) revealed that the seismic refraction method could provide safe and cost-effective ways of locating and delineating the trench sites. During the SAGE field course in 1998, and over a two week period afterward, additional seismic refraction data were obtained and a complete magnetic map (Plate I) of the site was made (Ferguson et al., 1998). Magnetic mapping, could in addition locate concentrations of buried ferrous material dispersed among the other waste products. The data will be interpreted and recommendations made concerning the location of the waste trenches at MDA-B.

Chapter 2

Background of the Studied Area

The area under investigation is a part of the Technical Area-21 (TA-21) of the Los Alamos National Laboratory. Geographically TA-21 is located on DP Mesa, part of the Pajarito Plateau between the White Rock Canyon of the Rio Grande on the east, and the Jemez Mountains to the west. TA-21 is on the eastern edge of Los Alamos, NM (Fig. 2.1), and served as a plutonium processing facility from 1945 to 1978.

2.1 Site History and Description

At an elevation of about 7140 ft, TA-21 centers on DP Mesa and sits in between two adjacent canyons; Los Alamos Canyon to the south and DP Canyon to the north (Fig. 2.2). From 1945 until the 1978 several disposal areas were excavated, where contaminated equipment, process residues, toxic, and corrosive chemicals, and other hazardous radioactive wastes were buried in shallow trenches or isolated shafts (Broxton and Eller, 1995).

Material Disposal Area B (MDA-B) is the largest solid waste disposal site, and

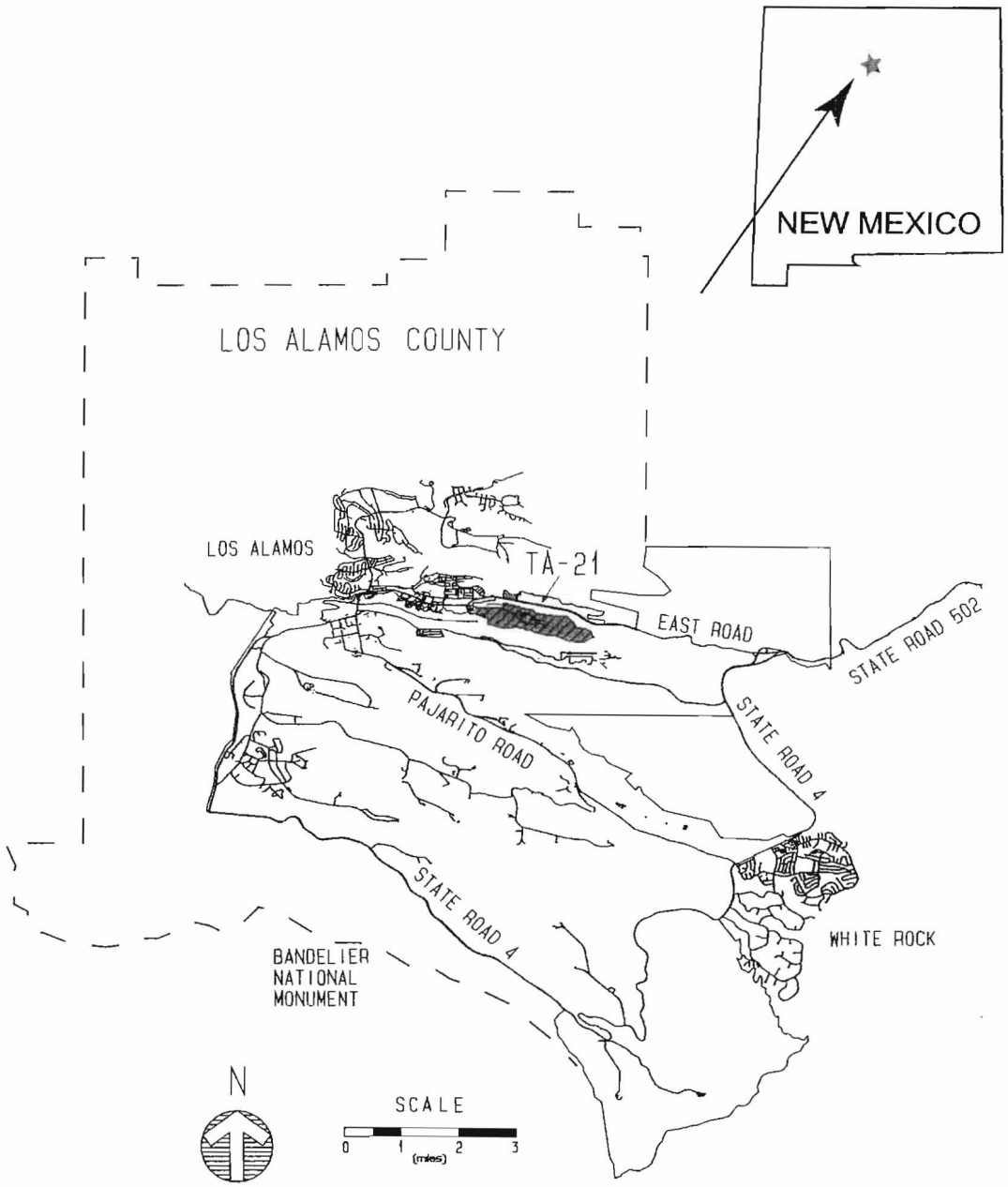

Figure 2.1: General map of Los Alamos, NM and the location of TA-21. (Source: http://www.lanl.gov)

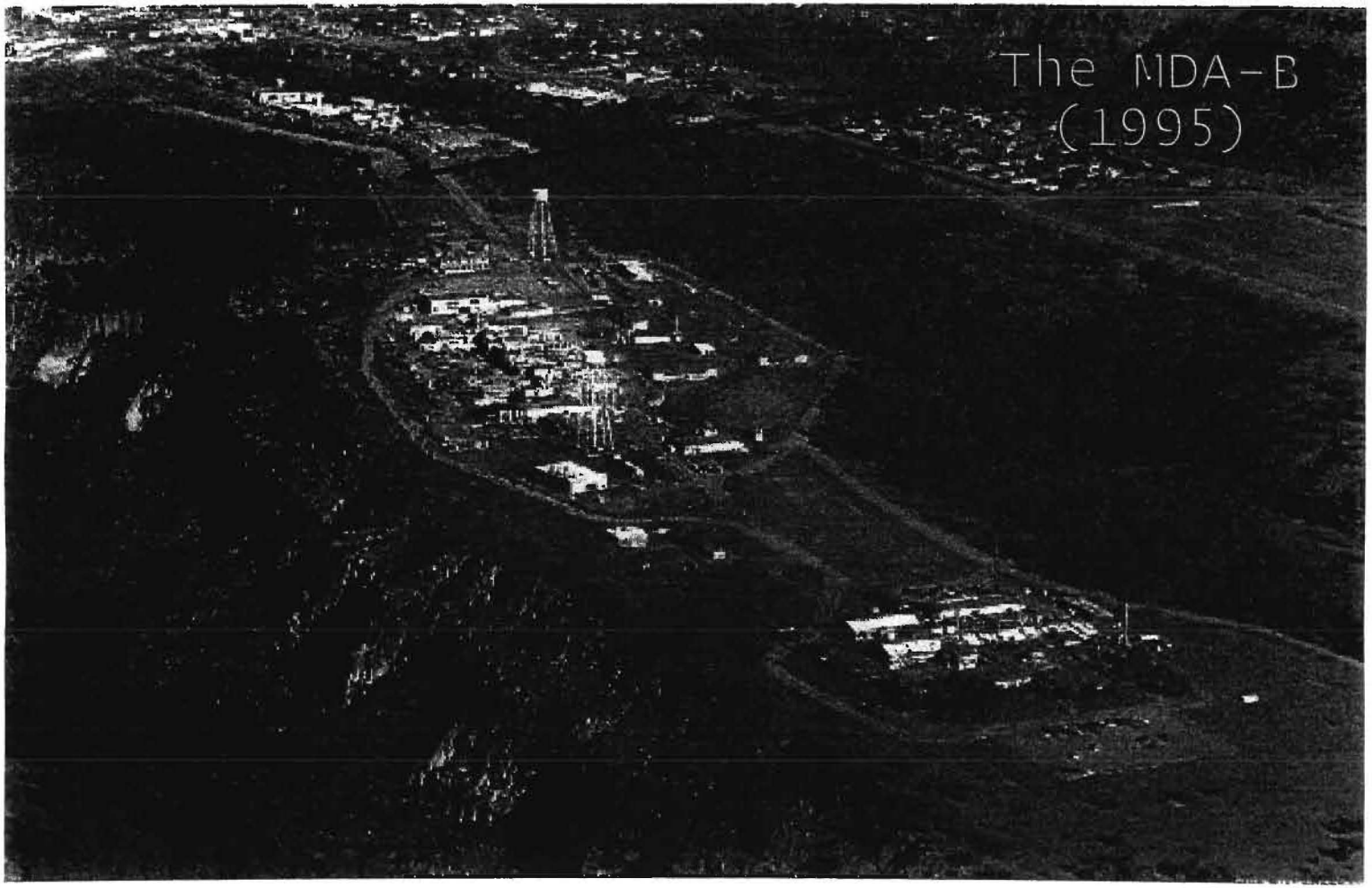

Figure 2.2: West facing aerial view of the TA-21 parcel and the MDA-B site, 1995. Note the airport location in the upper right. (Source: http://www.lanl.gov)

was probably the first solid waste burial ground for the laboratory. It was operated as a disposal site from 1945 until 1950, with available records only after 1947 through the closing of the area (Rogers, 1977). Old records indicate that MDA-B is actually a series of pits (Fig. 2.3). They were excavated between 1945 and 1948. The pits were most likely cut in unit 3a of the Tshirege Member of the Bandelier tuff. Until this thesis research was done, the location and the number of them were unclear (Fig. 2.4).In 1966, at the proposal of LANL (then called Los Alamos Scientific Laboratory) and the Atomic Energy Commission the western two-thirds of the Area B (outside the radius of 1050 ft from TA-21) were leveled, filled where was necessary, and sealed with asphalt (Purtymun and Kennedy, 1966). The area was used for many years as community vehicle and trailer storage facility. In the 1980s, experimental caps of rock and soil were emplaced in the eastern (unpaved) portion of MBA-B (Nyhan and Barnes, 1989; Nyhan et al., 1986)(Figs. 2.5 and 2.6). The experiments are no longer active at MDA-B as of May 1997. At Material Disposal Area T (MDA-T) four absorption beds, receiving untreated and treated wastes, were constructed in 1945. Later on, disposal shafts were established between the absorption beds. There is evidence that a paleochannel runs through this area.

2.2 Geology

In order to place the local geology in perspective, this study commences with a discussion of formal stratigraphy followed by a brief discussion of the structural and neo-tectonic setting of the site, and its implications for the geophysical methods to be used.

Extensive geologic work has been done at TA-21. Smith and Bailey (Smith

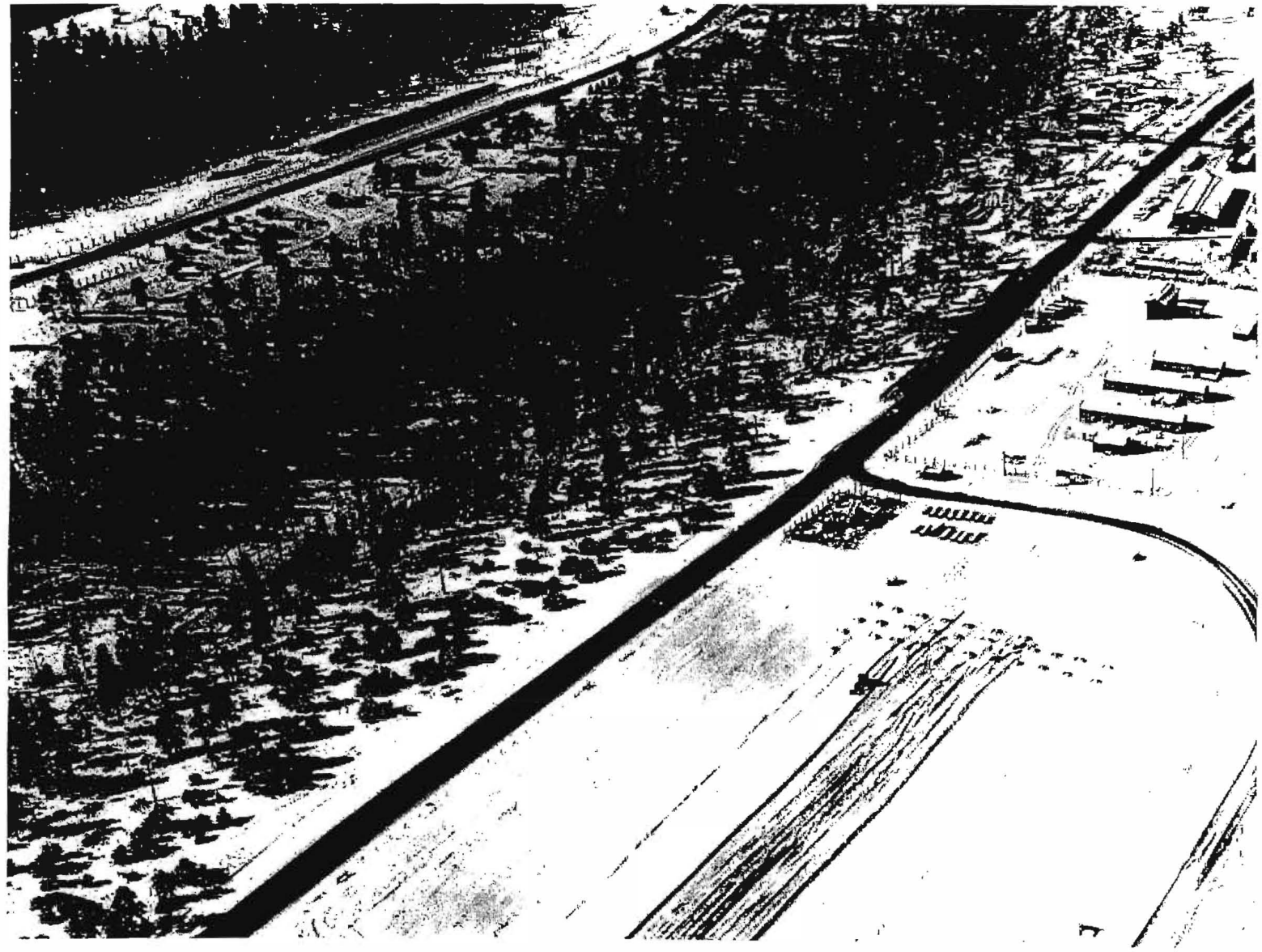

Figure 2.3: Aerial view looking west of excavated trench in 1947 (upper left), and portion of the Los Alamos airport (lower right) after a snowfall. See Fig. 2.2 for a more recent view(Source: Pope, P. 1997, personal communication)

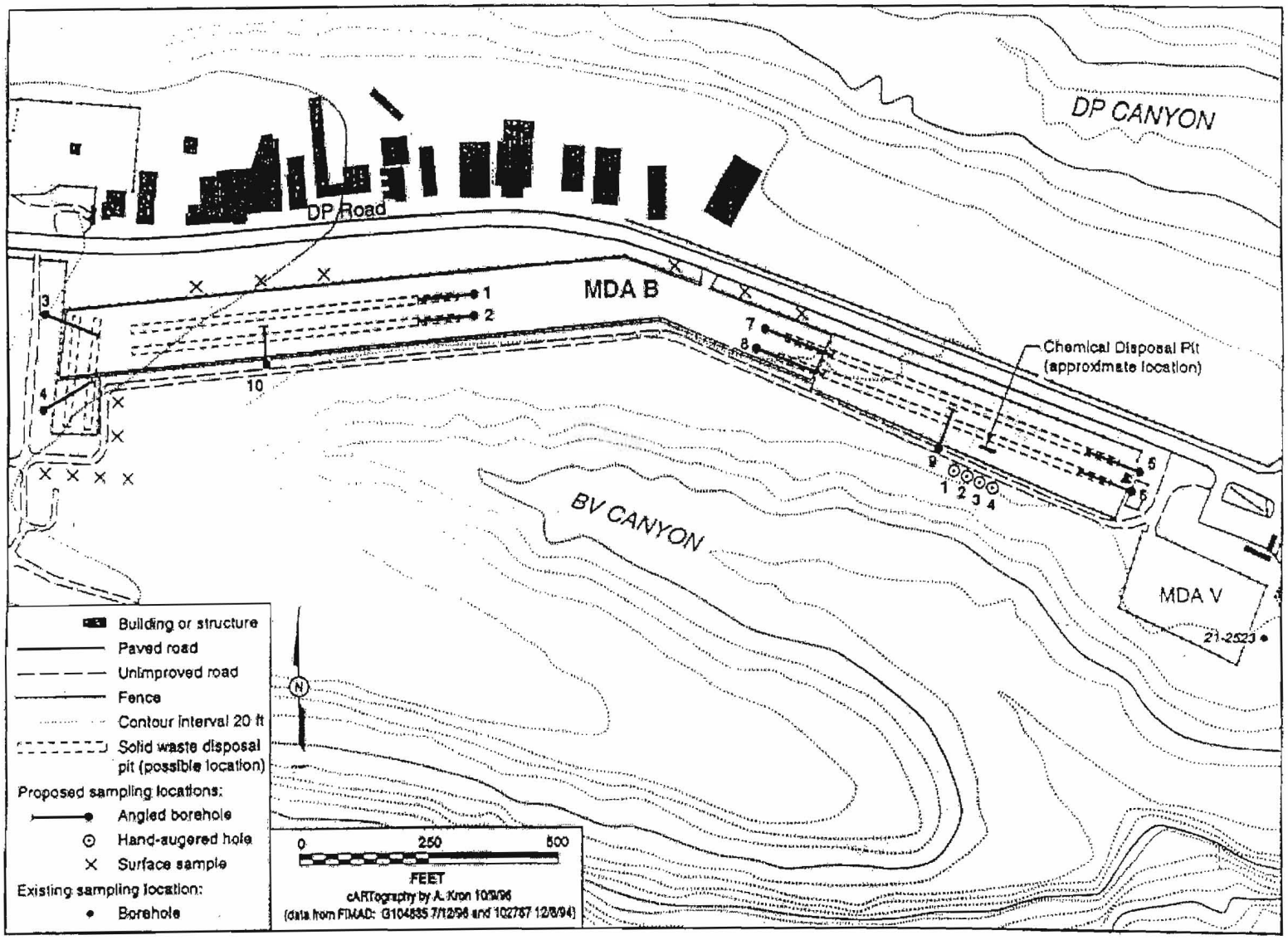

Figure 2.4: Map of MDA-B showing possible layout of disposal beds and proposal locations of boreholes and surface samples. (Source: LANL, Sampling Plan for MDA-B 1996, internal documentation)

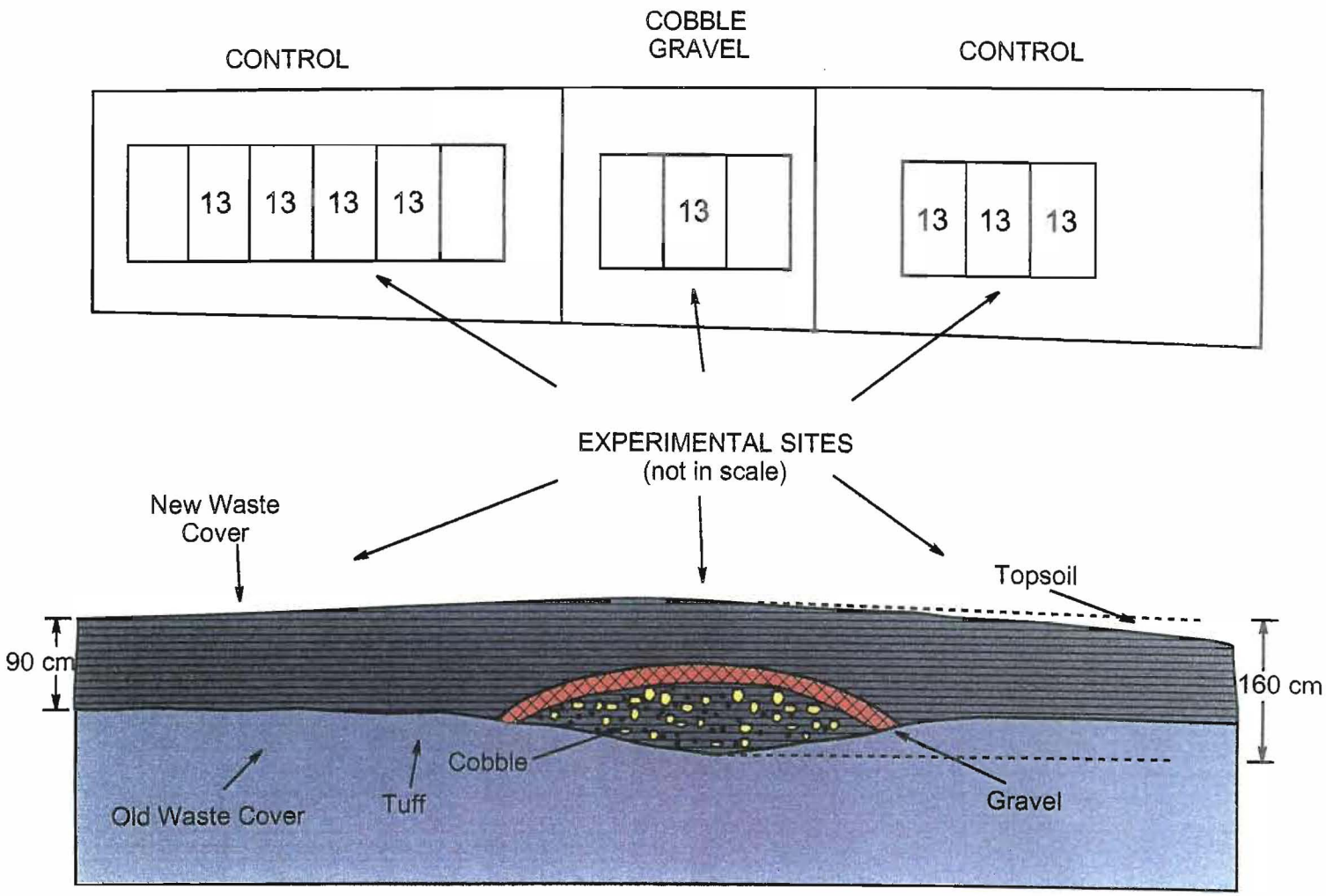

Figure 2.5: Plan view and cross-section of study site in the Eastern Part of Area B. (After Nyhan et al., 1996)

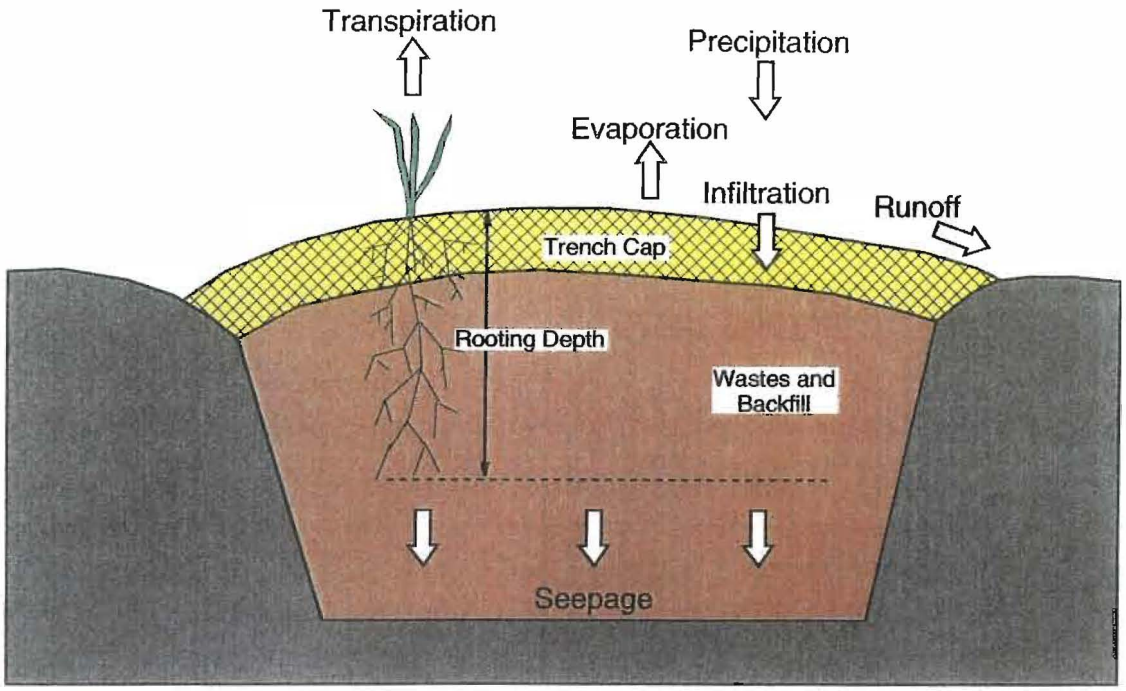

Figure 2.6: Experimental site in eastern MDA-B without the latest cover. (After Nyhan et al., 1996)

and Bailey, 1966), studied the ash-flow tuffs (Bandelier tuff) erupted in two climactic pyroclastic outbursts from the Valles caldera of the Jemez volcanic field. A succession of cliff-forming ash flows,(Fig. 2.7) including the 1.22 Ma old Tshirege Member (Izett and Obradovich, 1994) of the Bandelier tuff -a rhyolitic deposit which dominates on the whole Pajarito Plateau (Goff, 1995) - as well as the older Otowi member, a massive pumiceous breccia (air fall) compose the main bedrock geology of the TA-21 (Broxton et al., 1995). The Tshirege Member is a compound cooling unit divided into four distinct units. Following Tshirege deposition, a system of streams was incised into the tuff, forming a braided pattern as they traversed the plateau (Reneau, 1995).

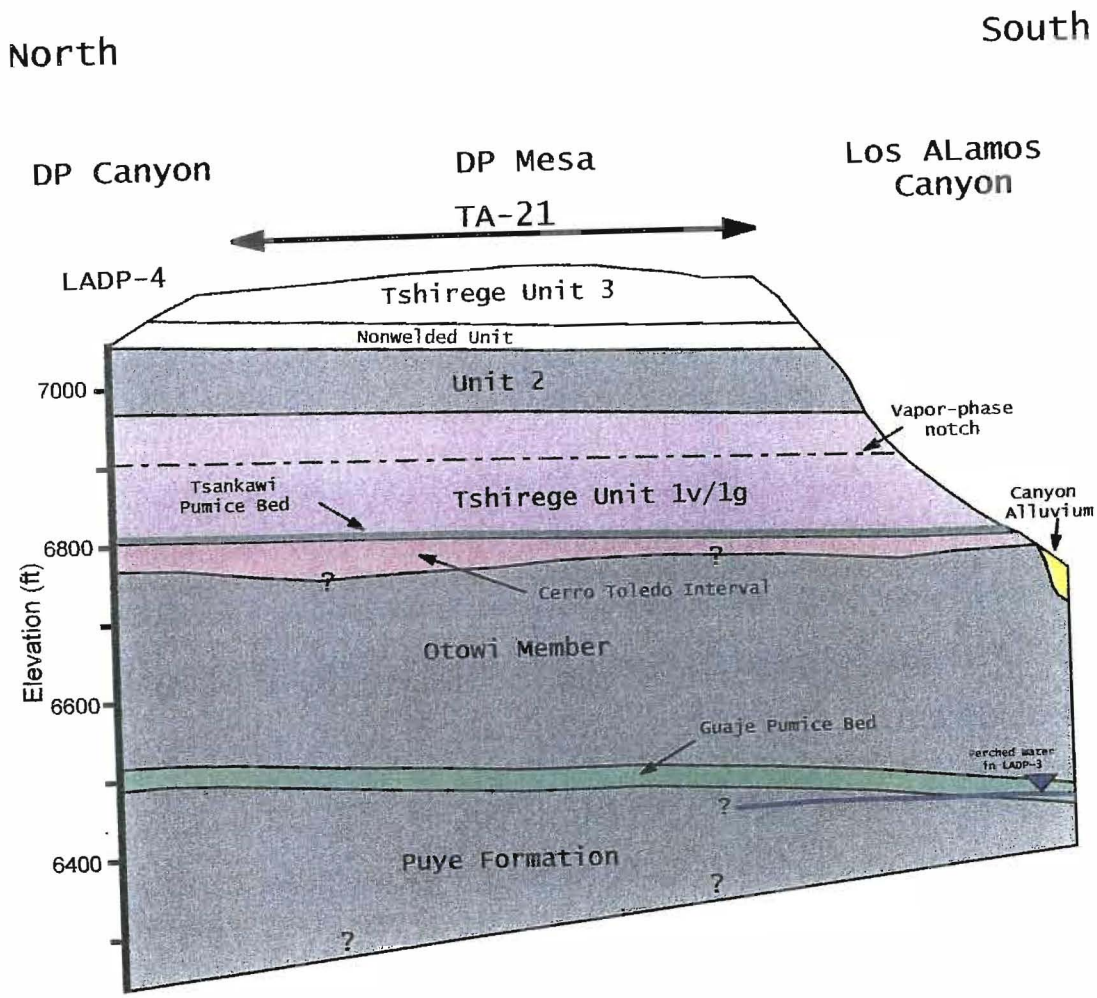

Figure 2.7: Geological cross section at MDA-B, TA-21. (After Broxton et al., 1995)

However at TA-21 the Unit 3 is also the caprock unit; it is further subdivided into the lower slope forming tuffs and the upper cliff-forming tuffs with a gradational boundary in between. Unit 3 is partially to moderately welded with the top 10 m non-welded, thus accelerating the weathering process of this portion of the cliff. The sequence is now covered with post-Bandelier mesa topsoil and alluvium and in some places civilian structures (Fig. 2.8).

Measurements and analysis of rock fractures indicate a notable increase in fracture density through Material Disposal Area V of TA-21. The ashflows of the Bandelier Tuff are broken into blocks formed by shrinkage joints as the ashflow cooled (Rogers, 1977; Broxton et al., 1995). These joints are more numerous within the welded part of the tuff. In general, fractures in the TA-21 area make up a conjugate set of NW and NE strikes (Wohletz, 1995). According to Broxton and Reneau (Reneau, 1995; Broxton et al., 1995) clay and tuff detritus fills the near surface fractures. The tuff is exposed on the canyon rims and a general cover of post-Bandelier talus and colluvium debris from the underlying cliffs of Unit 3 covers the outcrops of the non-welded tuff in central areas.

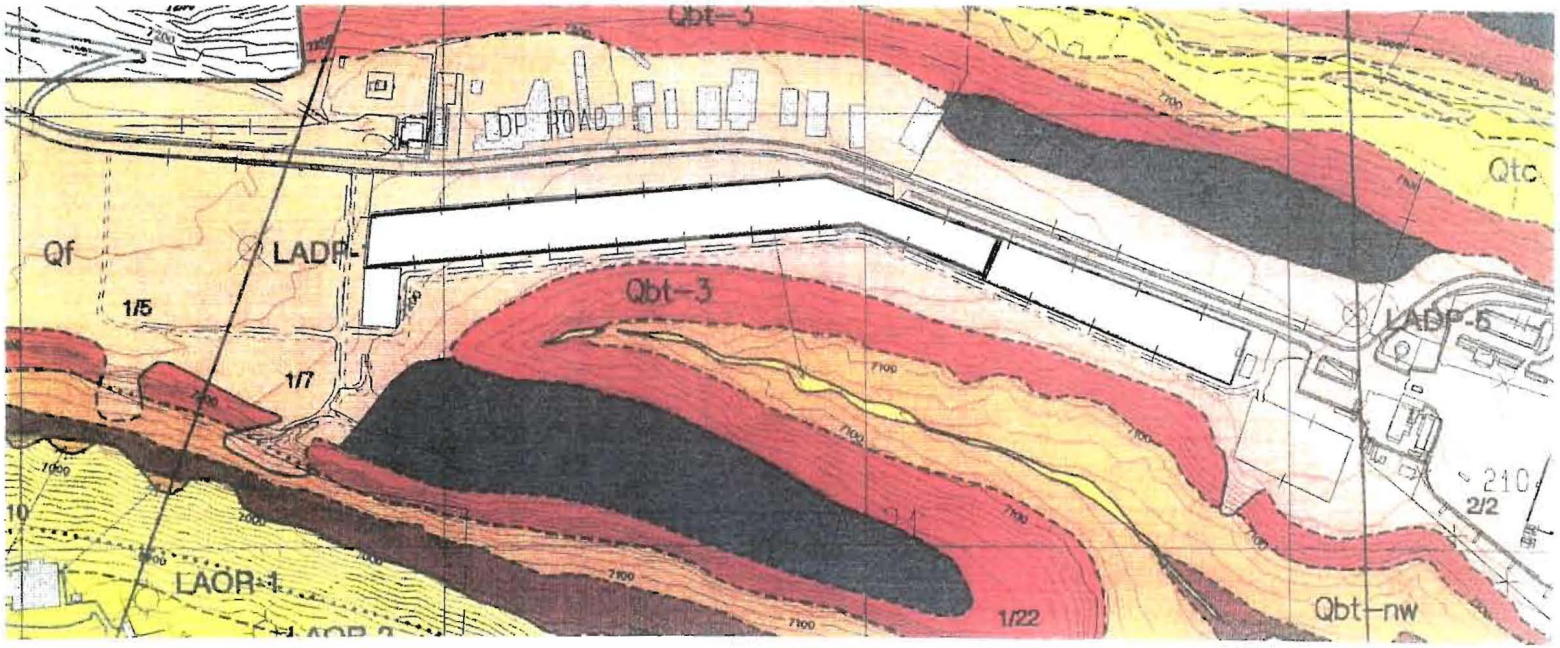

Qf Artificial fill and disturbed soils on mesa tops.

Qmt Mesa top soils developed in weathered Bandelier Tuff, loess, and alluvium on mesa tops; includes small bed rock outcrops.

Qtc Talus and Colluvium; slope wash and rock fall from local sources; includes small landslides, small alluvial fans, and small patches of alluvium on canyon sides.

Qal Alluvium; stream deposits of gravel, sand, silt, and clay in valley bottoms.

Qbt-3 Unit 3; cliff-forming, nonwelded to partially welded ignimbrite; combined with nonwelded Unit in east side of map area.

Qbt-nw Slope-forming, nonwelded unit; jagged contact lines show approximate eastern limit of unit, combined with Unit 3 in east side of map area.

Qbt-2 Unit 2; cliff-forming, partially to moderately welded ignimbrite.

Qbt-1 Unit 1; nonwelded to partially welded ignimbrite; vapor-phase notch occurs in this unit and vapor-phase alteration is widespread above this feature; Tsankawi pumice fall at base of Unit 1.

MDA-B

N

SCALE

400 0 400 800

FEET

Figure 2.8: Geologic map of MDA-B vicinity. (After Broxton et al., 1995)

Chapter 3

Previous Geophysical Surveys

Material disposal and paleostream channel sites at TA-21 were preliminarily investigated in the summers of 1996 and 1997 by the SAGE geophysical field course (Ferguson et al., 1998). The investigation, consisting of a combination of seismic refraction, magnetic, electrical and radar surveys, was done at two sites. Five refraction lines were shot near MDA-A and MDA-T. Ground Penetrating Radar (GPR) and resistivity surveys were also performed on three of these lines. A buried paleochannel was discovered near MDA-T. A total of seven refraction lines were shot at MDA-B, five transverse to the supposed trench and two longitudinally (Fig. 3.1). Also a total field magnetic map (Fig. 3.1) was made on the unpaved eastern end of MDA-B. A seismic model and the nearest four magnetic profiles for the line 5 can be seen in Fig. 3.2.

An additional seismic line and some magnetic lines were accomplished in the paved part of the site. Also, resistivity and GPR profiles were made at the west-end of the unpaved area. These surveys established that waste trenches and stream channels could be mapped using seismic refraction methods. In July 1998, Bay Geophysical

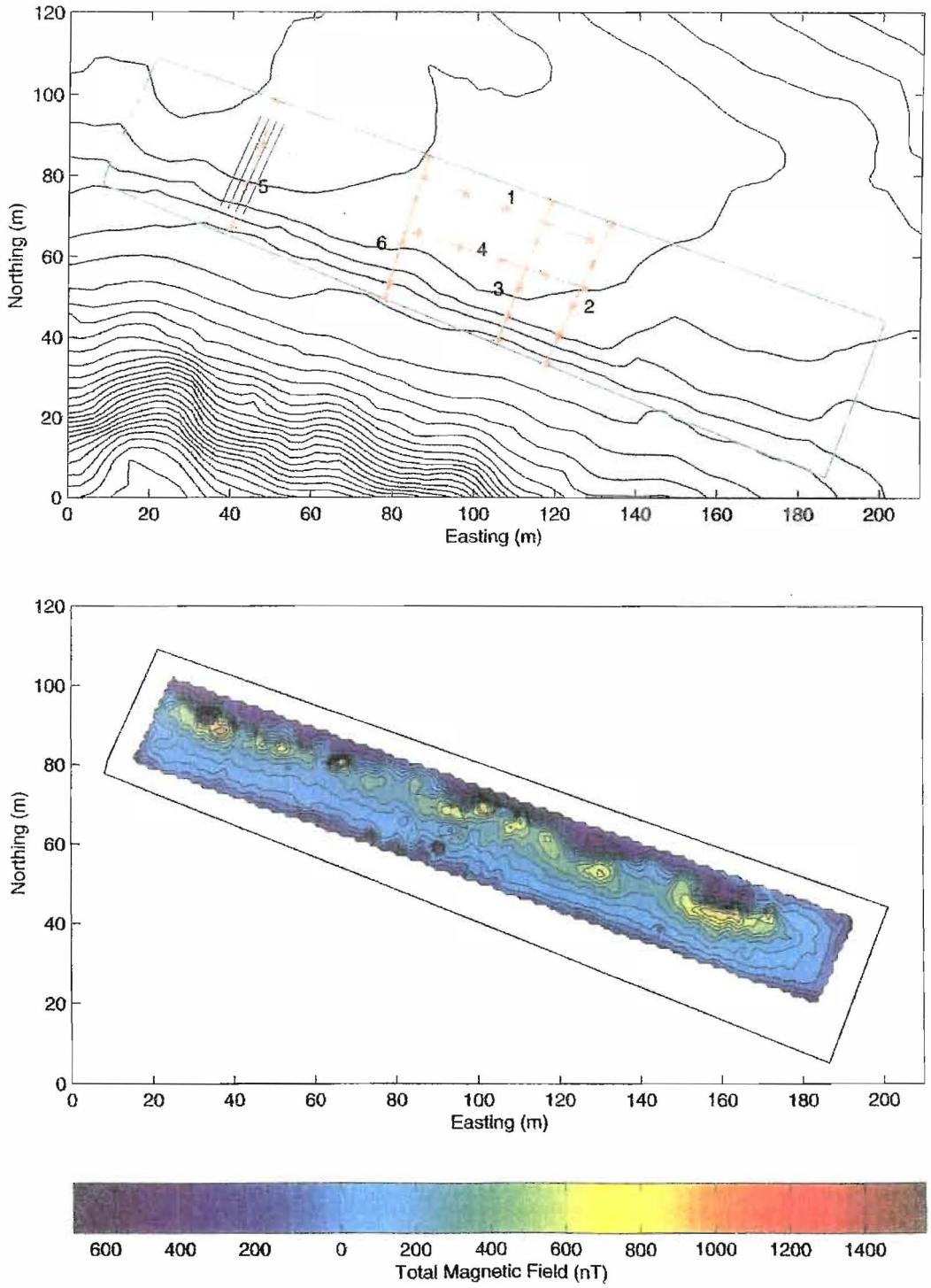

Figure 3.1: Seismic lines 1-6 at MDA-B, and the acquired magnetic map, SAGE 1997 (Ferguson et al., 1998).

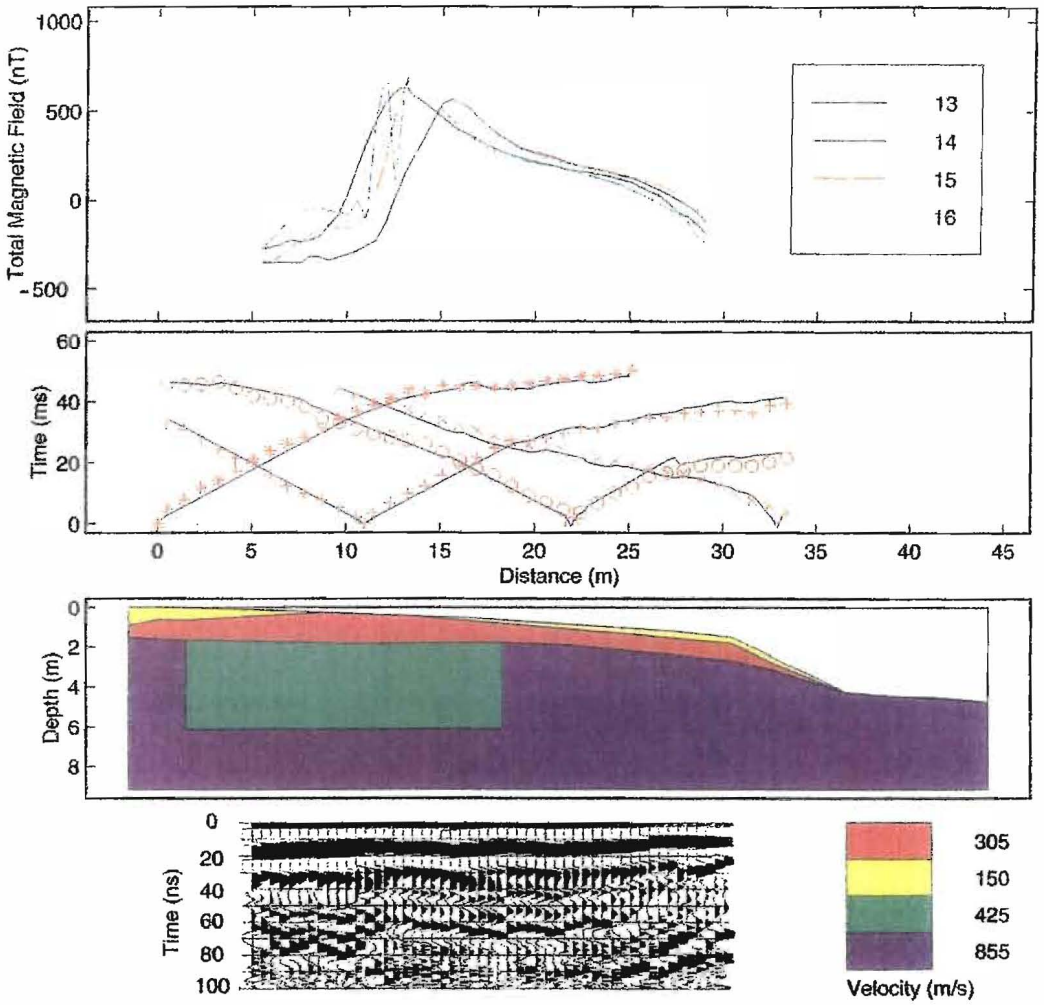

Figure 3.2: Seismic model for line 5 (middle), radar (bottom), and magnetic profiles (top) at MDA-B. Synthetic travel times are the solid blue lines, red symbols are observed traveltimes. SAGE 1997 (Ferguson et al., 1998).

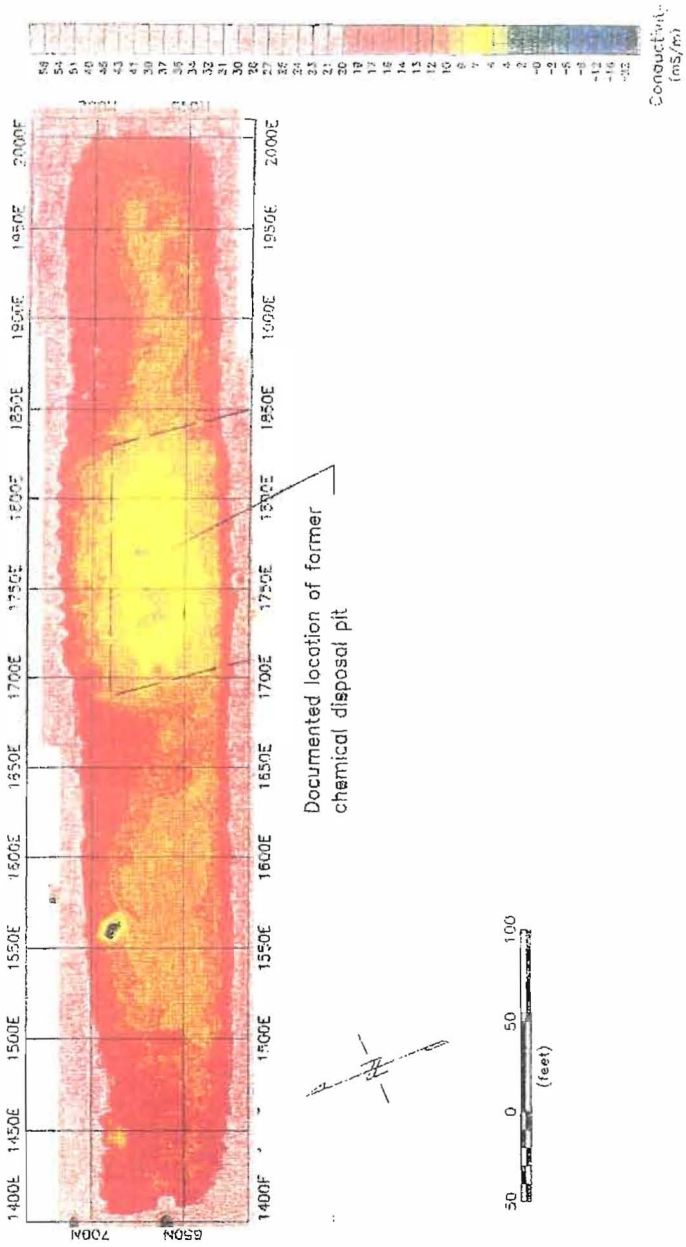

Figure 3.3: Terrain conductivity Map at eastern unpaved area, MDA-B (See also Fig. 9.8). Note that coordinates used by BGA are not related to the NM state plane grid used in this thesis. (After BGA 1998).

Associates, Inc.(BGA) was appointed by LANL to carry out a geophysical investigation. The survey was based on GPR and electromagnetic (EM) techniques and covered the whole of MDA-B (McQuown, 1998) . In particular, an EM-31 for the terrain conductivity study and an EM-61 for the detection of metal objects were used. Conductivity data were acquired at 2.5 ft intervals along parallel grid lines spaced 5-ft apart. GPR data were collected along traverses established over EM anomaly indications. The GPR profiles were located with the intent to provide depth estimations. The goal was to delineate the lateral and vertical boundaries of the pit, integrating the GPR and EM surveys. Some results of EM-31 survey made by BGA over the area B are shown in Fig. 3.3.

Even though the initial objective was not really achieved, the survey revealed a general picture of the conductive objects. Maps of anomalous conductivity generally conform to potential trench locations. Exact definition of these trenches are not really possible from these data. Unambiguous interpretation of the GPR data (both SAGE and BGA) is difficult, and exact depths cannot be estimated mainly due to lack of velocity data and the presence of clayey-behaved material.

The magnetic map that had been acquired by the SAGE/UTD survey previously at that summer had yielded a picture similar to the conductivity maps (Fig. 3.1).

Chapter 4

The Seismic Refraction Method

The seismic refraction method had its beginning in World War I with the development of seismic instruments for location of artillery. After the war this technology was rapidly developed for petroleum exploration; its success was due to its simplicity. Seismic refraction has been successfully used for geophysical investigations over waste disposal sites and landfills e.g (Green et al., 1998; Lanz et al., 1997; Steeples et al., 1997; Green et al., 1999). The method commonly refers to the interpretation of first arriving P-wave traveltimes. Traveltimes are measured over a "spread" of geophones, arrayed at increasing offset distance from a common "shot" point (seismic energy source). The seismic refraction methods are most readily applied to situations in which there are essentially flat-lying strata (Scott, 1973; Lankston, 1990; Belfer et al., 1996), each having differing propagation velocities for the compressional waves. A requirement is that the velocity of the waves increases with depth (Telford et al., 1996). Ray paths are either turned back to the surface by increasing velocity gradients or critically refracted at distinct layer boundaries. Solutions for layered models are well known (Dobrin and Savit, 1988). In the refraction method ray paths are

generally horizontal as opposed to the reflection method where they are more vertical. Refraction methods permit accurate measurements of seismic velocity whereas the reflection method is more sensitive to lateral structural variations. Multiple shot points recorded into the same spread permit the interpretation of lateral as well as the vertical velocity variation. In more complex structures ray tracing methods have been applied for interpretation. Recently, new methods based on wavefront extrapolation have been developed (Schneider et al., 1992) which are more easily applied to models with strong lateral velocity variation (Fig 4.1(b)) (Smith and Ferguson, 2000). Schneider's algorithm deals successfully with large contrast, discontinuous velocity distributions as opposed to the ray tracing techniques which suffer complications due to critical refractions. The algorithm follows a dynamic programming approach to compute traveltimes across a uniform grid. (Fig 4.1(a)) . The achieved accuracy of the method is reasonably high (0.12% error).

4.1 Refraction Traveltime Curves and Raypaths

On the time-distance graph of first arrivals (Fig. 4.2) each deviation from a straight line indicates a lack of uniformity, either in geometry or in seismic velocities. The shallowest horizon is defined by the direct wave. At a sufficient distance from the energy source the critically refracted wave in the following layer will arrive first because of it is traveling mostly in the lower higher velocity layer. When the variations of traveltime with distance have been determined, depths and velocities of the refracted horizons may be deduced from the traveltime curves. Snell's law and the principles of Fermat and Huygens determine the raypaths and consequently

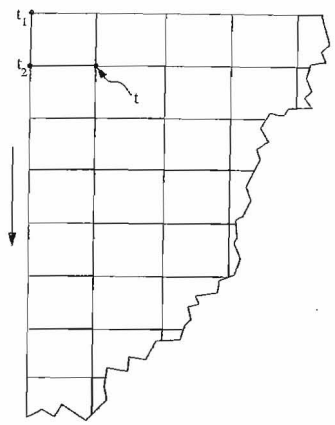

(a) Grid layout

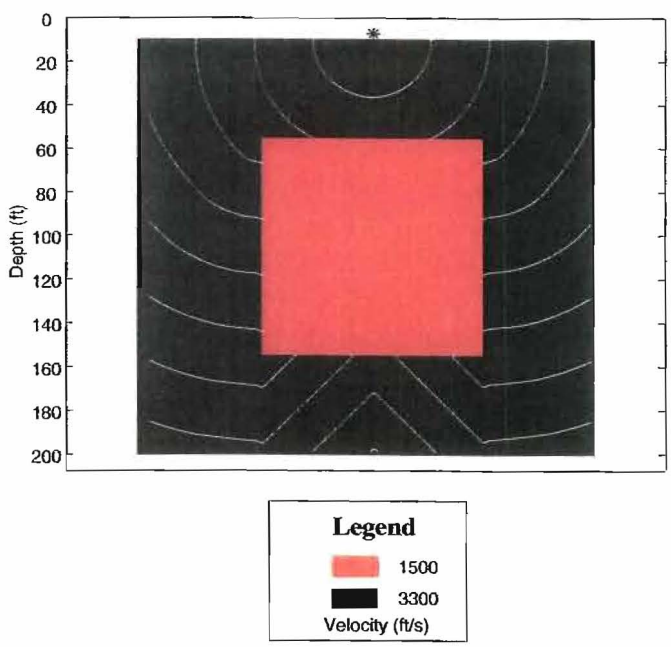

(b) Synthetic model

Figure 4.1: Wavefront extrapolation using the Schneider algorithm. The distortion of the wavefronts, here shown at regular time intervals (white solid lines), is due to the presence of a low velocity medium (red). (After Schneider et al., 1992)

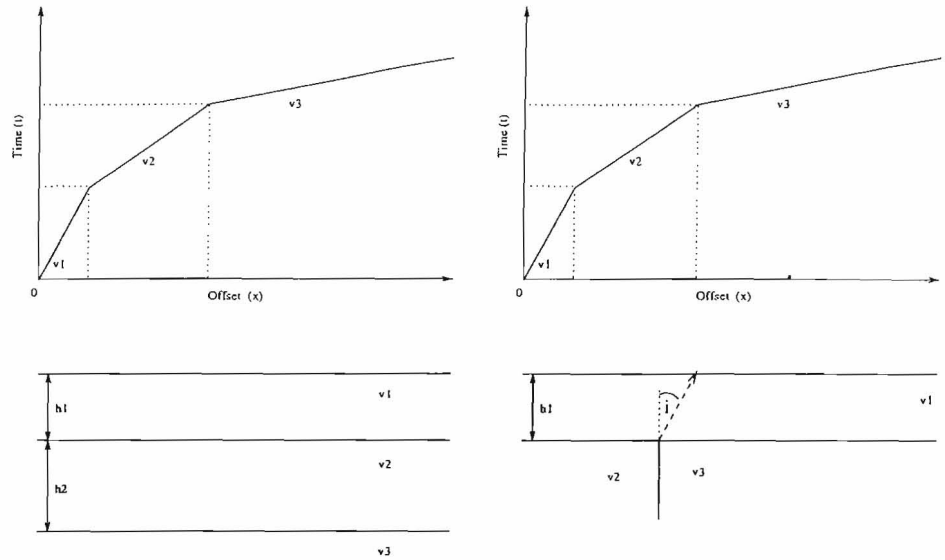

(a) Ambiguity arises

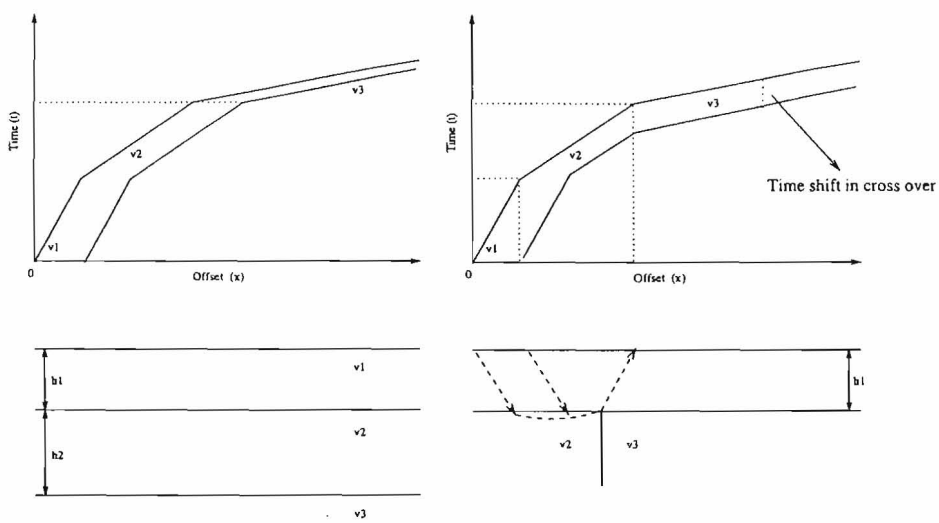

(b) Ambiguity Resolved

Figure 4.2: In the case of a single shot point (part a), one cannot distinguish between horizontal and vertical structure. In part b this ambiguity is resolved. (After Lankston 1990)

the arrival time instances. Interpretation methods that determine the geometry and velocity of each horizon do not always guarantee the uniqueness of the solution (Lankston, 1990; Lankston and Lankston, 1986), which is therefore ambiguous -Fig. 4.2(a). This ambiguity however can be drastically restricted by shooting in opposite directions over the same path, or even better, by use of multiple shot points for each geophone spread (Ackermann et al., 1986; Lankston, 1990; Lankston and Lankston, 1986) Fig. 4.2(b). The number and spacing of the extra shotpoints usually depends on the complexity of the geology and the attenuation of the medium.

Chapter 5

Seismic Survey of MDA-B Site

5.1 Methodology

Among all the geophysical methods the most suitable for trench mapping seems to be the seismic refraction approach. The nature and origin of the disposal sites posed severe constrains on potential approaches. High electric currents, boreholes and explosives had to be avoided due to potential disturbance of the site. A steel, chainlink fence surrounding the area restricted the configuration of magnetic surveys, since the fence produces a magnetic anomaly which obscures those due to subsurface sources. Seismic reflection methods do not work well at shallow depths (Steeples et al., 1997). Although the attenuation of seismic energy in the Bandelier tuff and trench fill is very strong, refracted P-waves can be reliably recorded over a range of up to 40 or 50 m. The use of multiple shot points on each recording spread permits resolution of relatively small scale structures, such as individual pits.

5.2 Survey Configuration: Selection of Seismic Lines and Data Acquisition

Preliminary analysis of the magnetic map (Plate I) allowed a rough estimate of the lateral boundaries of the trenches. Hence, the magnetic survey served as a guide for the final configuration of the position of seismic lines. In order to sample the whole of MDA-B a total of 29 lines were shot (Fig 5.1).

As a distance unit through out this work feet ft was selected, since it complies with existing maps and configuration of seismic cables. However, in the magnetic modeling and occasionally in few other places, meters m was used instead to be consistent with the SI unit system and to avoid "mixing" units during the complex computations of the synthetic magnetic field. This is a convenience rather than an inconsistency.

MDA-B can be divided into 3 parts (Fig. 5.1). The eastern part is the unpaved area previously used for moisture studies in the 1980's (Nyhan and Barnes, 1989). In the unpaved eastern area Lines 1-6 were shot by the SAGE field course in 1997 (Fig. 3.1) (Ferguson et al., 1998). The second and biggest part involved the entire asphalt-paved area. A total of 18 lines; 12 of them (Lines 8-13 and 29) were located at the eastern end. Most of the lines were transverse to the axis of the site, with a spacing varying from 10 m to about 100 m. In order to estimate the seismic velocities of the undisturbed geology Lines 1, 18 and 19 were intentionally shot close to the edges of the site, where the probability of crossing the trench was small. The longitudinal lines were acquired to tie the transverse ones. Another expanding pattern of transverse lines, more widely spaced, (Lines 25, 26, 7 and 28) were used to trace the rest of

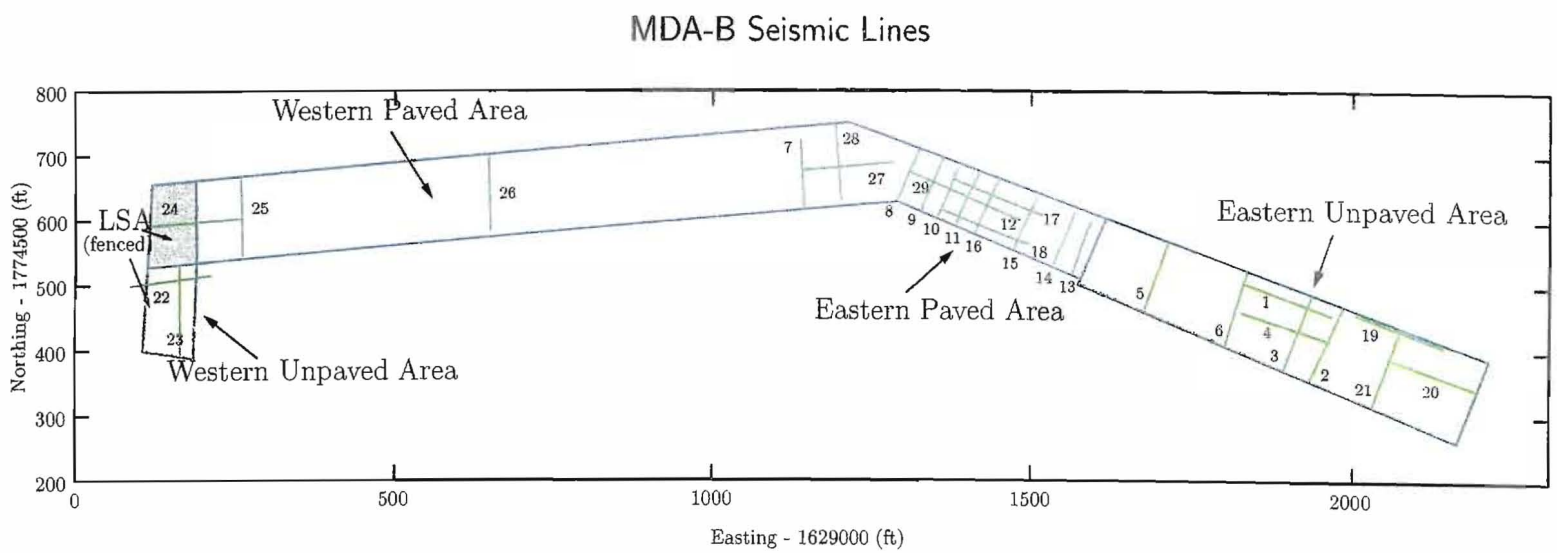

Figure 5.1: Configuration of seismic lines 1-29 (green lines) in MDA-B. (Blue lines follow fence).

the western paved part of MDA-B area. The paved part may also subdivided into a western and eastern portion. Finally on the third part, consisting of the L-shaped unpaved area at the western end of the site, were shot 2 lines (22, 23) perpendicular to each other.

The geophone spacing was 3 ft in every seismic line, while the energy source was free to move in between; usually every 6 geophones on the short lines and every 12 on the longitudinal ones. The position of geophones and shot points were determined from a 1:1000 topographic map (Broxton and Eller, 1995). We used a 48-channel Bison 9048 recording system, with frequency response 4-1000 Hz. During recording two analog filters were applied; a low cut at 4 Hz (2-pole steps Butterworth), and a high-cut (6-pole Butterworth) at 1000 Hz since the sampling rate was 200 ms. The geophones that were used had damping factor 0.74 and natural frequency 30 Hz.

Finally as an energy source we used an "airless jackhammer". This hammer consists of a vertically constrained steel rod which strikes the ground with the force of a large sledge hammer. We know that the frequency content of the produced elastic wave is not the same when the shot is fired in hard rock as when it is shot in loose material. Shooting in loose or plastic material is characterized by less peaked spectrum due to the relative higher damping factor. The shape and frequency content of the source affects directly the shape and spectrum of the seismogram.

The asphalt served to change the shape of the source wave and also acted as a high velocity layer on top of the lower velocity filling material, thus violating one of the most basic assumptions of the refraction method. These high velocity arrivals in the asphalt layer would make the near source traces unusable in many of the records shot in the paved area. Lines 7-15 were shot with the source on the asphalt surface and

the geophones in small, chopped holes, while Lines 24-29 were shot with the source in a one square-foot chopped hole with much better results (Fig. 5.2).

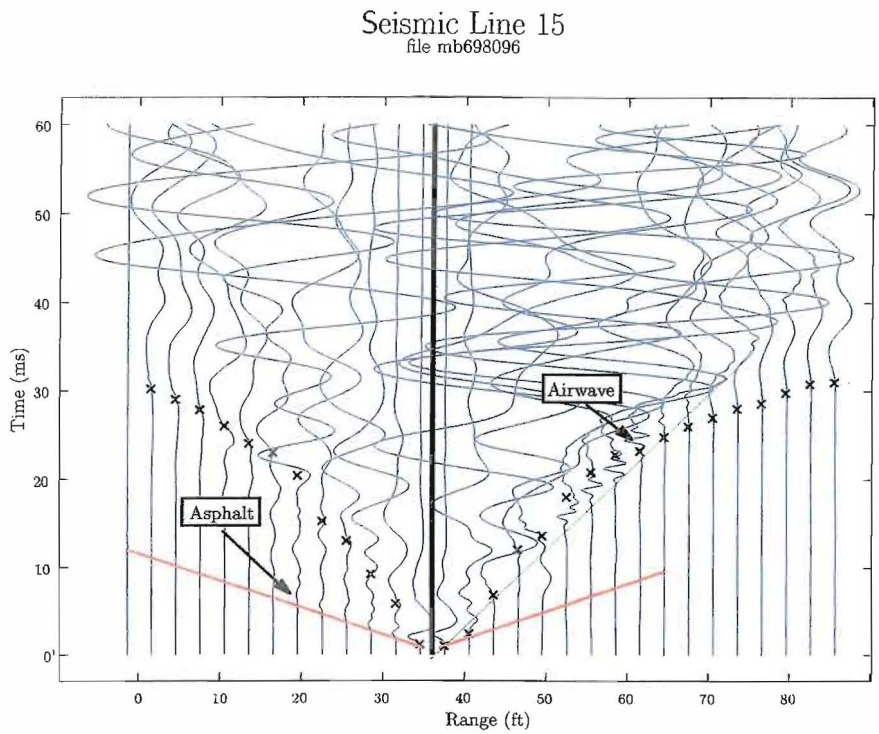

(a) Line 15

Figure 5.2: Seismic traces for a representative source on asphalt line (see also Sec. 5.3). x markers are P-wave picks.

5.3 Seismic Noise and Picking of the first arrivals

In general a seismogram contains seismic noise with various kinds of origin. External sources of noise are most crucial and can affect dramatically the recorded signal.

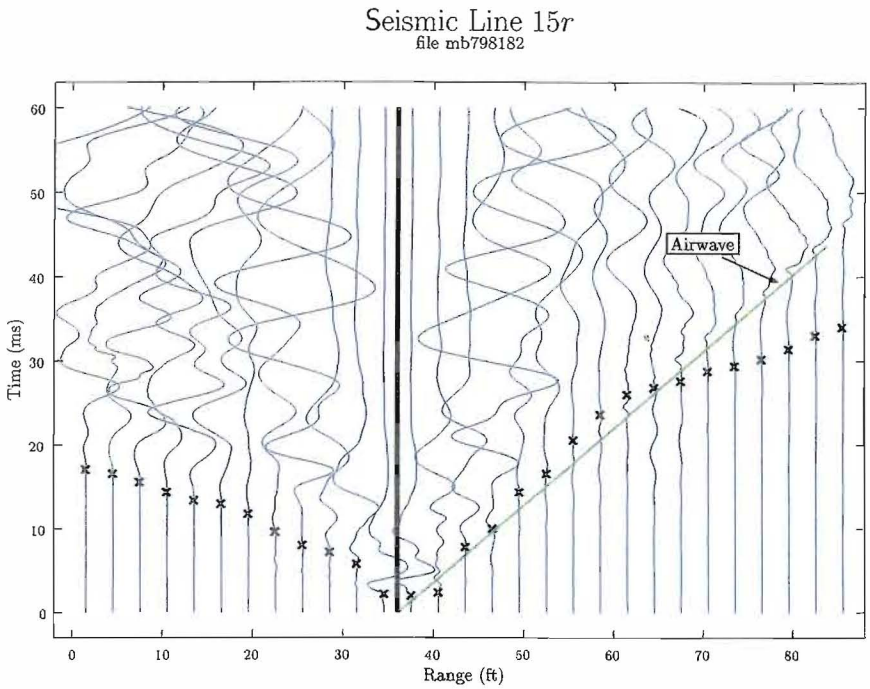

(b) Line 15r

Figure 5.2: (Con't) Asphalt effect and airwave coupling. Hammer in $1ft^2$ chopped hole in asphalt.

Common sources of this kind of ambient noise are cultural activity, wind, and induced electromagnetic noise due to power lines or even atmospheric electric activities (Green, 1974). Even though in most of the cases we were able to protect against these unwanted signals eliminating or diminishing them, it was impossible to achieve a noise-free seismogram. Furthermore, the airwave obscured the first arrival of the $P-$waves in most shots due to the very low surface $P-$wave velocity. In seismic refraction method usually the only part of the seismogram that is important is that which contains the first break of the first arriving wave $P-$wave, the "pick", and the rest of the signal is ignored.

The question that arises here is how can we know that the first visible arrival is the $P-$wave and not something else. This is known as the *event recognition* problem, and airwave coupling at the first part of the seismogram can lead to such a false identification. Furthermore, even in case of right event recognition there is still an uncertainty that has to do with the right *event timing*. Due to presence of noise, the first break can be "shifted" in the time domain. This "shifting" has to do with the fact that the recorded signal is the sum of the signal produced by the hammer and any other external source (noise). The nature of the two components is usually different; Seismic arrivals are deterministic, while the noise in most cases appears to be random. Assuming that the last statement holds, significant signal enhancement can be achieved by stacking (summing repeated measurements), a common practice in seismic acquisition. It can be shown that under some simple assumptions, usually fulfilled, the picked traveltime t_p is an unbiased estimator of the real, noise-free, first break t_0 (Mateeva, 2000). Problems arise when the output response of the system (recorded signal) is asymmetric and cannot approximated locally by a monochromatic

harmonic function, *sin* or *cos*. The timing error in general is proportional to signal to noise ratio S/N, and simultaneously depends on the frequency ratio between the signal and the noise. The "deltaness" of the input affects also the positioning of the first break; the "sharper" the signal the more robust its positioning is.

Materials at MDA-B have very high attenuation (low Q). This causes the signal to diminish rapidly and to decrease in frequency, lowering the signal to noise ratio S/N. In any case lost or altering of signal is compromised with noise presence. As a result some noise is always recorded to insure that the first break has been recorded as well.

5.3.1 The Picking process

Picking the first break in the acquired data was difficult. Initially, the picking was done using the `BSIPIK v3.2` software package (Rimrock Geophysics, Inc.) based on a correlation technique. Afterward, the automatic pickings were adjusted and refined manually based on the nature of the first break since the automatic picks were almost always incorrect. In most of the seismograms the velocity of the first layer was much lower than the airwave. Consequently pickings were chosen in order to correspond to that layer avoiding the airwave breaks. In order to minimize any kind of subjectivity we did this in cases were the first break of the P-waves (second arrival) could be clearly distinguished from the airwave (first arrival). Situations like that correspond to very low values of the elastic moduli in high porosity materials, like soil or landfill.

Another pitfall concerning the first break picking had to do with the asphalt itself. At the paved area the asphalt acted as a high velocity layer creating a local velocity inversion (high velocity layer is on top of a lower velocity layer, Fig. 5.3). Ordinarily,

this local velocity inversion cannot be determined by the refraction data. However, it has been demonstrated (Tewari et al., 1995) that if the high velocity layer is thin relative to the underlying lower velocity layer it produces a traveltime skip with a magnitude directly related to the thickness of this low-velocity layer. This time offset is due to the delay of the P-waves as they travel through the low-velocity medium (Banerjee and Gupta, 1975; Greenhalgh, 1977; Whiteley and Greenhalgh, 1979). Also there is a strong attenuation of the P-waves (first branch of the curve) because of the energy leakage that takes place at the interface (Press and Dobrin, 1956; Green, 1962). The asphalt problem was reduced or diminished for areas of thin and highly broken pavement. In general the greatest difficulties in the picking process were related to the presence of asphalt. The picked traveltimes were used to reconstruct the velocity distribution on the seismic lines.

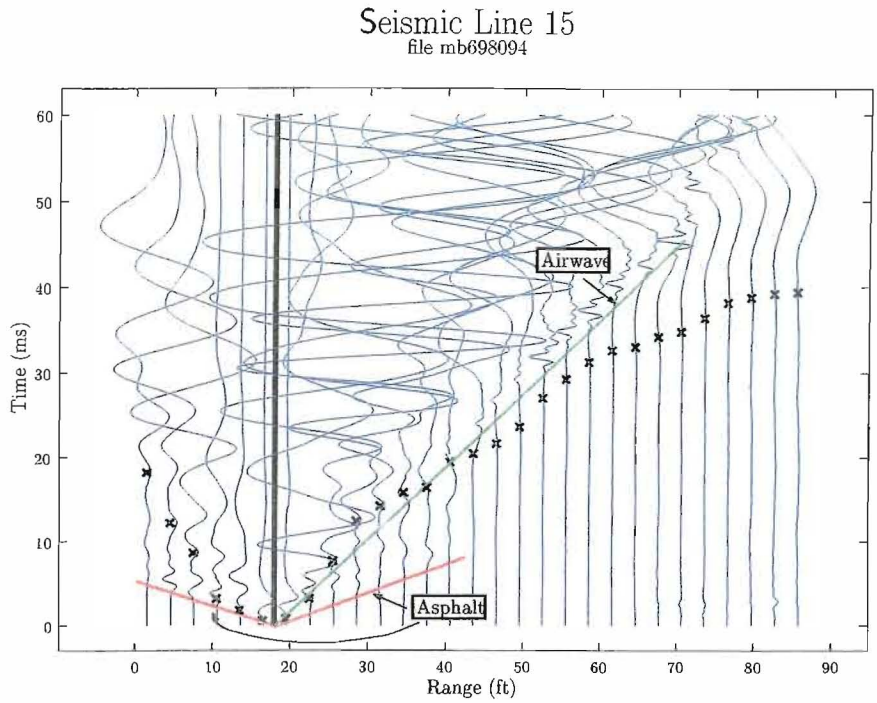

(a) The asphalt underneath the hammer is present.

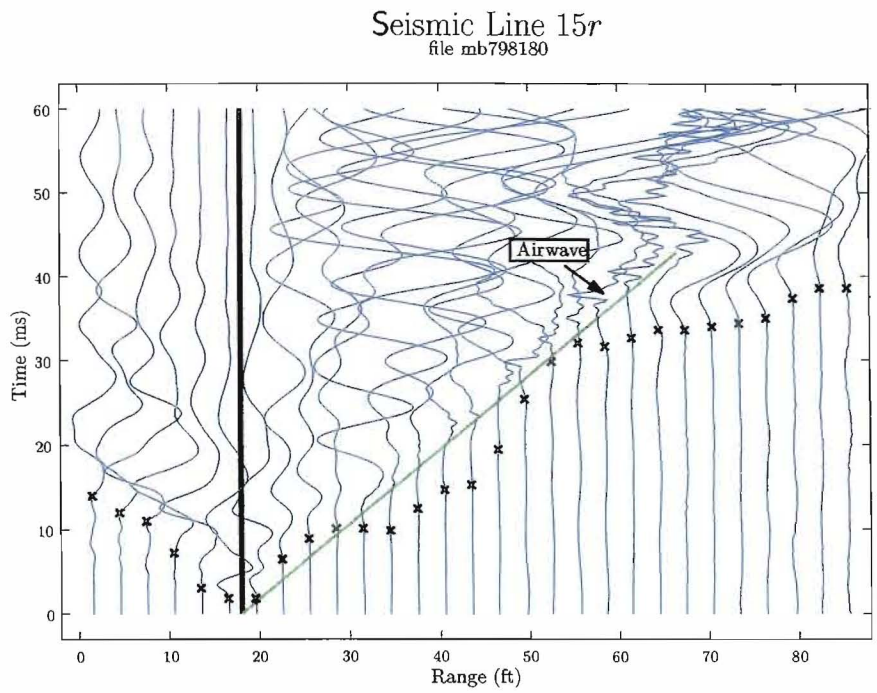

(b) The asphalt has been removed.

Figure 5.3: Local velocity inversion because of the asphalt presence.

Chapter 6

The Magnetic Method

Magnetic surveying is generally cheaper than other geophysical methods, therefore, magnetic observations are commonly used for reconnaissance. The magnetic effects from buried bodies of a given shape and magnetization can be calculated from potential theory (Blakely, 1995). The method is particularly attractive where the objective is to isolate materials with high magnetic susceptibility contrast (e.g., buried ferrous objects). In magnetic prospecting, the susceptibility is the fundamental material property whose spatial distribution we are attempting to determine. In the absence of macroscopic currents the magnetic field intensity **H** is irrotational, (Kellogg, 1953; Kaufman, 1992) and consequently its scalar potential U is a harmonic function and can uniquely determine the magnetic field **B** (unfortunately the inverse is not true).

The magnetic induction or magnetic field **B** is given then by the equation (Blakely, 1995)

$$\mathbf{B}(P) = -\nabla_P(U(P)) = -\frac{\mu_0}{4\pi}\nabla_P \int_R \mathbf{M}(Q) \cdot \nabla_Q(\frac{1}{r})dv \quad (6.1)$$

where $\mathbf{M}(Q)$ (in $\frac{A}{m}$) is the magnetization at point **Q**, r is the distance from the

observation point $\mathbf{P}$ to $\mathbf{Q}$, (boldface symbols refer to vectors) (Fig. 6.1). The proportionality constant has units in SI, $\frac{\mu_0}{4\pi} = 10^{-7} H/m$ and μ_0 is the permeability of free space. In the above equations the term $\mathbf{M}$ can refer to the total magnetization which includes the induced magnetization $\mathbf{M_i}$ due to the external field $\mathbf{H}$ as well as the remanent magnetization $\mathbf{M_r}$. In this case $\mathbf{M} = \mathbf{M_i} + \mathbf{M_r}$ and the magnetization vector has an arbitrary direction (Bhattacharyya, 1964), while in this case the total magnetic field $\mathbf{B}$ is given by the equation

$$\mathbf{B} = \mu_0(1+\chi)\mathbf{H} + \mu_0\mathbf{M_r} \tag{6.2}$$

Here χ is the magnetic susceptibility of the material. In some cases the term of $\mathbf{M_r}$ can be ignored (as negligible) but in general we measure the total magnetic field $|\mathbf{B}|$ and the magnetic anomaly T is given then by

$$\Delta T = -C_m \hat{\mathbf{F}} \cdot \nabla_P \int_R \mathrm{M}(Q) \cdot \nabla_Q(\frac{1}{r}) dv \ , \quad \left\|\hat{\mathbf{F}}\right\| = 1 \tag{6.3}$$

where $\hat{\mathbf{F}}$ has the direction of the regional field (Blakely, 1995).

6.1 The general magnetic interpretation problem

In order to estimate depths and dimensions of the magnetic anomalies forward modeling was performed. Comparison of the observed magnetic data with the results calculated from simple geometrical models can give estimates of depth, size, shape, and possibly susceptibilities of the magnetic sources. In general we cannot calculate absolutely the magnetization distribution in three-dimensional space from plane observations. The magnetization anomalies may be attributed to a variety of models (the non-uniqueness problem). In addition noise that is usually recorded with the signal limits the accuracy of the constructed model; small amounts of added noise can

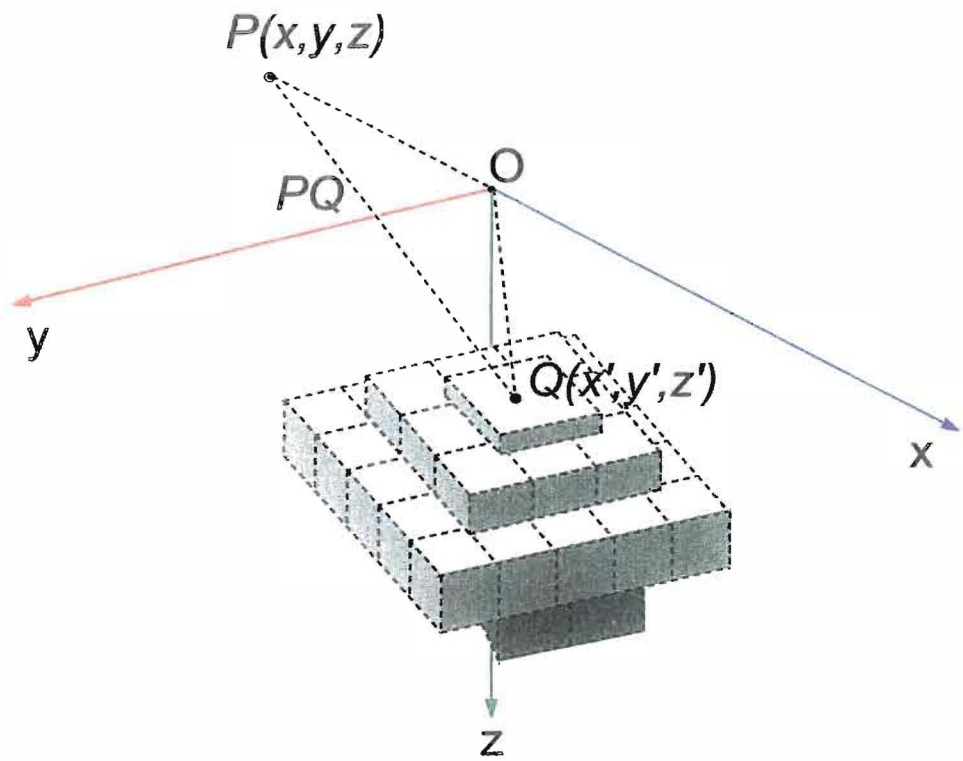

Figure 6.1: Calculation of the magnetic anomaly of an arbitrary shaped body.

cause a large change in the model (Naidu and Mathew, 1998). At the survey site the observed magnetic anomaly is composed of a number of small scale sources buried at shallow depth with varying shapes and magnetizations. There are some isolated and well defined anomalies surrounded by scattered and apparently random distributed magnetic material. Nevertheless, as long as these anomalies are associated with the trenches they can provide extra constraints on the geometry of the trenches. The total magnetic anomaly can be considered as a superposition of the buried, scattered magnetic sources, and the anomaly that is produced by the trench itself.

6.1.1 Depth estimation of the magnetic bodies

One of the most important parameters of the model estimation is the depth to the source of the anomaly. This estimation becomes more ambiguous as we deal with more than one nearby source. Solutions to this problem are well known, either for randomly magnetized well defined shape sources or for constant magnetization bodies but with arbitrary boundaries (Blakely, 1995; Naidu and Mathew, 1998). As it usually happens, real situations fall in between. In this case the choice of the optimal approach is based upon pre-existing information.

Approximate estimations of depth to the top of an isolated anomaly can be done using simple graphical rules like the Peters half slope method (Peters, 1949), or the Parasnis method for asymmetric anomalies (Parasnis, 1986). For complex anomalies the above estimates deviate drastically and any attempt at depth estimation is unsafe.

Another approach to determine mean depths of ensembles of prismatic bodies is to use the amplitude and energy spectra (Spector and Grant, 1975; Gerard and Debeglia, 1975; Bhattacharyya and Leu, 1977). Depth estimation, can be based on the slope of the line segments on a radial power spectrum profile, an average version

of the spectrum over a set of concentric rings with increasing radius (Naidu and Mathew, 1998). In most cases the wavelength in conjunction with the gradients of the anomaly can determine the depth. Shallow sources produce high horizontal gradients near the edges. Blakely and Simpson (1986) suggested a computational method to define the edges of magnetic (or gravity) anomalies using the horizontal gradients.

In MDA-B most of the anomaly sources are at shallow depth, and the horizontal gradients define well the lateral boundaries of the bodies. Starting from simple graphical depth estimations and building models that fit the data and take into account the above principles is another approach for depth calculations. In this case the most suitable building block is the prism as opposed to spheres or cylinders since i) complex bodies can be approximated by a collection of prisms and ii) the horizontal gradients of spheres or cylinders give, because of their higher symmetry, no precise information about the lateral extent (Green's equivalent layer principle).

6.1.2 Anomaly of the trenches

The most important target for this survey is the geometry of the trenches themselves. Since the trenches were excavated within the tuff, a uniformly magnetized and practically infinite slab that yields no anomaly, they may produce by themselves considerable anomalies. On the other hand, we know that the magnetic objects were dumped into the ground along with other rubbish (paper, class, wood, etc) which mask and interfere with the anomaly of the trenches. In spite of this, the wavelength of the trench anomaly is longer than those from the individual sources. In this case frequency domain signal processing can be applied for signal enhancement. The filtering techniques, e.g. band pass filtering, may be applied successfully in situations

where there is a clear concentration of energy in distinct wavenumbers (Zurflueh, 1967).

Even in this rather optimistic scenario, power leakage from other sources (usually with similar wavenumbers) contaminates the signal resulting in an anomaly distortion. Upward continuation and low pass filtering suppresses the high frequency anomalies in favor of the lower ones. Pole reduction shifts the negative (or positive) lobes of the anomalies making the interpretation easier. Pole reduction also serves as a criterion for the determination of the polarization direction of the field (distortion analysis), (Naidu and Mathew, 1998). In the absence of remanent magnetization the polarization vector points to the direction of the ambient field, and pole reduction transforms the anomaly from dipolar to monopolar mode making the anomaly more symmetrical and the interpretation simpler. In the presence of remanent magnetization this effect is maximized when the assumed polarization direction approaches the real one.

Finally the downward continuation and the second derivative was considered unstable for this survey. However the second derivative depicted the shallowness of many sources. The above operations were applied selectively to parts of the magnetic map.

6.2 The Magnetic Survey at MDA-B

The magnetic survey at the eastern unpaved area of MDA-B was done during SAGE 1997 (Ferguson et al., 1998), and for the rest of the site in 1998. The map (Plate I) was initially used as a guide for the design of the seismic survey. Also it revealed a linear pattern of magnetic anomalies along the site in the order of up to 10,000 nT, that mainly reflect the existence of ferromagnetic material buried at shallow

depth. It consists of 454 magnetic profiles of North-South direction each one having sample interval of about 1m, and was acquired using a Geometrics cesium vapor magnetometer. The raw profiles were sampled rapidly in time and were acquired by walking with the magnetometer at a constant pace. Then the data were despiked, smoothed and resampled at $1m$ intervals. The profiles were measured relative to the fence lines. Mapped fence corners were used to locate the profiles in New Mexico state plane coordinates.

The magnetic anomalies can be divided into three main groups: a) high negative anomalies at the edge of the map whose amplitudes are of the order of -3000 nT that have a linear expansion and correspond to the fencing of the site. The anomaly appears to show only the one negative lobe; b) high positive anomalies up to 7000 nT with their corresponding negative parts due to the dipolar nature. They are located in the middle of the site each one having in general the orientation of their polarization vectors parallel to the ambient field. c) scattered noise that has been recorded during the survey and affects the whole map. A regional field of 51500 nT has been subtracted from the map. Because of the large size and the complex shape of MDA-B, and the fact that the survey was conducted at different time periods, the site was divided into four areas. The processing of the magnetic signal for each area was different depending on the characteristics of the local anomalies.

6.2.1 Eastern Paved Area

The eastern end of the paved part or EPA (Fig 6.2) appears to be the most magnetically "complex" part of the site. This is due, to a certain degree, to its closeness with the fence (it is the narrowest part of the site) and the superposition with other shallow magnetic sources (mainly at the north side). Because of the anomaly's

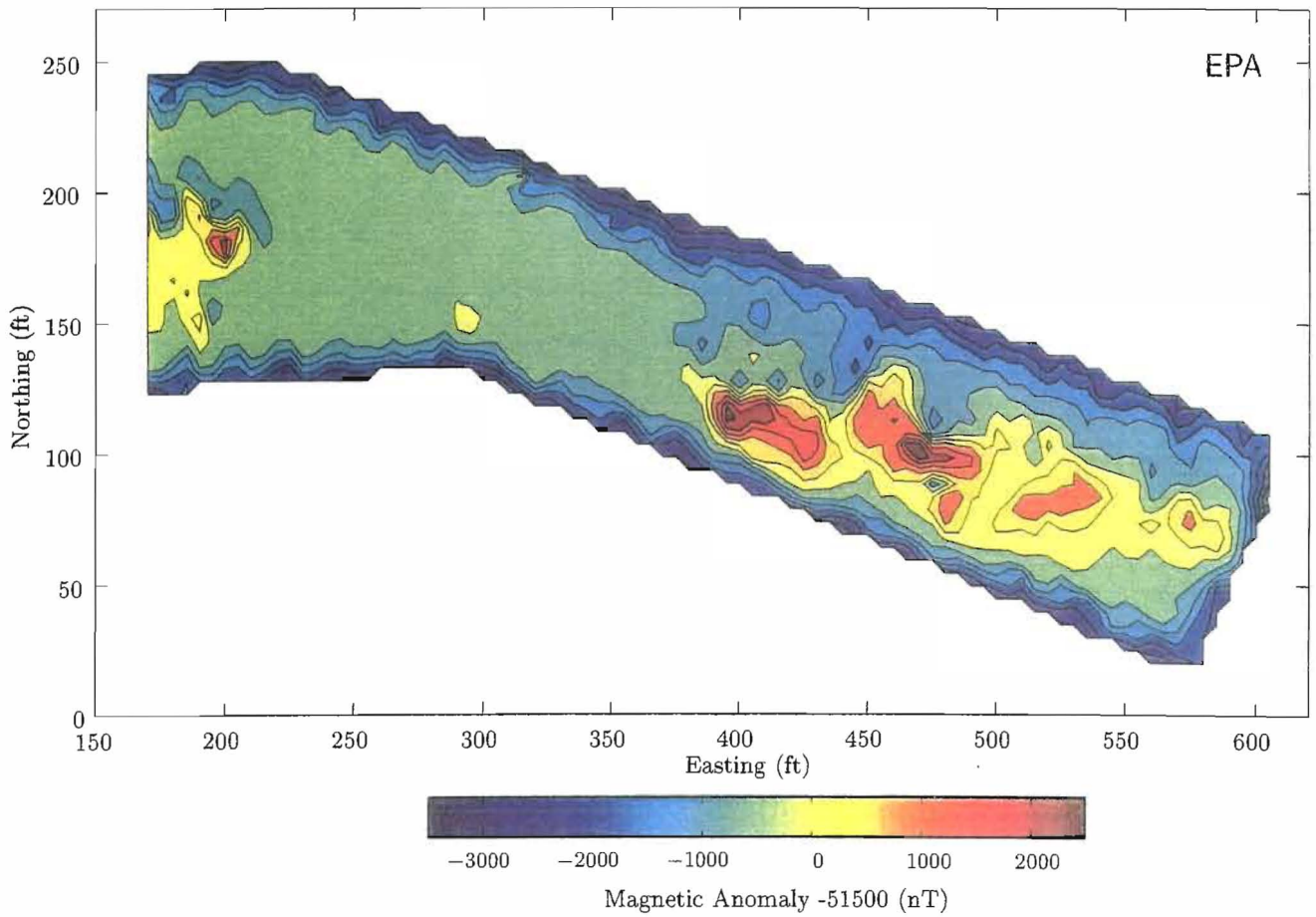

Figure 6.2: Magnetic anomaly at Eastern Paved Area.

complexity and its strong interference with the nearby fence any attempt for further interpretation may be biased and unsafe. Furthermore, since the objective is to enhance the contrast between the signal due to the anomaly target and the rest of the signal, digital processing of the magnetic data is an obvious next step. With the term anomaly target we mean the pit itself as well as any magnetic sources within it. The magnetic map is a discrete version of the potential field measured at a certain surface; in this case a horizontal plane. The Nyquist frequency that depends on the space sampling interval of the survey determines the shortest wavelength that can be resolved from the data. Anomalies with different wavelengths yield spectra with different wavenumber (frequency) content. Also the fact the sampling interval was different at the N-S profiles ($\approx 0.3m$) than at the E-W direction (line spacing interval $\approx 1m$, implies that magnetic anomalies with N-S distribution can be resolved better.

As a first step a bandpass filter was applied. The calculation of the power spectrum was done using the classical, discrete Fourier transform representation in the wavenumber domain (Fig 6.3). The spectrum revealed some directionality due to the linear character of the fence and the target. It also showed a concentration of energy at some distinct wavenumber zones, an indication that finite dimension anomalies exist on the map. For the bandpass filtering we applied the windowing method. The design of the two-dimensional filter was based on the extension of a one-dimensional Hanning window with rectangular support (Dudgeon and Mersereau, 1984). The magnitude of the inpulse response and frequency response of the bandpass filter are shown in figures 6.4(a) and 6.4(b) respectively, while the filtered map, as well as the residual anomaly are shown in figures 6.5(a) and 6.5(b). From these figures we can notice four well defined anomalies rectangular in shape (three of them 50x20 ft,

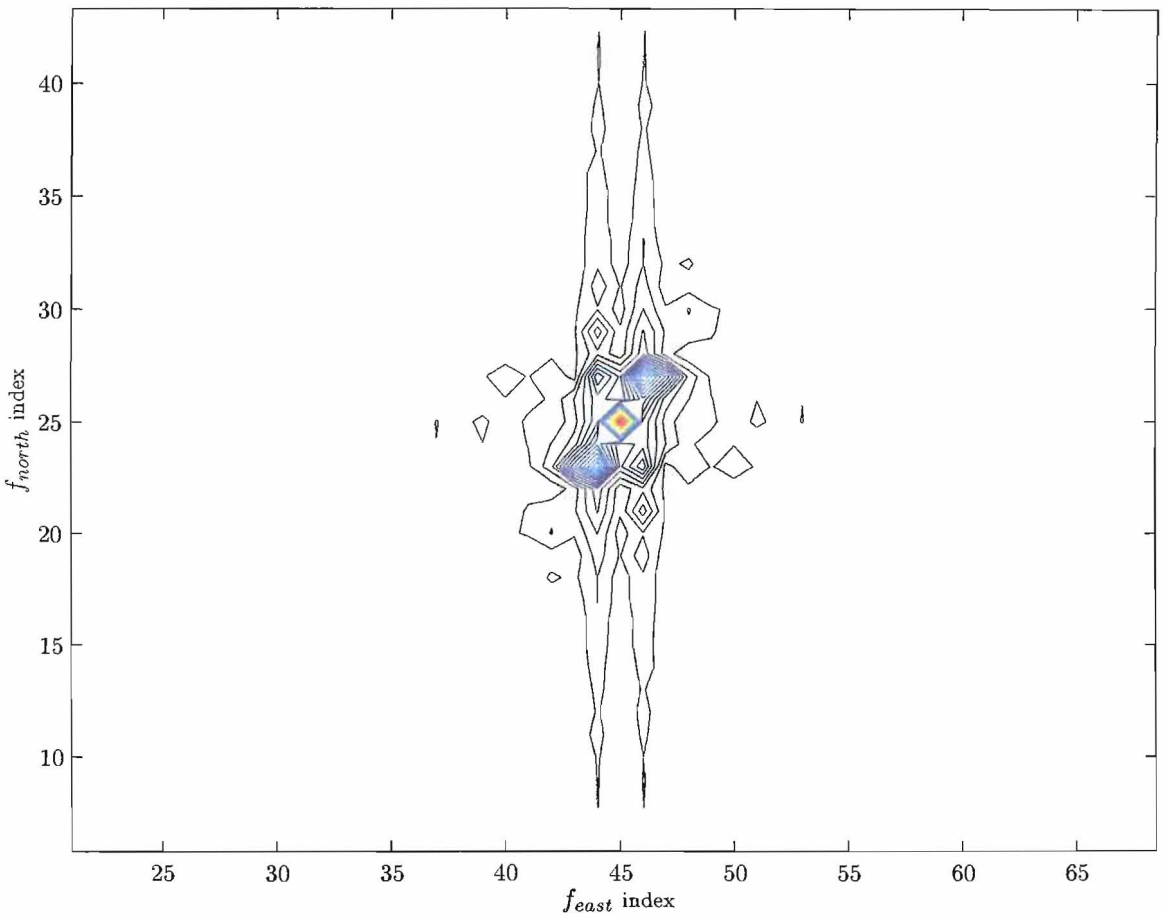

Figure 6.3: Spectrum of Magnetic anomaly at EPA.

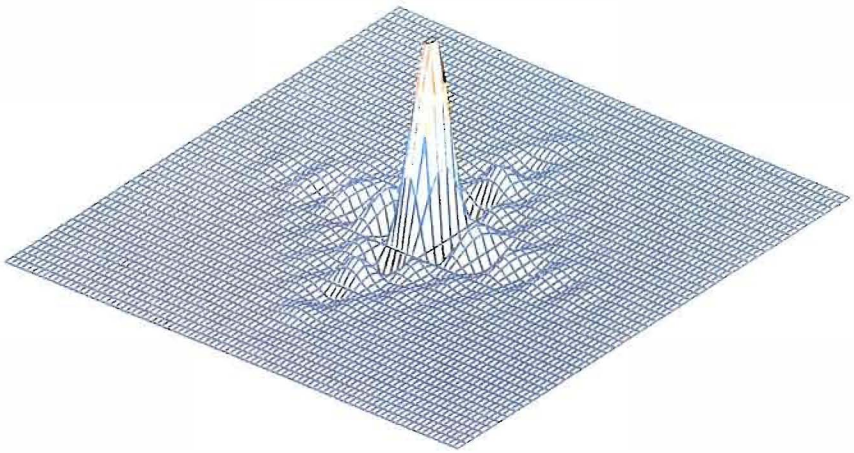

(a) Inpulse response

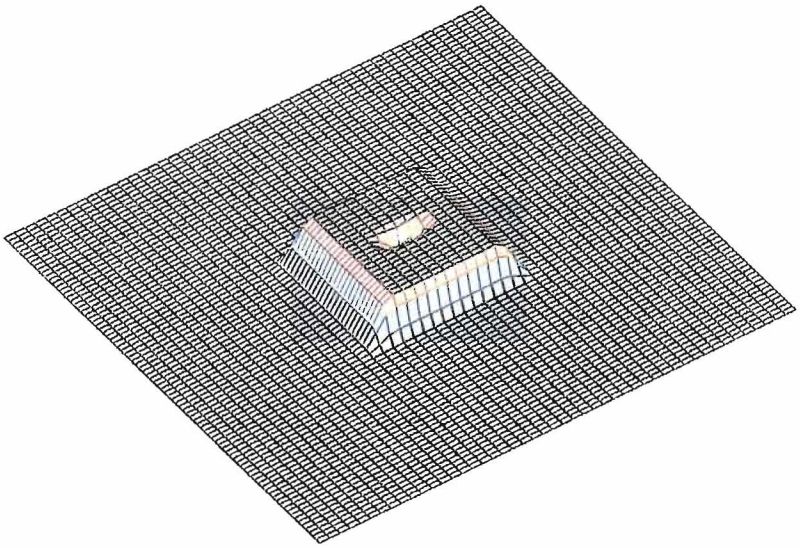

(b) Frequency response

Figure 6.4: FIR bandpass filter implementation for EPA.
Inpulse and frequency responses.

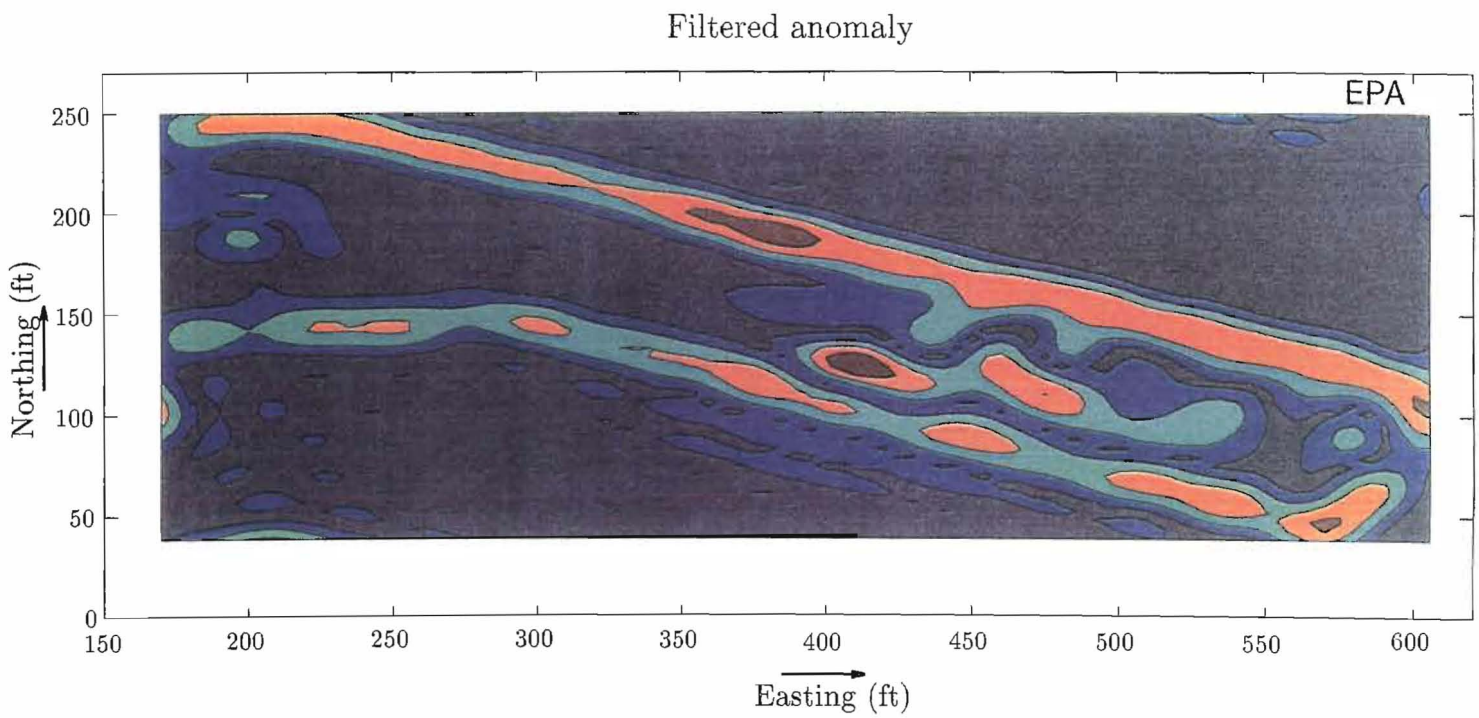

(a) Filtered map

Figure 6.5: Filtered magnetic anomaly and its residual at EPA.

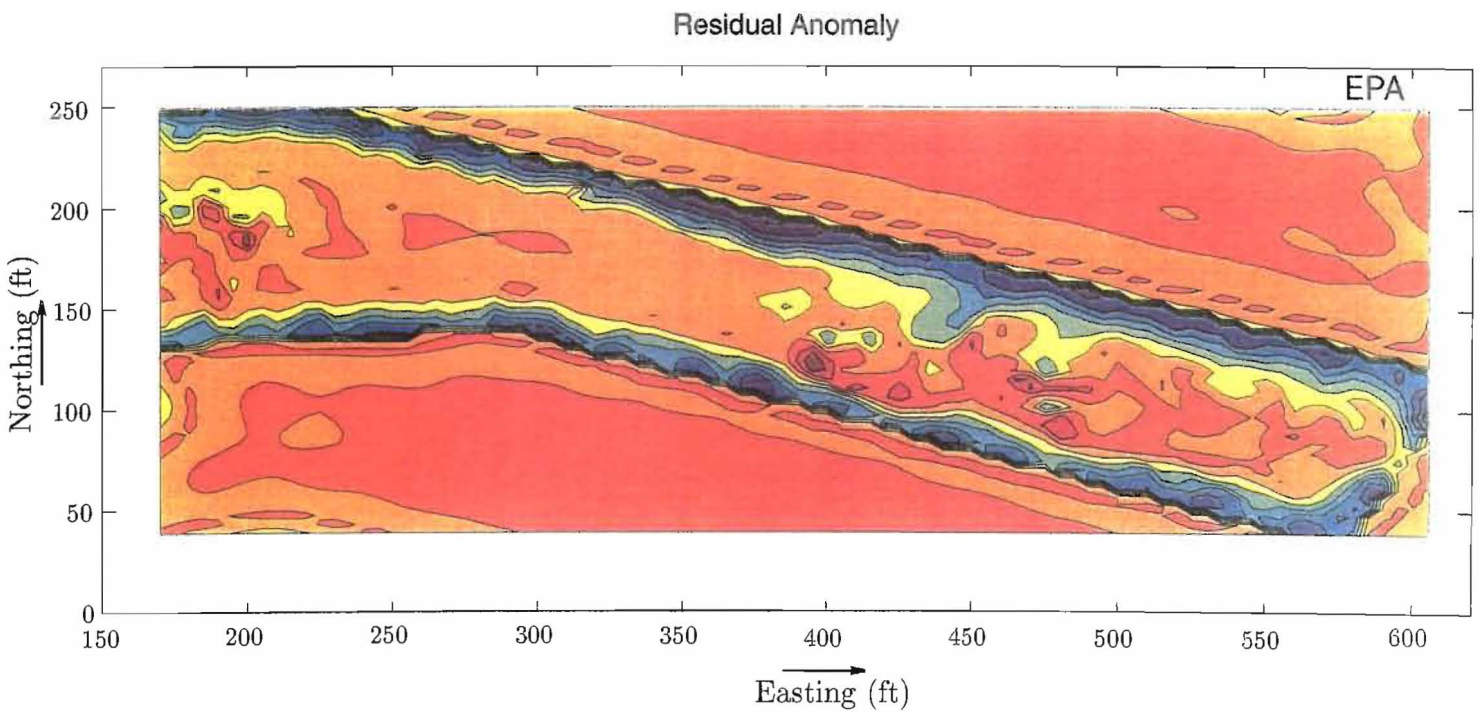

(b) Residual map

Figure 6.5: (Con't) Filtered magnetic anomaly and its residual at EPA.

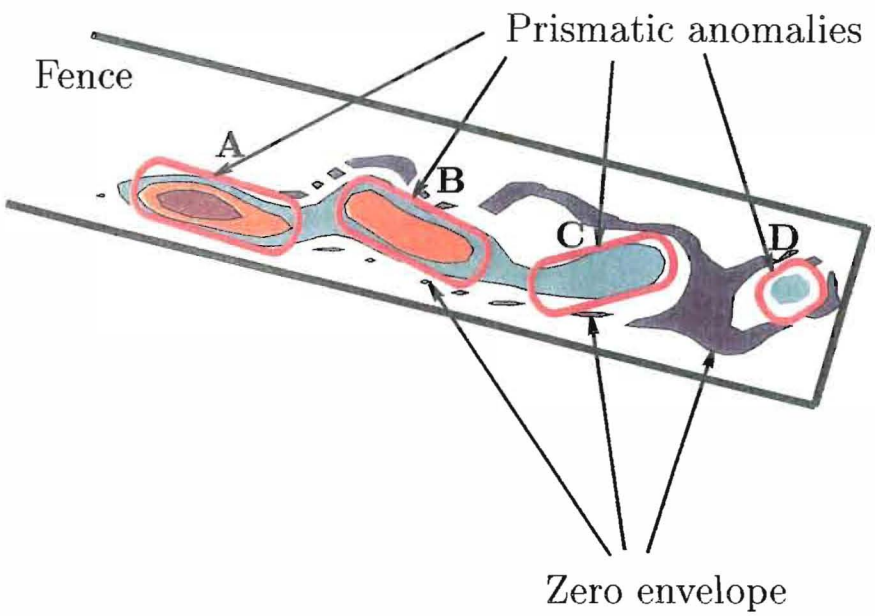

Figure 6.6: Magnetic anomalies at EPA.

and a fourth one 15x15 ft located at the eastern corner Fig 6.6). Higher frequency anomalies mainly correspond to the first two of the above anomalies and secondary to amplified noise as in figure 6.5(b). Another task was the calculation of an upward

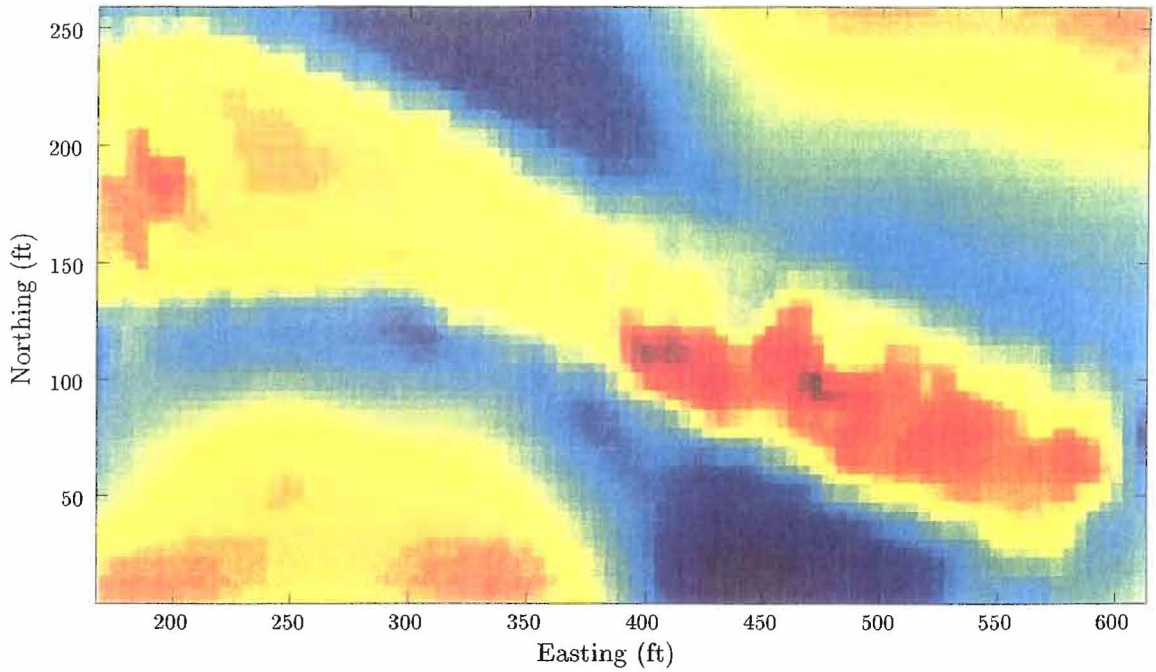

Figure 6.7: Upward continuation 2.5 ft of reduced to the pole magnetic anomaly at EPA.

continuation version of the map. The map was first reducted to the pole assuming polarization directions of the ambient field and then the continuation at 2.5 ft above the initial level was calculated (Fig 6.7).

6.2.2 Western Paved Area

The western -and middle- end of the paved area (WPA) is elongated and rectangular in shape, and is the largest portion of the paved area (Fig 6.8). At a first view, magnetic anomalies seem to be dispersed longitudinally and concentrated in the middle of the area. There are three big, distinct anomalies that dominate the right end. The

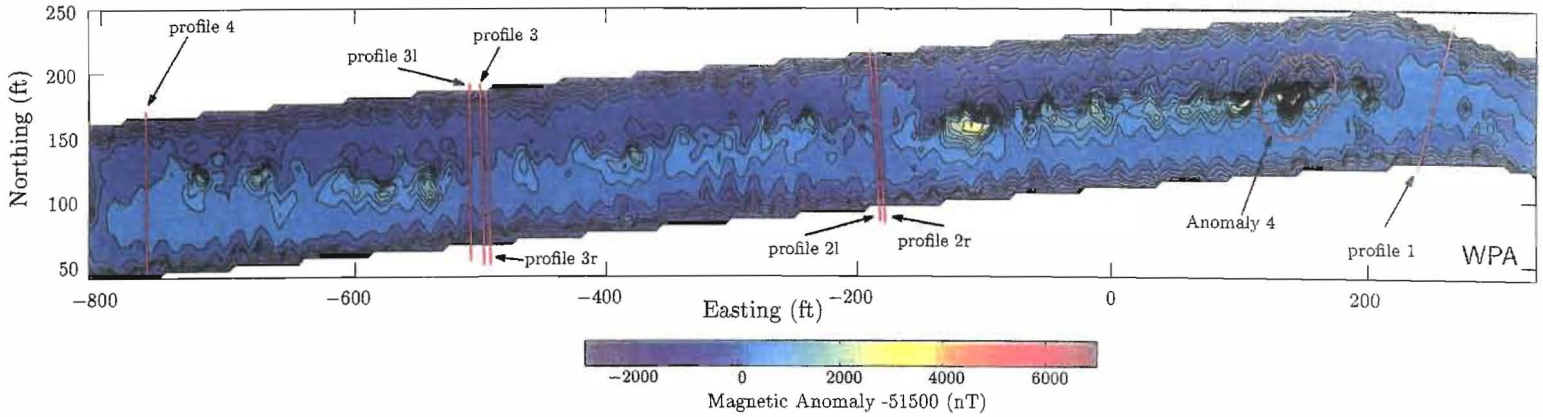

Figure 6.8: Magnetic anomaly at Western Paved Area.

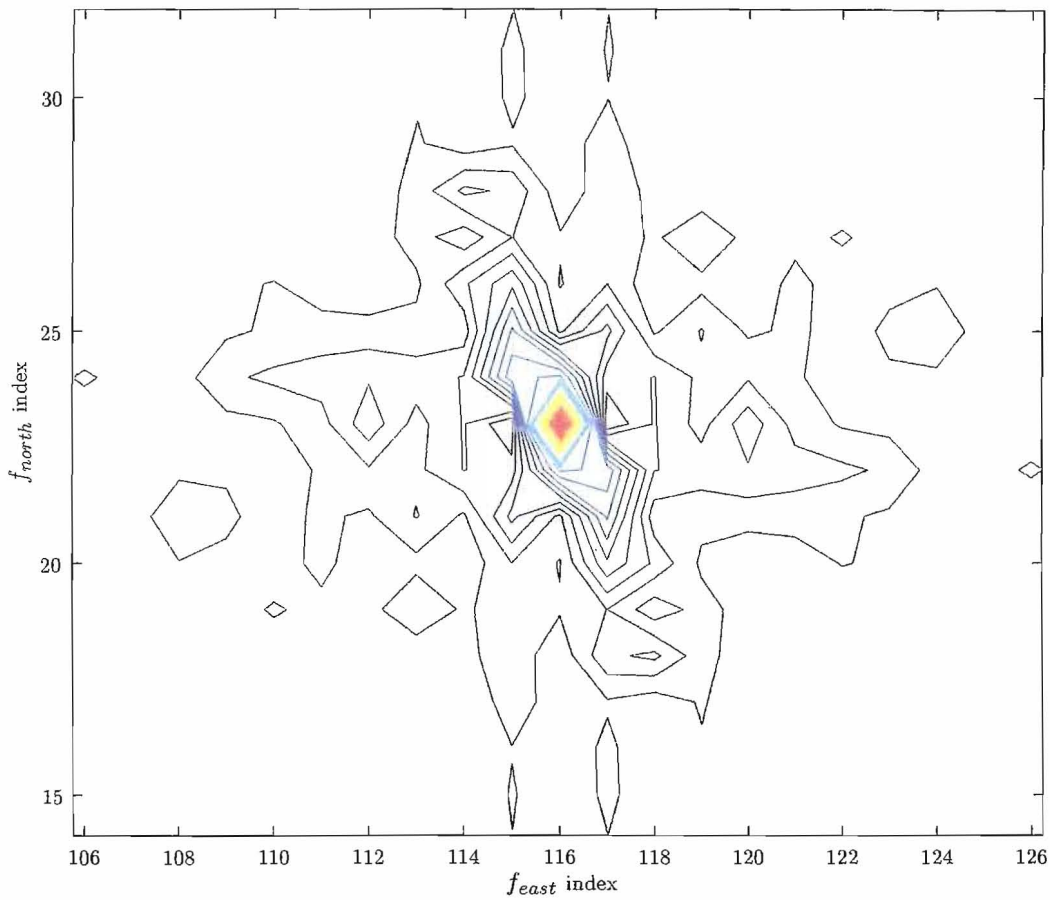

Figure 6.9: Spectrum of magnetic anomaly at WPA.

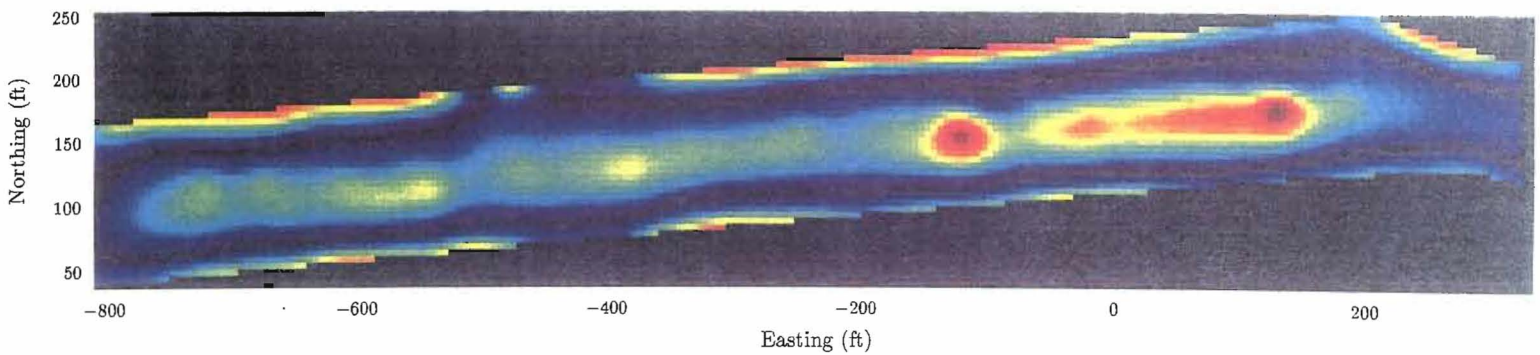

Figure 6.10: Upward continuation 8.2 ft of reduced to the pole magnetic anomaly at WPA.

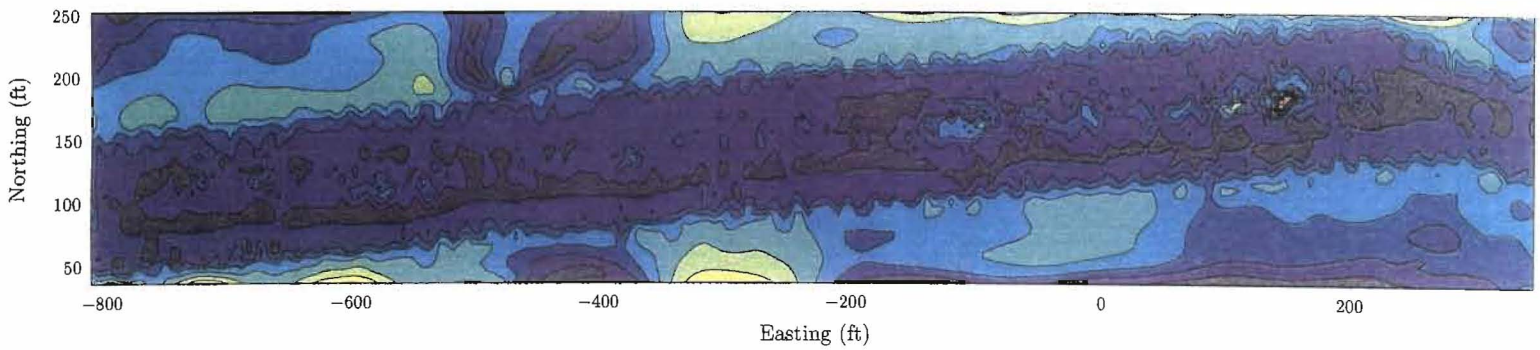

Figure 6.11: Bandpass (25-40 ft) filtered anomaly at WPA.

processing of the magnetic signal was the same as in the Eastern Paved Area. Once more, reduction to the pole-upward continuation, first vertical derivative and band-pass filtering was applied (Fig 6.9, 6.10 and 6.11). The bandpass filter was obtain using a 2D Hanning window at the 5.0 - 8.0 ft wavelength band, and the main goal here was to remove the magnetic contribution of the fence.

6.2.3 L-Shaped Area

The L-shaped area (LSA) comprise the western end of the site and it is surrounded by a fence. The one half is paved and can be taken as the extension of WPA separated by a short block wall, while the other half is unpaved (WUA) and forms an L-shaped body when is viewed in conjunction with the WPA. Except a small edge anomaly along the boundary with WPA, this site appears to be magnetically quiet; hence there was no particular processing at LSA (Fig 6.12). We will refer to this area as either LSA or WUA depending on the context. Usually magnetic data refer to LSA as a whole, while in the seismic survey the unpaved part of LSA (WUA) is treated as a separate unit.

6.2.4 Eastern Unpaved Area

Finally, the last part of the site is the Eastern Unpaved Area or EUA (Fig 6.13). Its spectrum is similar with that at EPA (Fig 6.3) except at the very low frequencies (long wavelengths) where at EUA is almost diminished (Fig 6.14). This is due to the clipping of the anomaly and the absence of the fence signal. Therefore, the remaining signal may be attributed to sources with origin strictly related to the site. A low-pass filtered version of the map can be seen in figure 6.15, where each pixel corresponds to the magnitude of the signal at that point. In this map a reduction to the pole filter

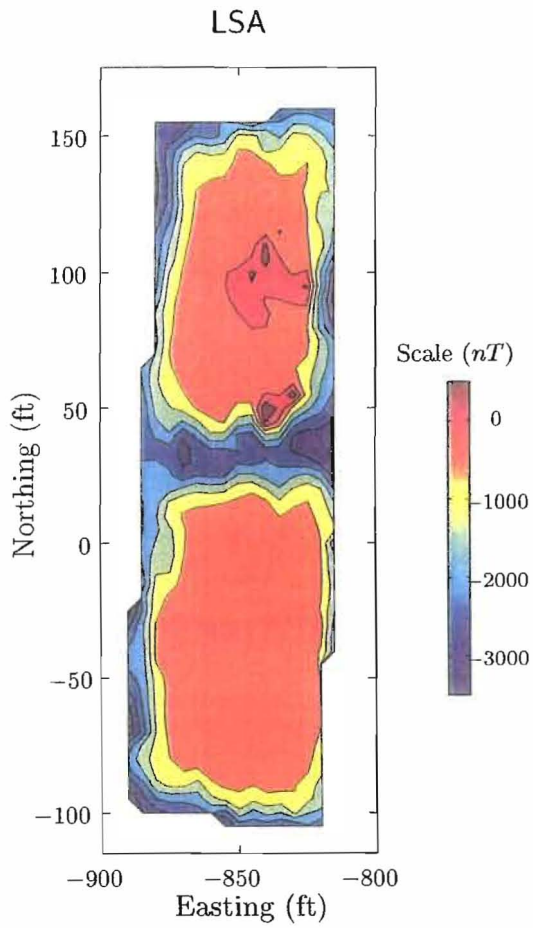

Figure 6.12: Magnetic anomaly at LSA (-51500 nT).

was previously applied.

6.3 Magnetic Modeling Method

Estimation of the geometry of the source(s) can be done by forward modeling, a trial and error technique. The assumed model is modified until its calculated anomaly fits the observed data. Many techniques have appeared in geophysical literature on the calculation of magnetic anomalies of regular or irregular bodies e.g. (Talwani, 1965). Most of them utilize either approximation of the body to a model bounded by first-order surfaces and calculating the effect of each face, or dividing the body into thin horizontal plates, calculating the effects and summing between depth limits. There are also examples of inverse modeling somewhat idealized but they are usually applied in cases where neither the signal is too much contaminated with noise nor the model is very complex. In this study the calculation of the magnetic anomaly of three dimensional bodies uses the first approach; in particular, a rectangular prism is used. This kind of prism has also been used in inverse methods to derive the vector $\mathbf{M}$ from the total field anomaly.

First of all, an elementary body, which approximates the structure, is found. In this case it is a collection of rectangular prisms (Fig 6.1). The prisms must fulfill the conditions of the whole range of the structures. The physical material parameter is the magnetization. The model should be comprehensible to the user and not overloaded with details. The total magnetic field of the rectangular prism was first derived by Bhattacharyya in the spirit of equation 6.3, $\Delta T = -C_m \hat{\mathbf{F}} \cdot \nabla_P \int_R \mathbf{M}(Q) \cdot \nabla_Q(\frac{1}{r}) dv$,

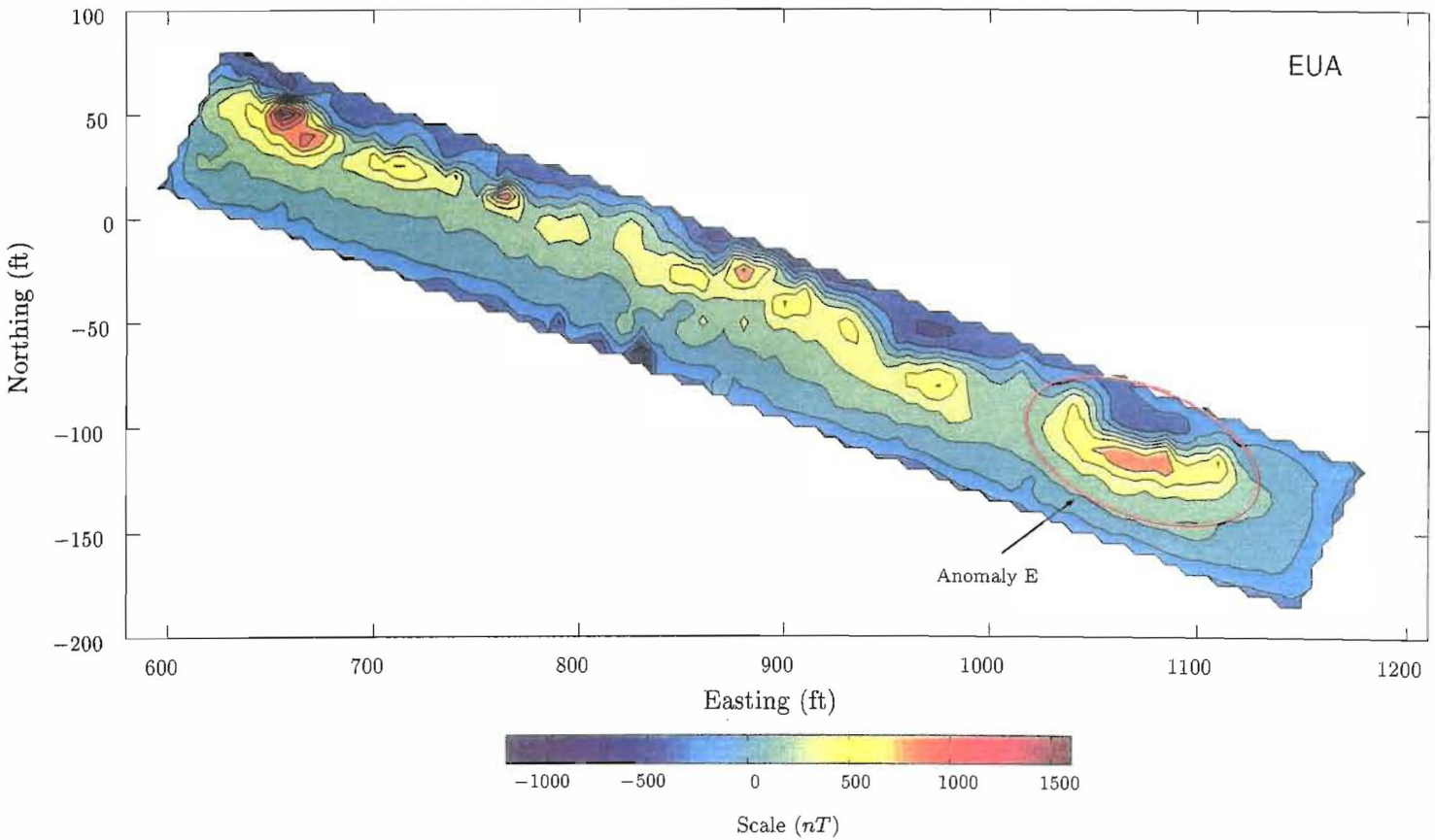

Figure 6.13: Magnetic anomaly at Eastern Unpaved Area (-51500 nT).

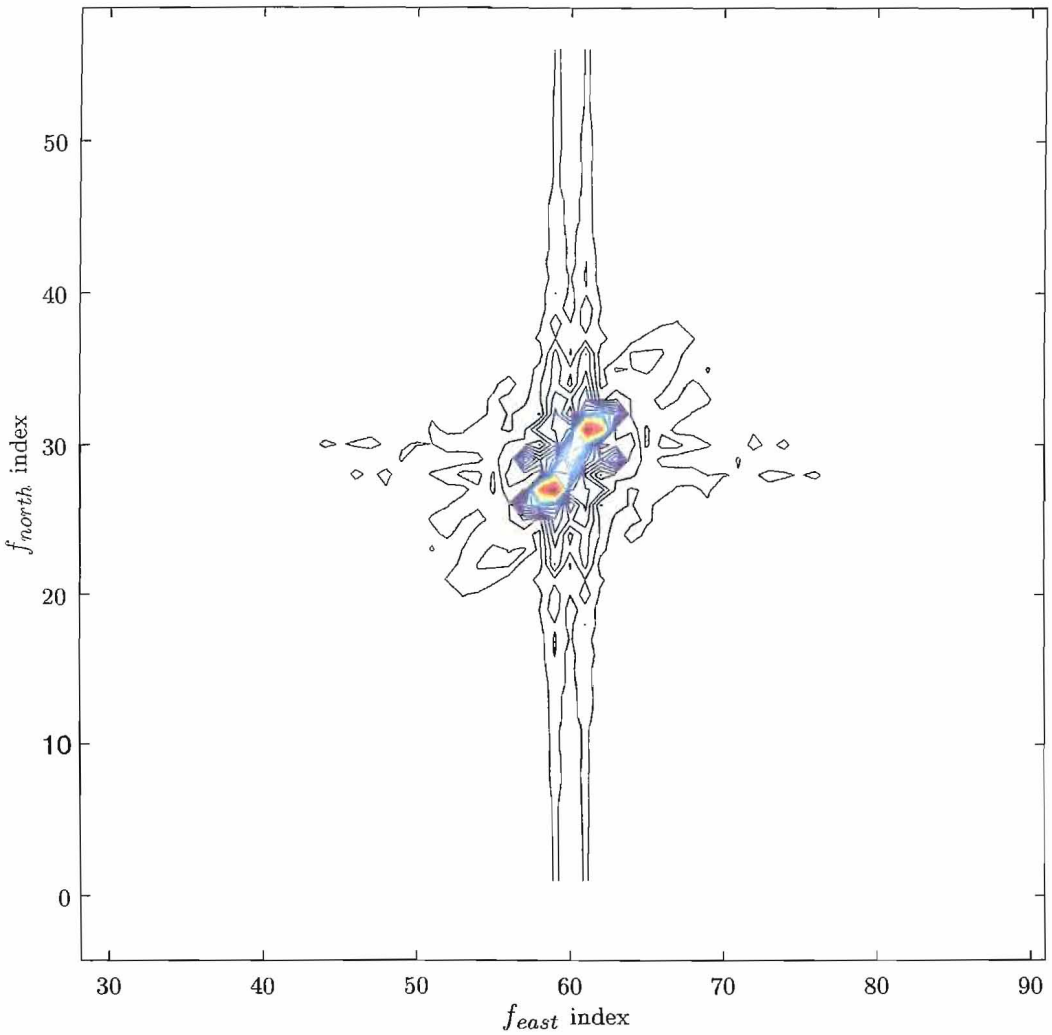

Figure 6.14: Spectrum of magnetic anomaly at EUA.

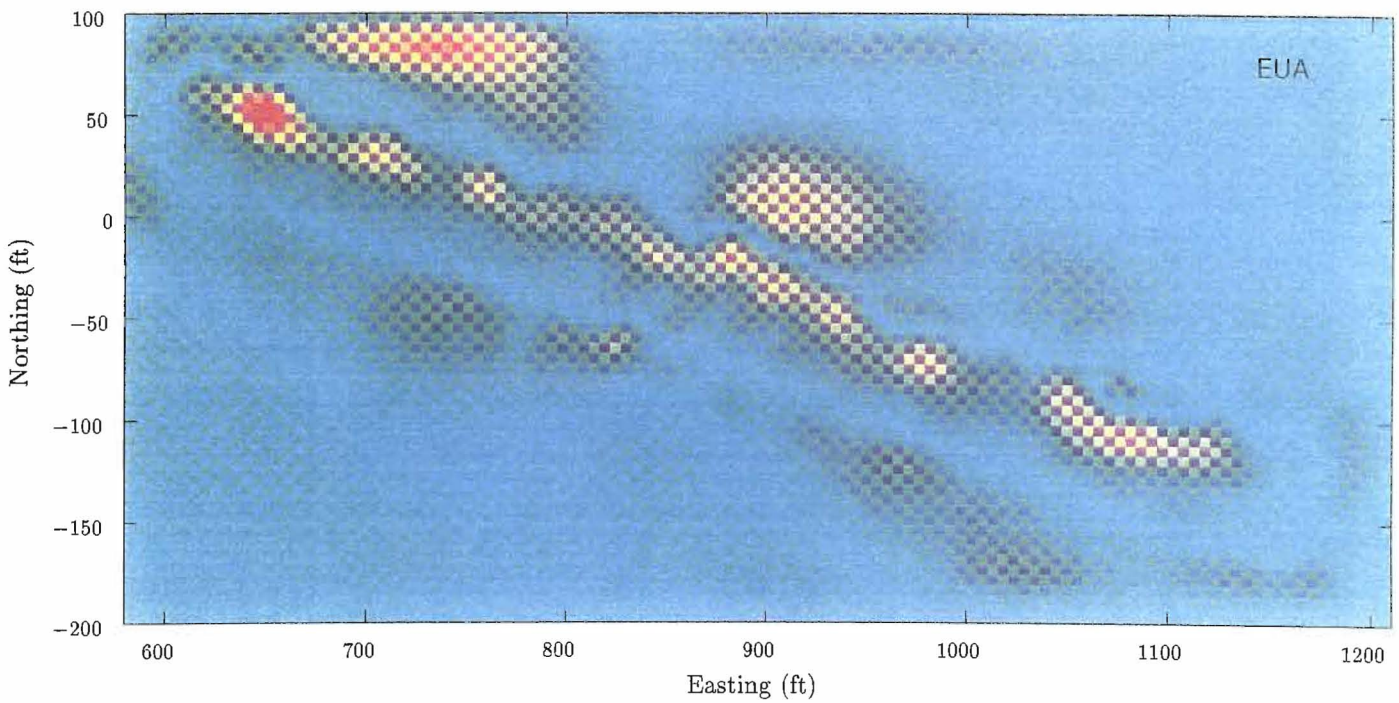

Figure 6.15: Filtered map of magnetic anomaly at EUA.

which in discretized form becomes (Bhattacharyya, 1964)

$$\Delta T = C_m \left[\frac{\alpha_{23}}{2} \log\left(\frac{r - x'}{r + x'}\right) + \frac{\alpha_{13}}{2} \log\left(\frac{r - y'}{r + y'}\right) - \alpha_{23} \log(r + z_1) \right.$$
$$- \hat{\mathrm{M}}_{\mathrm{x}}\hat{\mathrm{F}}_{\mathrm{x}} \arctan\left(\frac{x'y'}{x'^2 + rz_1 + z_1{}^2}\right) - \hat{\mathrm{M}}_{\mathrm{y}}\hat{\mathrm{F}}_{\mathrm{y}} \arctan\left(\frac{x'y'}{r'^2 + rz_1 + x'^2}\right) \tag{6.4}$$
$$\left. - \hat{\mathrm{M}}_{\mathrm{z}}\hat{\mathrm{F}}_{\mathrm{z}} \arctan\left(\frac{x'y'}{rz_1}\right)\right] \Bigg|_{x'=x_1}^{x'=x_2} \Bigg|_{y'=y_1}^{y'=y_2}$$

$\mathbf{F} = (\hat{\mathrm{F}}_{\mathrm{x}}, \hat{\mathrm{F}}_{\mathrm{y}}, \hat{\mathrm{F}}_{\mathrm{z}})$	: is the unit vector having the direction of the ambient field
$\mathrm{M} = M(\hat{\mathrm{M}}_{\mathrm{x}}, \hat{\mathrm{M}}_{\mathrm{y}}, \hat{\mathrm{M}}_{\mathrm{z}})$	: is the magnetization vector
r	: is the distance to the source of the anomaly Q from the observation point P (Fig. 6.1).

Each prism is oriented parallel to the x, y, and z axes and has magnetization $\mathbf{M} = M(\mathbf{i}\hat{M}x + \mathbf{j}\hat{M}y + \mathbf{k}\hat{M}z)$ and dimensions $x_1 < x < x_2$, $y_1 < y < y_2$, and $z_1 < z < \infty$. The expression of the total field in closed form is derived on the assumption of uniform magnetization throughout the body. Without this assumption, analysis of the problem is practically impossible because we do not know the distribution of M within the body. The total anomaly of the prism is calculated using equation 6.4 two times with corresponding depths z_1 and z_2 and subtracting the results.Therefore the modeling was based on equations 6.3 and 6.4.

6.3.1 The modeling program

Blakely(1995) based on the Bhattacharyya equation, suggested a Fortran subroutine that implements equation 6.4 to calculate the total field anomaly. The implementation of that subroutine into `Matlab`© code is shown in Appendix A, and was used as the core routine to calculate the synthetic anomaly of a single prism. A modeling program

then, also in `Matlab`©, was written to compute the total anomaly of an accumulation of prisms, allowing each one to have different magnetic properties and dimensions.

Chapter 7

Seismic Modeling

For each of the acquired seismic lines a model was constructed. The modeling was achieved tracking the wavefronts through a two-dimensional model (Ferguson et al., 1994). This method is currently employed in the `geomod` program (a collection of `Matlab`© functions for seismic and/or gravity modeling). Specifically, we assume that the subsurface can be represented as a number of polygons that span the two dimensional cross-sectional area, each one having a constant velocity distribution.The polygons may correspond to different media, either geologic (tuff, weathering layer) or to man-made structures (trenches, landfill). In each case a specific configuration of these polygons is constructed for each line. As was earlier mentioned, the major advantage of wavefront extrapolation over ray tracing is that it allows a high velocity contrast between the polygons, a likely feature for this site. A uniform rectangular grid was then applied to the model as in Fig. 4.1(a), and the slowness values for each cell of the grid were assigned based on the geometry of the polygons. The grid interval was determined based on the complexity of the model and the desired accuracy; in most of the models it was $1ft \times 1ft$.

As an initial model a simple multi-layer configuration based on Lines 18 and 19 was

used, that clearly do not appear to include any anomalous velocity distribution. These same lines also gave a good first estimation of the velocities of the undisturbed geology, using the slope/intercept-time method. Then the starting models were iteratively and interactively modified. The synthetic traveltimes for the models were calculated and compared to the picked first-arrival traveltimes. Once the model fit the data well it was considered acceptable. The data fitness was determined based mainly on the quality of the data. Since the seismic noise and signal attenuation varied among the lines the error threshold also varied. Thus there was no definite numerical value for the acceptable residual norm. The models were accepted as final based on i) an overall visual inspection ii) an agreement of the apparent velocity between the observed and calculated data and iii) the match of certain parts (inflections) of the traveltime curves. The last one especially can indicate the lateral boundaries as well as the depth extent of the trenches. Another question that arises here is the uniqueness of the model. Again, we know that the problem of calculating the depths and velocities of the refraction horizons involves a large number of parameters, generally more than the number of data; it is thus non-unique. Hence extra information is needed to constrain the number of the solutions (Ackermann et al., 1986). This extra information comes from the additional shots on the same line. Furthermore, the survey resolution that depends on the space interval between the geophones determines how well we can separate and identify inflection points, and calculate apparent velocities from the traveltime curves. In this survey the horizontal resolution was approximately $3ft$, and the vertical at least as good or better.

Finally, an attempt was made to keep the model geometry and the number of layers as simple as possible. Thus, special attention was paid to the simplicity of the constructed models rather than to the absolute data fit.

Chapter 8

Interpretation

8.1 The Magnetic data

8.1.1 Eastern Paved Area

Bandpass filtered map (Fig 6.5) supports the belief that the magnetic anomaly at EPA cannot be attributed to deep seated sources (e.g of geologic origin). On the other hand, the upward continuation map (Fig 6.7) clearly portrays the presence of a magnetic source different than in the anomalies A,B,C, or D. Similar in shape is the zero envelope of the bandpass filtered map(Fig 6.6). This combined with the observation that at the northern edge of the map the gradient is not as step as the east and south edges, is a strong evidence of a trench-fill magnetic anomaly. The shape of the trench can be better shown in the upward continuation map. In this map (Fig 6.7) the trench signal appears to be rectangular in shape even at the SE corner. The band pass filtered map mainly enhances the combined effect of the individual sources, and to a lesser degree the anomaly of the pit. This result is achieved after rejection of i) the high frequency signal (wavelengths less than 25 ft) and ii) the very long wavelengths (greater than 50 ft at the North-South direction).

The southern boundary of the pit cannot be easily resolved from these data because of the fence proximity. The anomaly D as seen in the total field map (Fig 6.2) appears to extend outside of the east end of the site, toward the unpaved area.

8.1.2 Western paved Area

The net magnetic anomaly of the trenches at WPA cannot be estimated by filtering due to overlapping effects in the wavenumber domain. Therefore, this anomaly may only be seen in profiles that do not cross any major nearby sources. Furthermore, these profiles can be expected to have reverse polarization (negative part toward South) and mean amplitude (positive lobe) of order of around 200 nT. However this anomaly is obscured by the magnetic bodies buried with in it and the strong magnetic anomaly of the fences, and cannot be seen in the map. It is worth-noticing that at profiles 2r and 3l the anomaly is diminished, an indication that the tuff there remained intact (Figs. 6.8, 8.1).

Most of the other kinds of magnetic sources are at shallow depth (1-3 m) and yield steep gradients. This can be seen in the first vertical and/or horizontal derivatives, the high-pass filtered or the downward continuation maps (e.g. Fig 8.2). These shallow sources mask any smaller amplitude underneath anomalies. Consequently, the later can be recognized only at some distance away from the local anomalies taking advantage of the longer wavelengths. Another aspect that must be considered for this part of the site, as well, is the strong interference with the surrounding fence. The biggest part of the fence magnetic effect is attributed to the poles rather than the chainlink. The applied bandpass filter with wavelength range 5-30 ft illustrates the above statement (Fig 8.3). From this map the calculated period(spacing) of the poles is about 20.5 ft. In addition the complement of this filter provides the residual

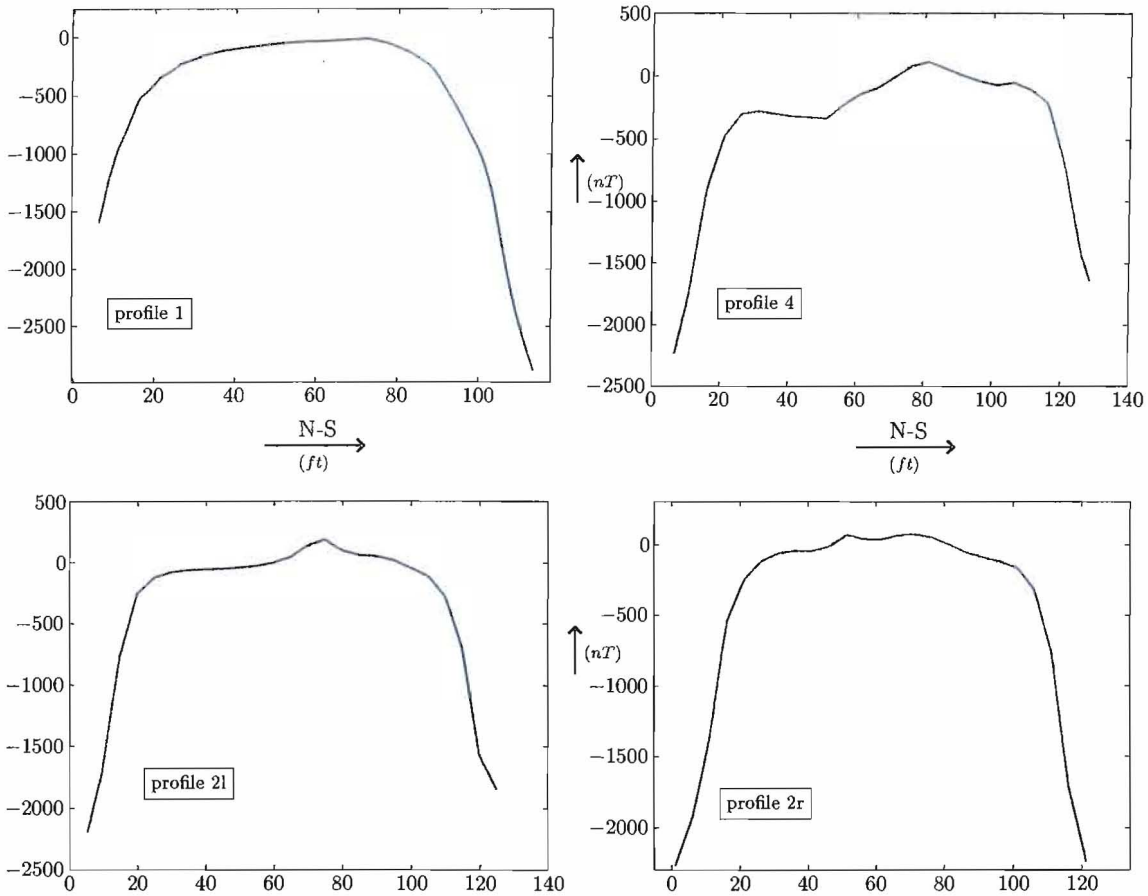

(a) profiles 1, 2r, 2l, and 4

Figure 8.1: Magnetic profiles along WPA. (see Fig. 6.8 for profile location)

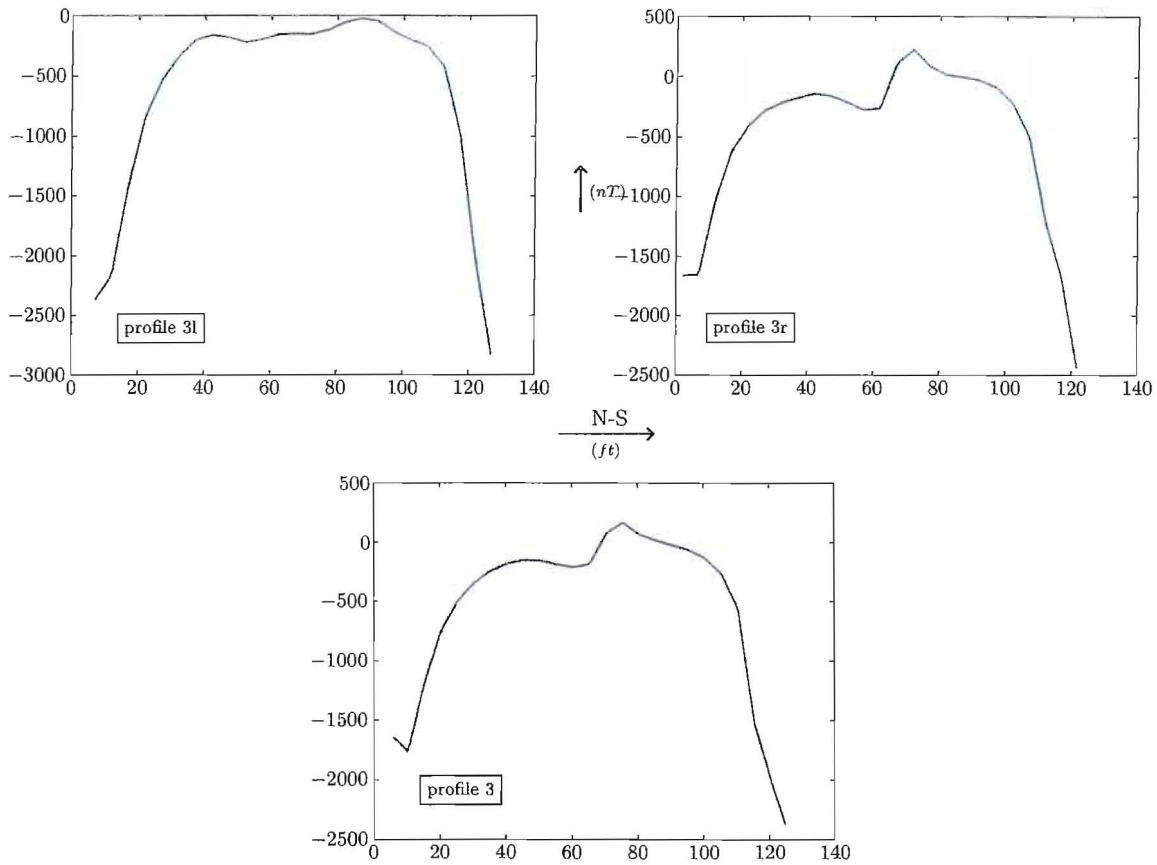

(b) Profiles 3r, 3, and 3l

Figure 8.1: (cont) Magnetic profiles along WPA.

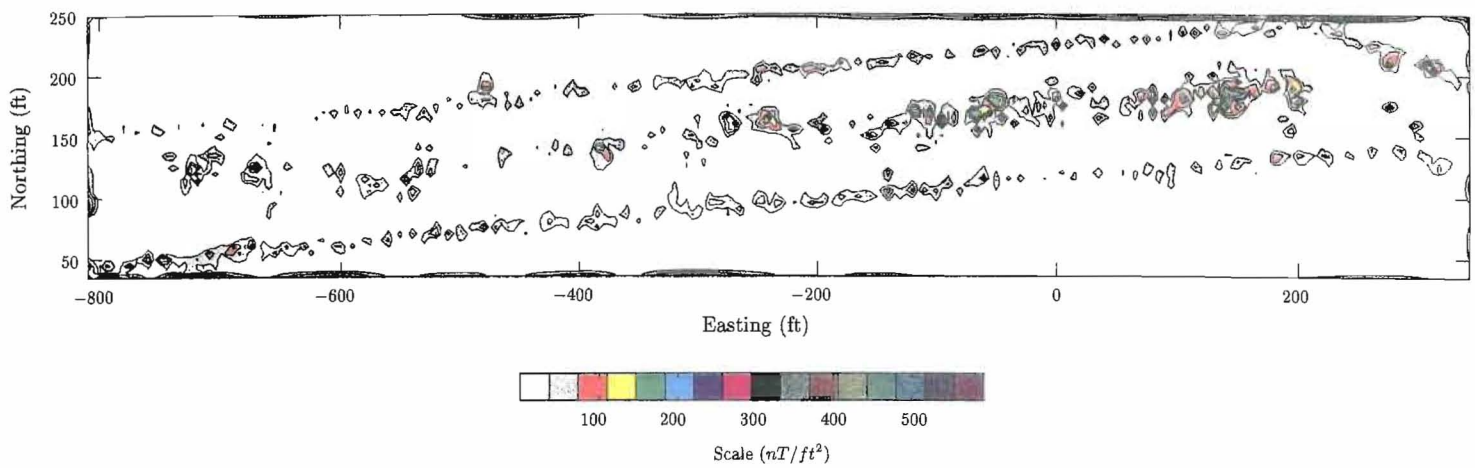

Figure 8.2: Second derivative of magnetic field at WPA. This high pass filter emphasizes shallow sources and delineates their boundaries.

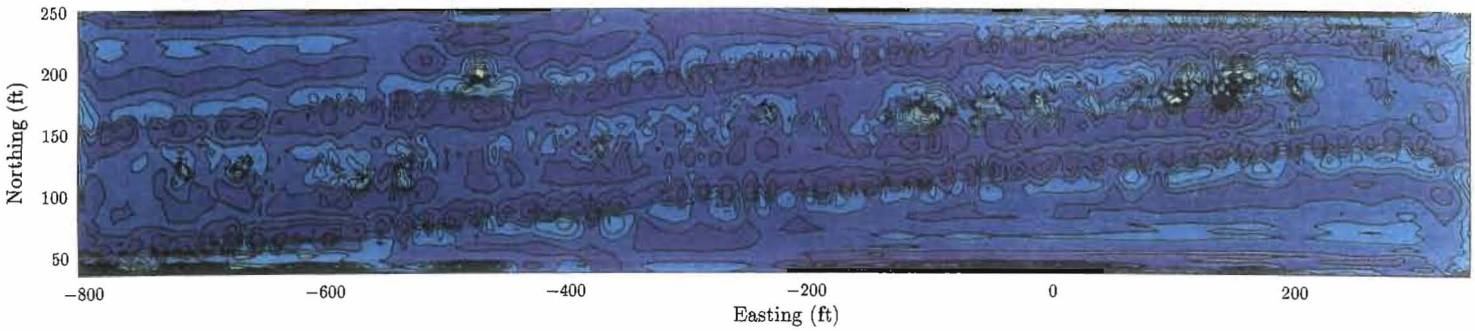

Figure 8.3: Filtered map (5-30ft) of magnetic field at WPA.

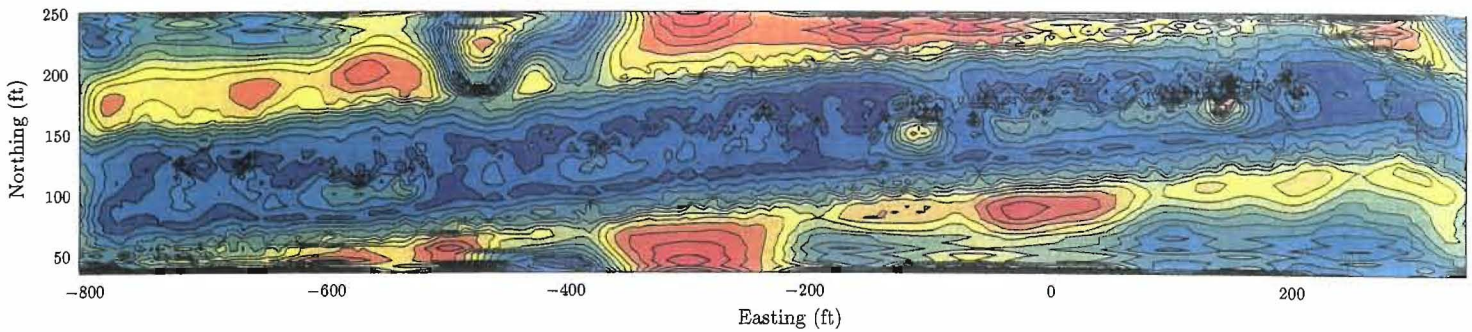

Figure 8.4: Residual of the previous filtered map [0 5) & (30 $+\infty$) ft, at WPA.

(band-cut filtered) map (Fig 8.4). The poles of the fence are also responsible for the waving shape of the anomaly near the edges. However, it is the contouring algorithm (minimum curvature) that propagates this pattern into the neighboring areas that have low gradients. Indeed, the waving character of the outer contours that outline the anomalies of the trench is an artificial effect attributed to the gridding minimum curvature algorithm (Briggs, 1974).

Filtering in the wavelength band 25-40 ft reveals a particular arrangement of the anomalies within the area. Again, the WPA seems to consists of three separate, main magnetic areas (Fig 6.11), with the dominating shallow-depth sources signal superimposed to the signal of deeper and broader anomalies and that to the fence. In agreement, the upward continuation of the pole-reduced map (Fig 6.10) clearly indicates the presence of three separated features that corresponds to three individual trenches.

WPA hosts at the eastern end the biggest anomaly of MDA-B, with magnitude up to $\sim 10000nT$ (Fig 8.5). Magnetic modeling also of this anomaly (see also Fig. 6.8, anomaly 4) indicates that the high magnitude is due to the shallowness of strong magnetic bodies (Fig 8.6).

8.1.3 Eastern Unpaved Area

The magnetic anomalies in Eastern Unpaved Area (EUA) appear to be smoother and lower in magnitude compared to the other areas, due to the existence of the experimental soil cap. Also it is worth noticing that since the acquired map was restricted within a rectangular area and did not cover the whole site, most of the negative parts

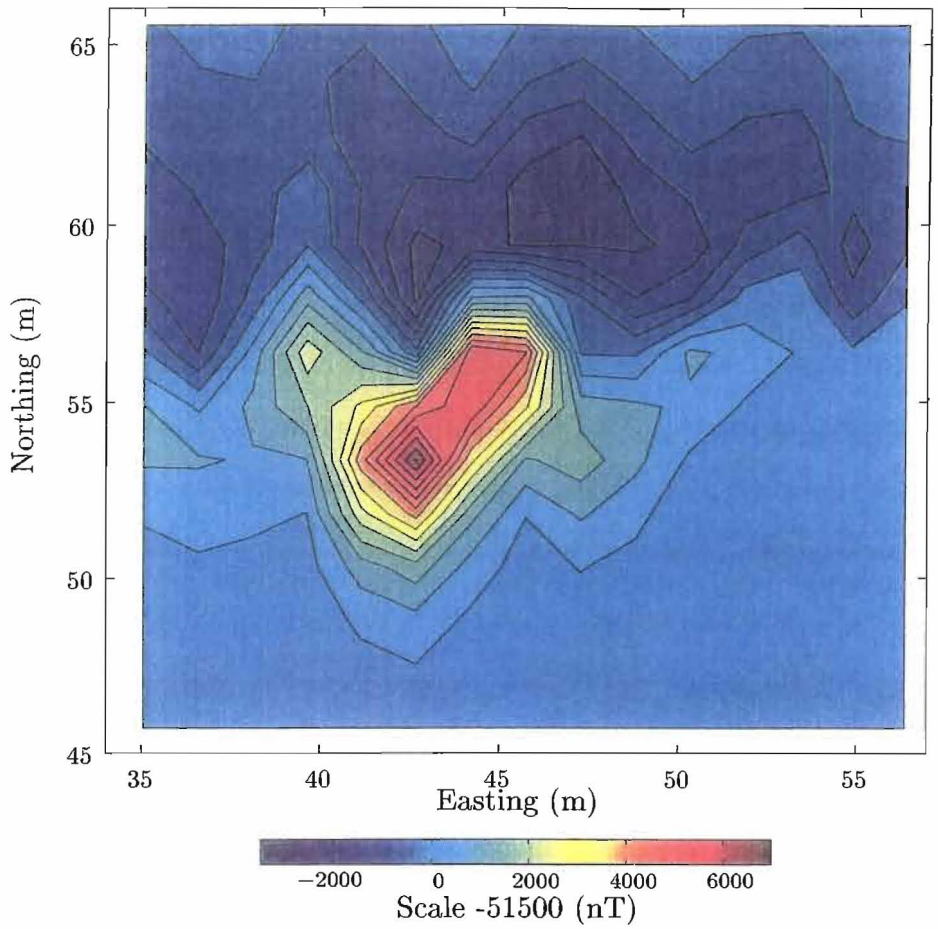

Figure 8.5: Observed anomaly (4) at WPA.

of the anomalies are missing. This corresponds to applying a rectangular window to our data in the space domain, an event that leads to a smoothing of the spectrum in the wavenumber domain(power leakage). The upward continuation and the low-pass filtered version of the total map (Fig 6.15) supports the hypothesis of one big elongated trench, most probably extended toward the west end, and continued in the eastern paved part.

In this area a well-defined anomaly (Fig. 8.7 appears at the western end, probably

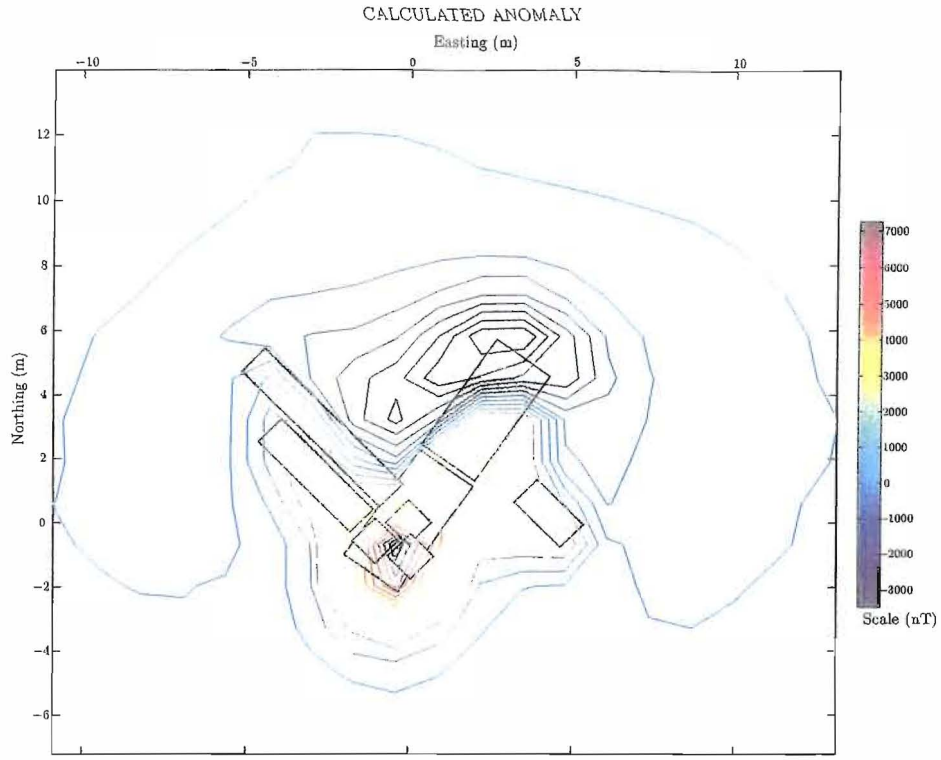

Figure 8.6: Modeled anomaly (4) at WPA. Contours represent total field anomaly of a distribution of magnetic bodies (prisms).

the beginning of the trench (Fig 6.13, anomaly E). This anomaly has been modeled and yields depths to the top of the big prisms of about $2-3m$. A possible model for that anomaly appears in figure 8.8.

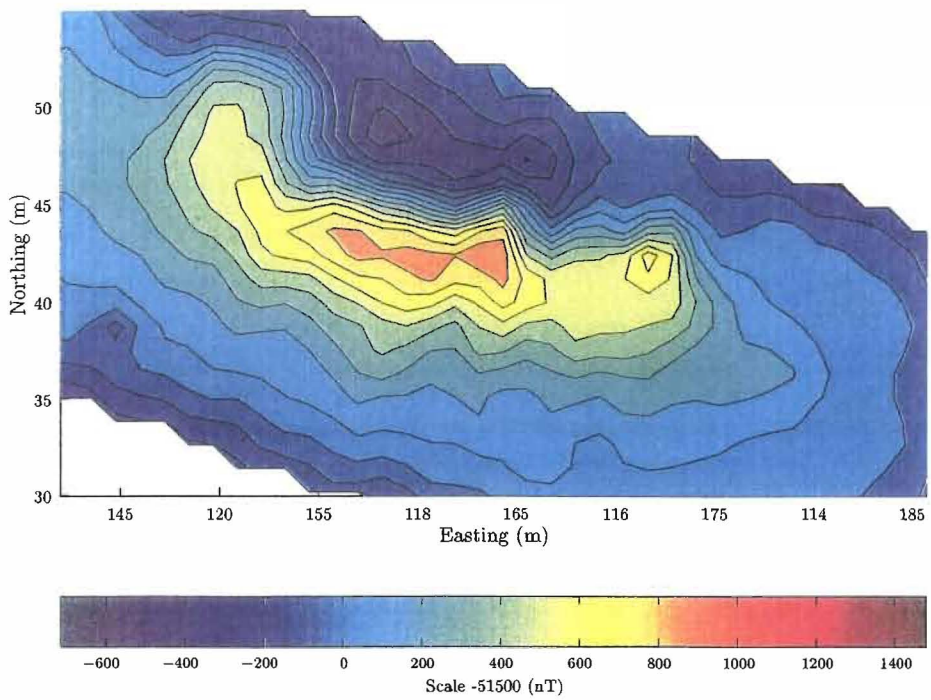

Figure 8.7: Observed anomaly (E) at EUA.

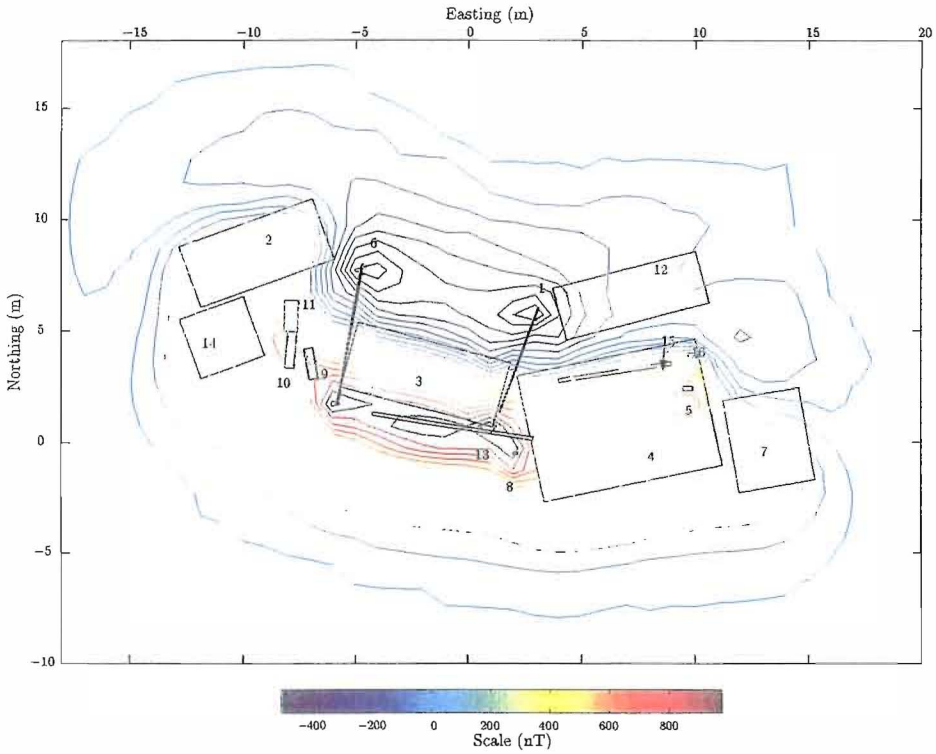

Figure 8.8: Modeled anomaly (E) at EUA. Contours represent total field anomaly of a distribution of magnetic bodies (prisms).

8.2 The Seismic data

In many cases and for simple models, we expect the number of line segments in the traveltime plots to be equal to the number of layers(velocity areas). For more complex models, and especially for configurations with local velocity inversion the above rule does not hold. Nevertheless, as was stated in Chapter 4, small scale velocities inversions are acceptable as far as they can be detected in the seismograms (e.g. Fig. 5.3).

Another issue that affects the interpretation of the refraction data is the resolution of the survey. The survey horizontal resolution was about 1 m (Chapter 7), assuming a certain quality for the data. There were places where the asphalt and the high attenuation effects, especially at the long profiles, decreased the resolution both vertically and horizontally, (here with the term *decreased resolution* we mean that we are not able any more to resolve features as small as 1 m because a low signal to noise ratio). On the other hand, there were profiles where the quality and content of the data and the configuration of the imaged structure was such that ambiguities were well resolved, yielding resolution even better than 1 m.

All the target structures were constructed within the Tshirege member-Unit 3 of the Bandelier tuff, a rather stratified volcanic unit partially and locally welded, and the alluvial cap. This fact reflects the differences in modeled velocities. Indeed, $P-wave$ velocities of the "bedrock" vary in the range of $2500-3200$ ft/s and reflect these inhomogeneities. Any other deviation from this range should be attributed to construction work that had been done at the site. In its larger extent, the Southern part of the site (being closer to the adjacent canyon) was leveled and partially filled with diverse material. This contributes to a drop in seismic velocities of about

200-500 ft/s relative to the undisturbed tuff.

8.2.1 Eastern Unpaved Area

A prototype plan for the effective closure of the whole site was applied in the EUA (Nyhan and Barnes, 1989). Eight experimental landfill cover systems within three well defined soil profiles were established for a variety of experiments (Fig 2.5). The topsoil used in the construction of the site cover material was classified as a sandy loam. Also, crushed Bandelier Tuff classified as a sandy clay was used as an overburden to the waste material (Fig 2.6). East and West control profiles differ in the amount of sandy clay loam. According to Nyhan and Barnes (1989) the west profile is more typical of landfill covers at Los Alamos. It consists of a topsoil about 15 cm thick that seats over a 85 cm layer of crushed tuff. The amount of topsoil(sandy clay loam) in the east profile is much higher because of the reconstruction in 1992. That contributes to much higher water holding capacity comparable to the west profile. In the middle there is a cobble and gravel profile covered by 45 cm of crushed tuff and 15 cm of topsoil. This profile is known also as the "biobarrier" profile because it prohibits capillary rise of moisture and consequently bio-intrusion. The above physical properties of the profiles directly affect the velocity of the P-waves as the later travel through them.

Line 19 8.9 supports a simple three-layered structure model where the experimental cap with average velocity 1000 ft/s and average thickness 7-8 ft is the first layer, while the undisturbed tuff is the second layer with modeled velocity 2600 ft/s. On top there is a very thin soil layer with very low velocity (550 ft/s). Seismic Lines 20 and 21 could not be modeled because of the high noise level, while Seismic Lines 1-5 were modeled by J. Ferguson after the summer of 1997 (Ferguson et al., 1998).

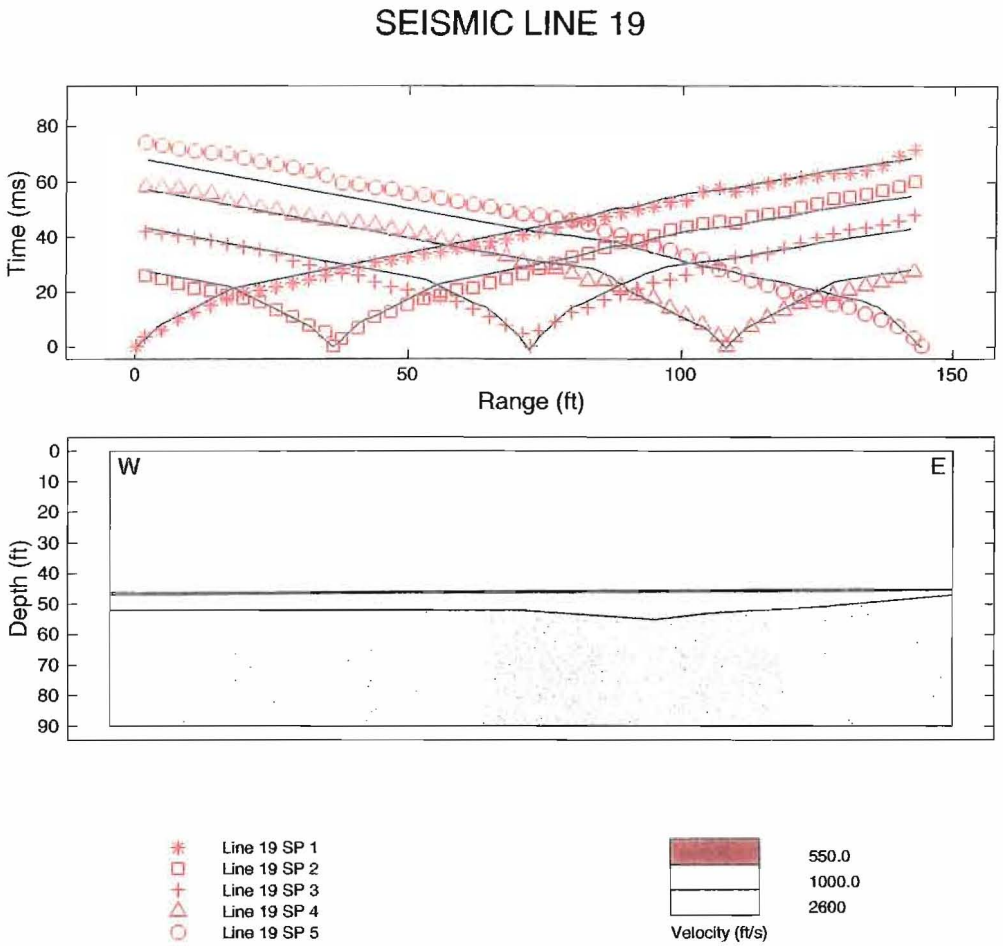

Figure 8.9: Travel times (red symbol observed, blue line computed), and corresponding model for line 19.

8.2.2 Eastern Paved Area

EPA was the most densely covered area in MDA-B. However during the survey there were a lot of sources of external noise drastically affecting the quality of the acquired data. In addition the asphalt there was thicker, and the attenuation higher. This can be easily seen in the seismograms, a fact that increased the level of uncertainty of the picked traveltimes. Paradoxically, there were places where the quality of the data was very good (e.g. Lines 10, 14, 18).

From Lines 8, 9, and 10 (Fig. 8.10-8.12) we can only see a minor disturbance of the Bandelier tuff that was probably done during the reconstruction and paving of the site in 1966. At these lines the tuff consists of two layers, one with seismic velocity 2000 ft/s and 2500 ft/s the other, with the former become progressively thicker in addition to topographical changes toward the East. Velocities within these layers may also change suggesting a local-scale heterogeneity. Line 18 averages these changes, yielding velocities 2200 ft/s and 2800 ft/s correspondingly, a fact that apparently contradicts with Lines 8,9,10 where velocities are decreased. This pronounced reduction in the transverse lines may be an indication of a local anisotropy but more likely is due to unresolved interface dip. Lines 11, 13, 14, 15 and 15r (Fig. 8.13-8.17) consistently cross perpendicularly a structure(trench) with much lower average velocity of about 1200 to 1400 ft/s. It is worth noticing that at Lines 11,13 and 14 the first tuff layer seems to have lower velocities at the southern end. Such a differentiation cannot be easily seen at Lines 8, 9, 10, 16, 15, or 15r. For the traverse Lines 11,13,14,15, and 16 the calculated velocity for the second layer was consistently 2400 ft/s.

The concluding results for this part of the site are presented in the following tables with the corresponding models shown in Figures 8.10, 8.11, 8.12, 8.13, 8.14, 8.15, 8.16,

8.17, 8.18, and 8.19 .

Table 8.1: Velocity model for line 8

Layer	Mean thickness (ft)	Velocity (ft/s)
1st	1.50	500
2nd	3.0	2000
3rd	–	2500

Table 8.2: Velocity model for seismic line 9.

Layer	Mean thickness (ft)	Velocity (ft/s)
1st	1.0	500
2nd	2.5	2000
3rd	–	2500

Table 8.3: Velocity model for line 10

Layer	Mean thickness (ft)	Velocity (ft/s)
1st	< 1.00	500
2nd	$7.0 - 8.0$	2000
3rd	–	2500

Table 8.4: Velocity model for line 11

Layer	Mean thickness (ft)	Velocity (ft/s)
1st	< 1.0	500
trench	$10.0 - 12.0$	1350
3rd	$8.0 - 15.0$	$1400 - 2000$
4th	–	2400

Table 8.5: Velocity model for line 13

Layer	Mean thickness (ft)	Velocity (ft/s)
1st	$1.0 - 2.0$	500
trench	$9.0 - 12.0$	1300
3rd	$5.0 - 13.0$	$1400 - 2200$
4th	–	2400

Table 8.6: Velocity model for line 14

Layer	Mean thickness (ft)	Velocity (ft/s)
1st	< 1.0	500
trench	$10.0 - 12.0$	1200
3rd	$5.0 - 14.0$	$1600 - 1900$
4th	–	2400

Table 8.7: Velocity model for line 15

Layer	Mean thickness (ft)	Velocity (ft/s)
1st	< 1.0	500
trench	$12.0 - 15.0$	1400
3rd	$7.0 - 15.0$	2000
4th	–	2400

Table 8.8: Velocity model for line 16

Layer	Mean thickness (ft)	Velocity (ft/s)
1st	$0.5 - 1.5$	500
trench	$12.0 - 15.0$	1300
3rd	$9.0 - 17.0$	2000
4th	–	2400

Table 8.9: Velocity model for line 18

Layer	Mean thickness (ft)	Velocity (ft/s)
1st	$0.5 - 1.5$	500
2nd	$4.0 - 8.0$	2200
3rd	–	2800

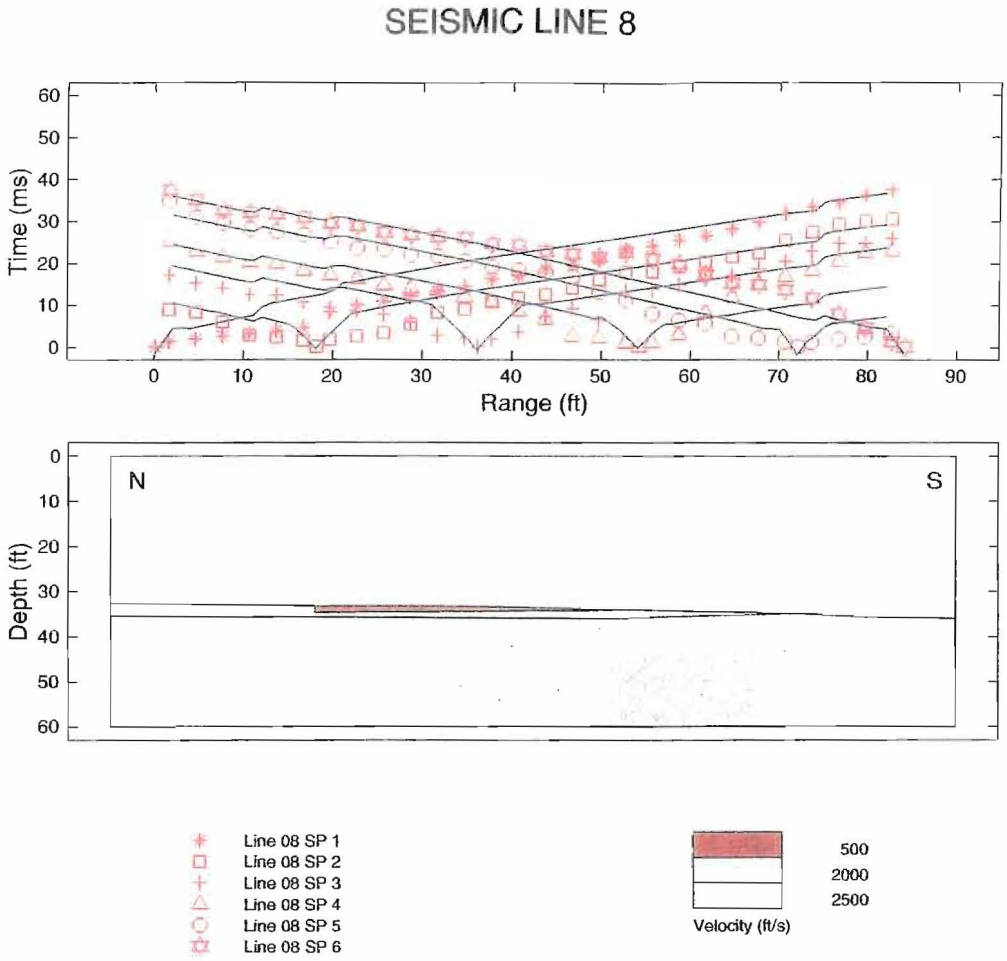

Figure 8.10: Travel times (red symbol observed, blue line computed), and corresponding model for line 8.

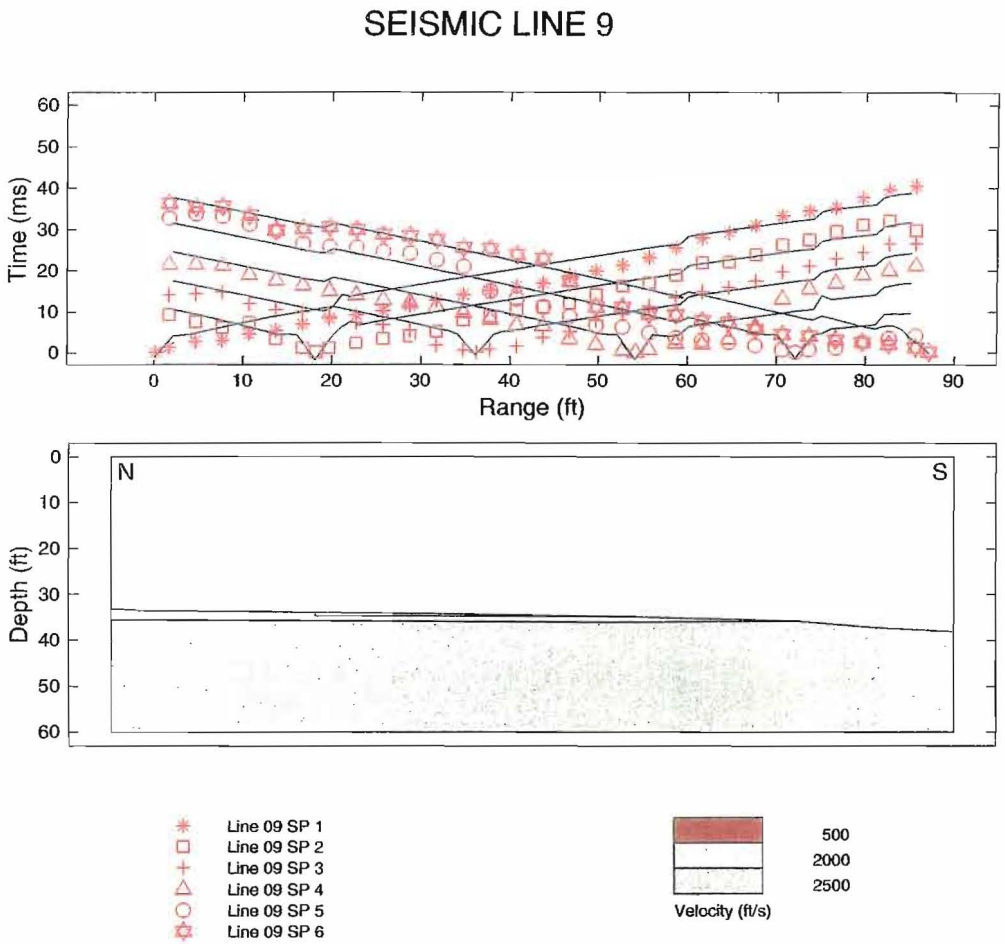

Figure 8.11: Travel times (red symbol observed, blue line computed), and corresponding model for line 9.

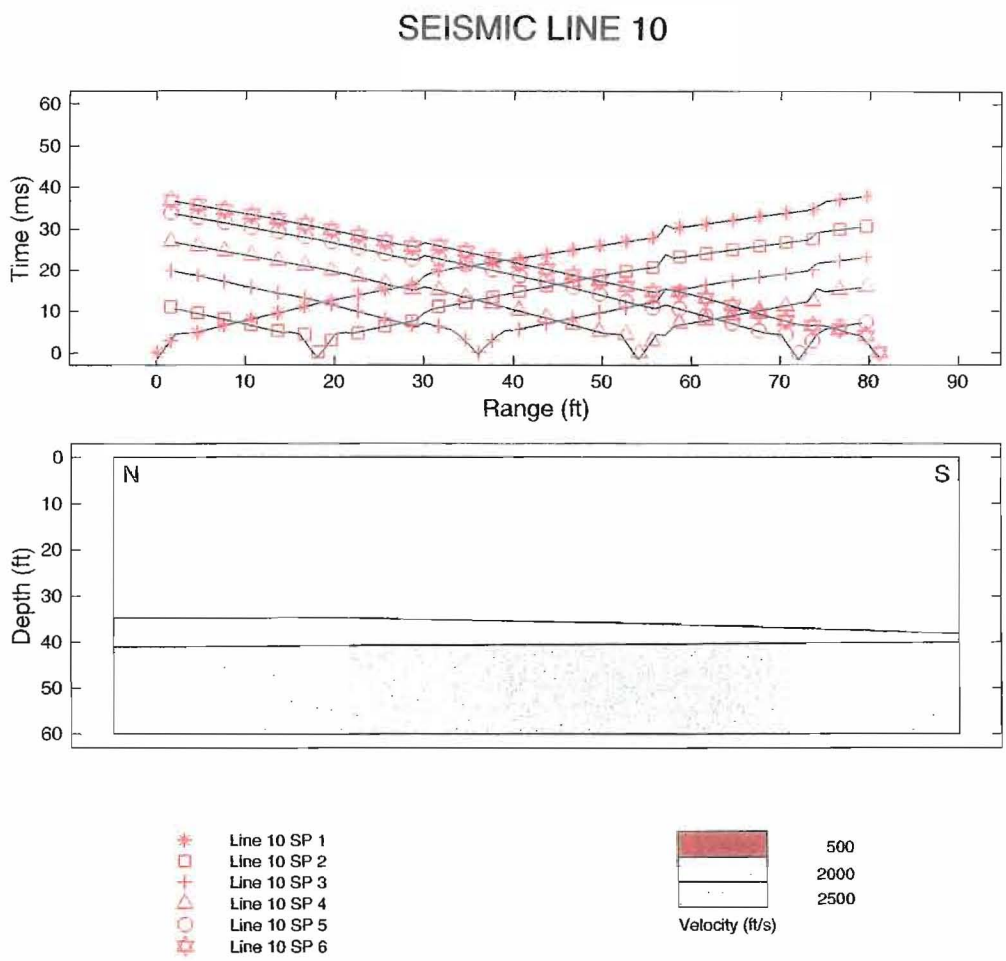

Figure 8.12: Travel times (red symbol observed, blue line computed), and corresponding model for line 10.

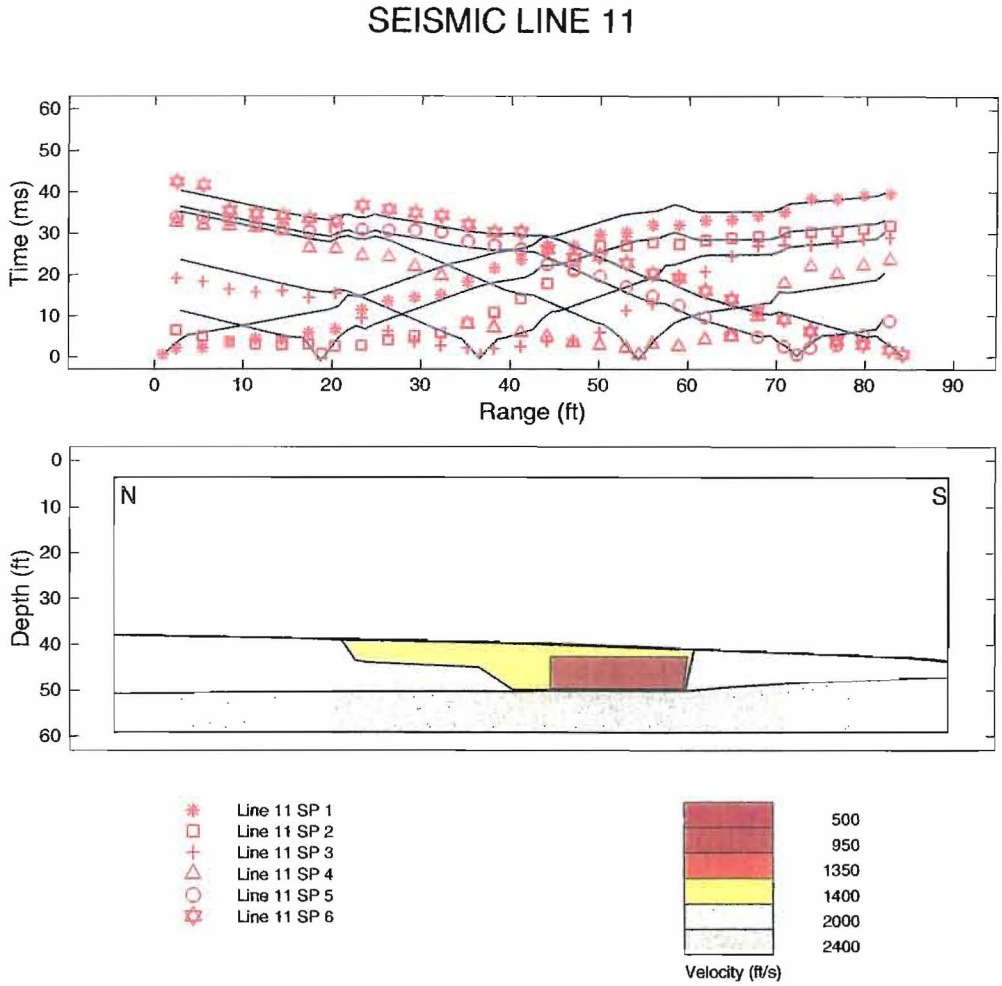

Figure 8.13: Travel times (red symbol observed, blue line computed), and corresponding model for line 11.

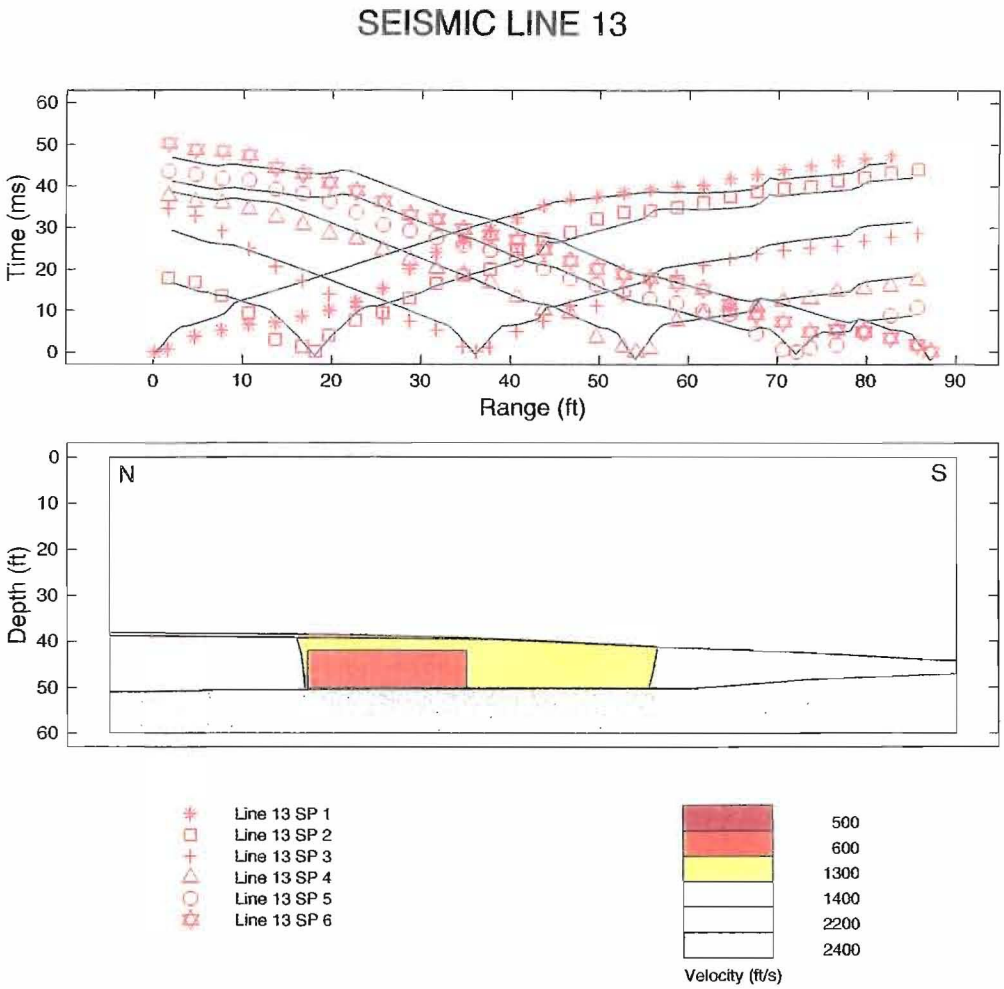

Figure 8.14: Travel times (red symbol observed, blue line computed), and corresponding model for line 13.

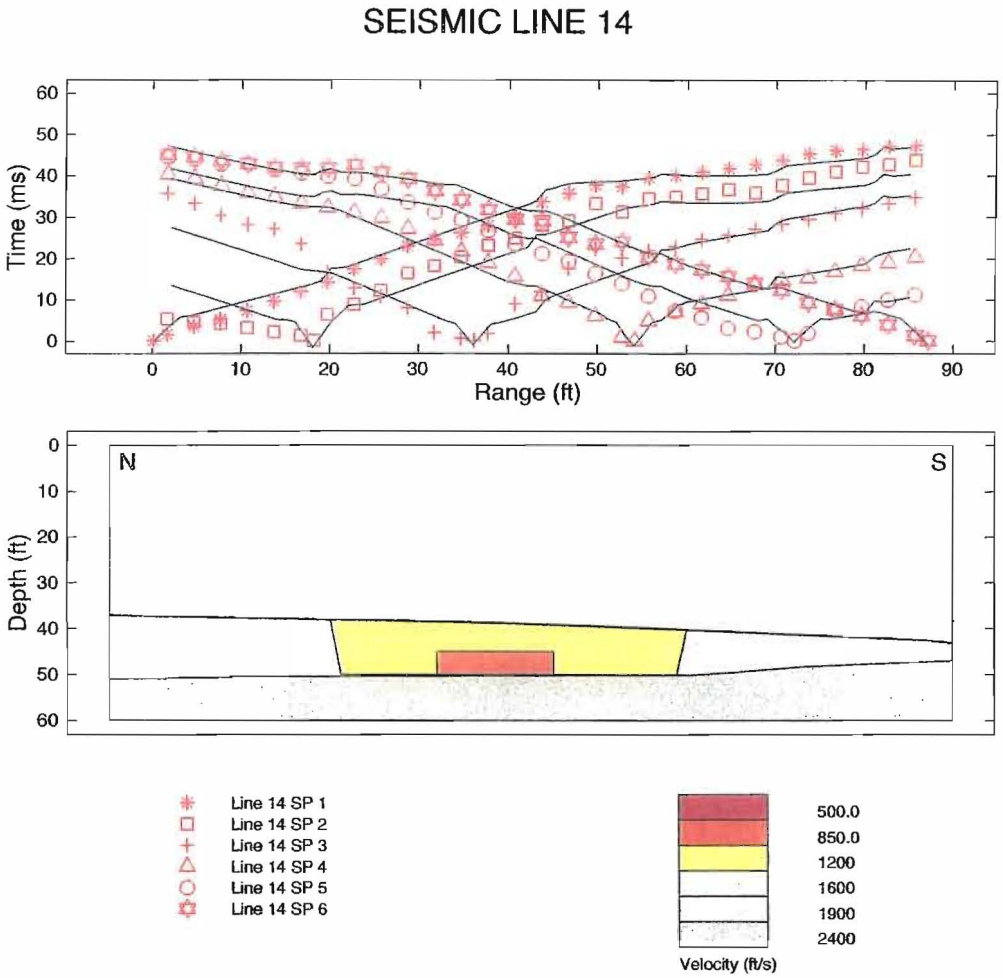

Figure 8.15: Travel times (red symbol observed, blue line computed), and corresponding model for line 14.

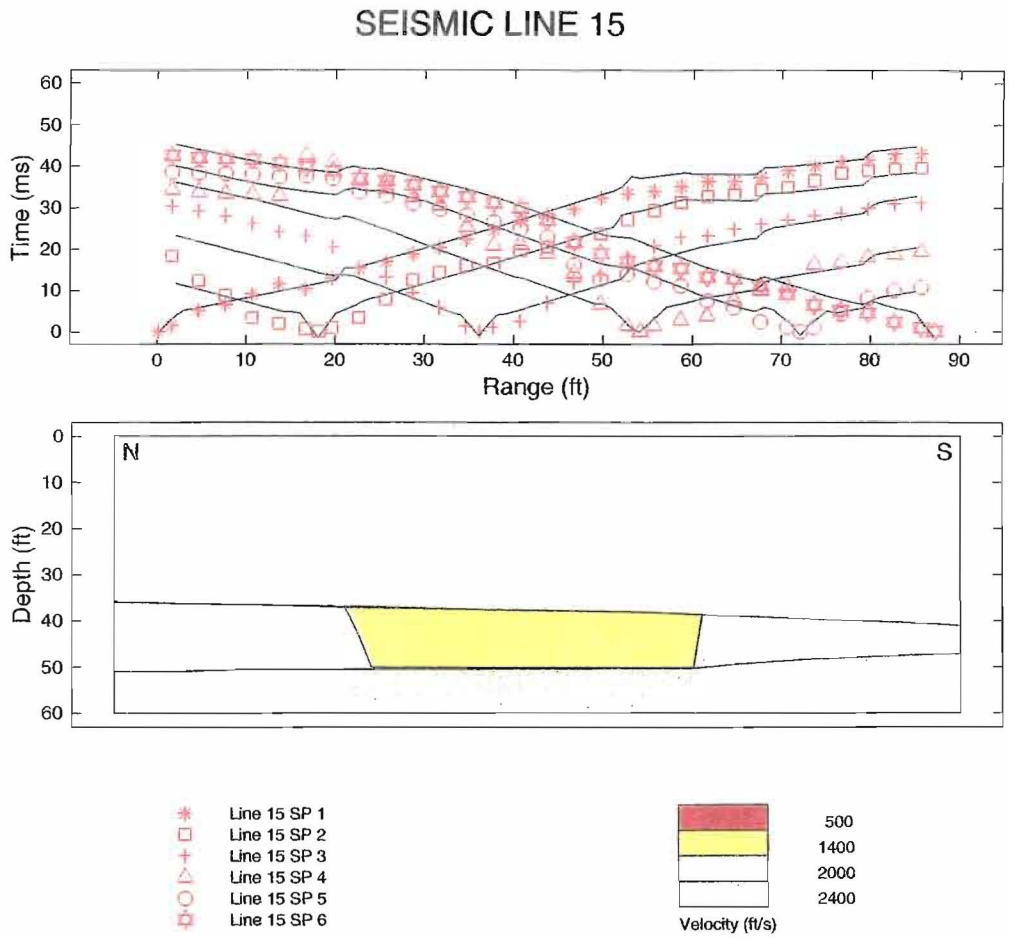

Figure 8.16: Travel times (red symbol observed, blue line computed), and corresponding model for line 15.

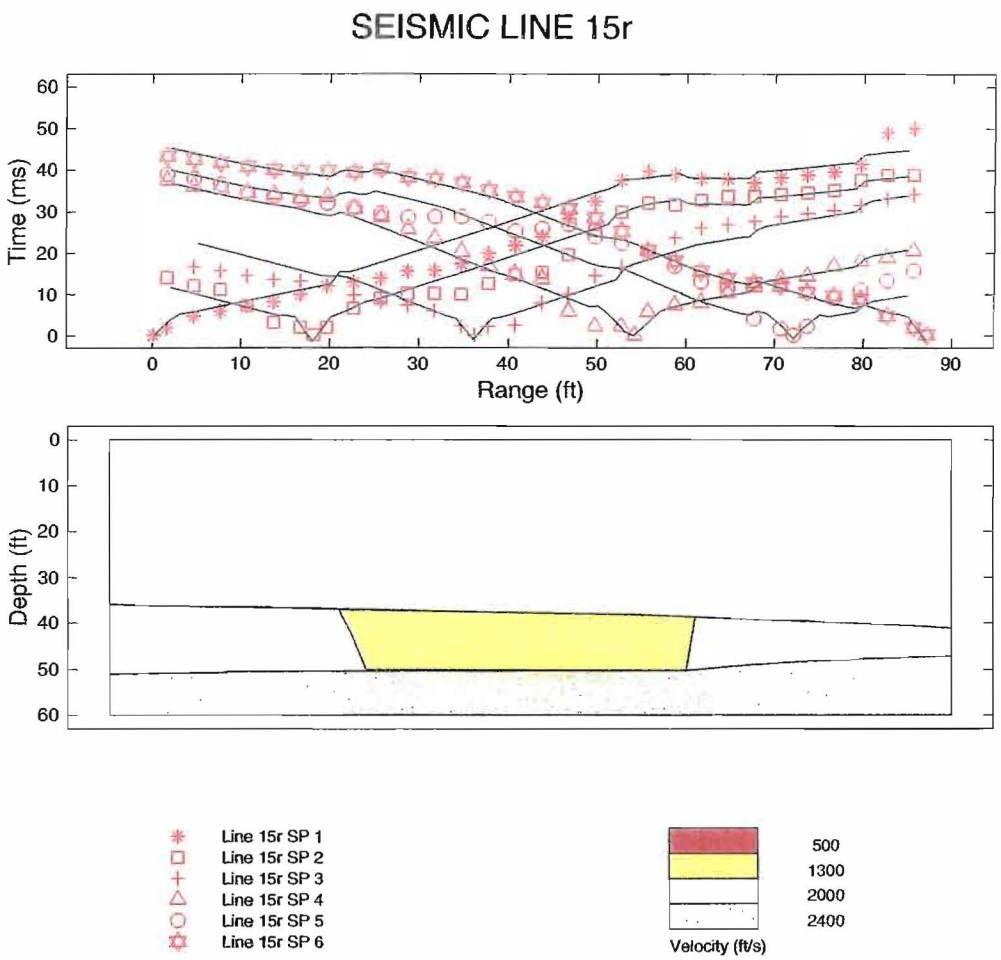

Figure 8.17: Travel times (red symbol observed, blue line computed), and corresponding model for line 15r.

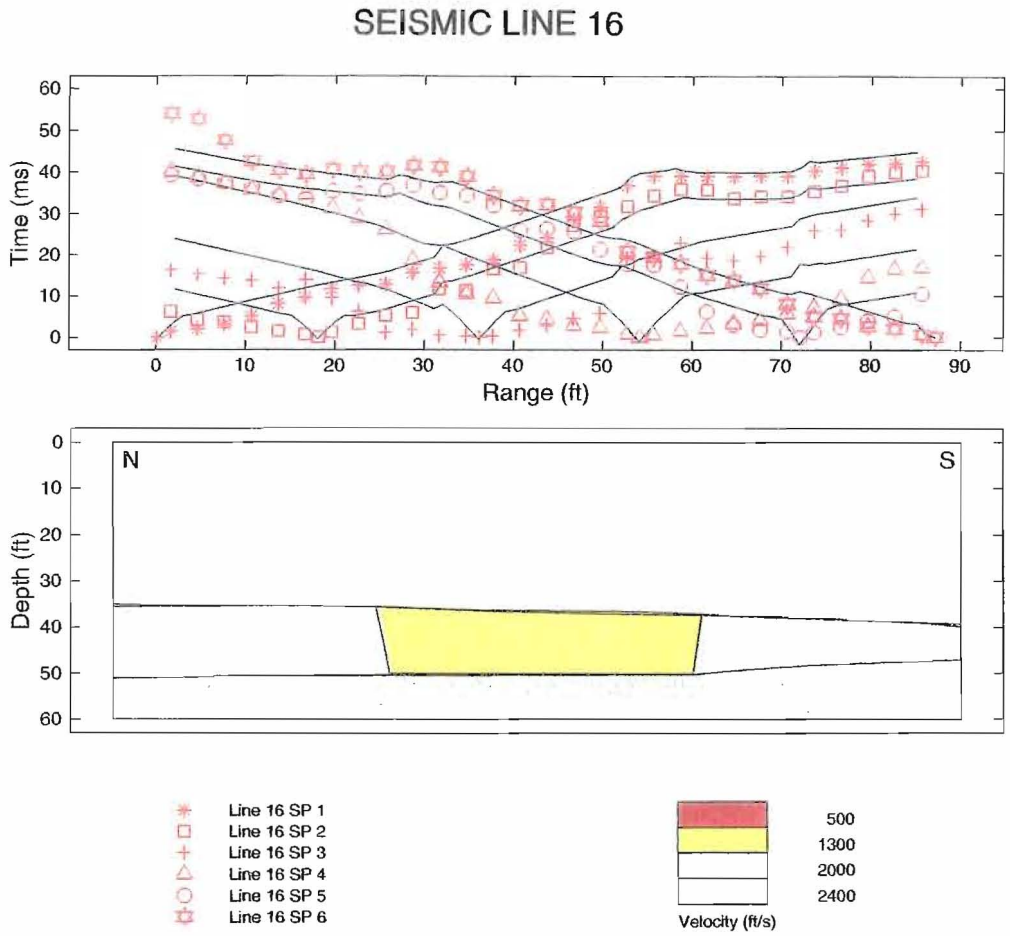

Figure 8.18: Travel times (red symbol observed, blue line computed), and corresponding model for line 16.

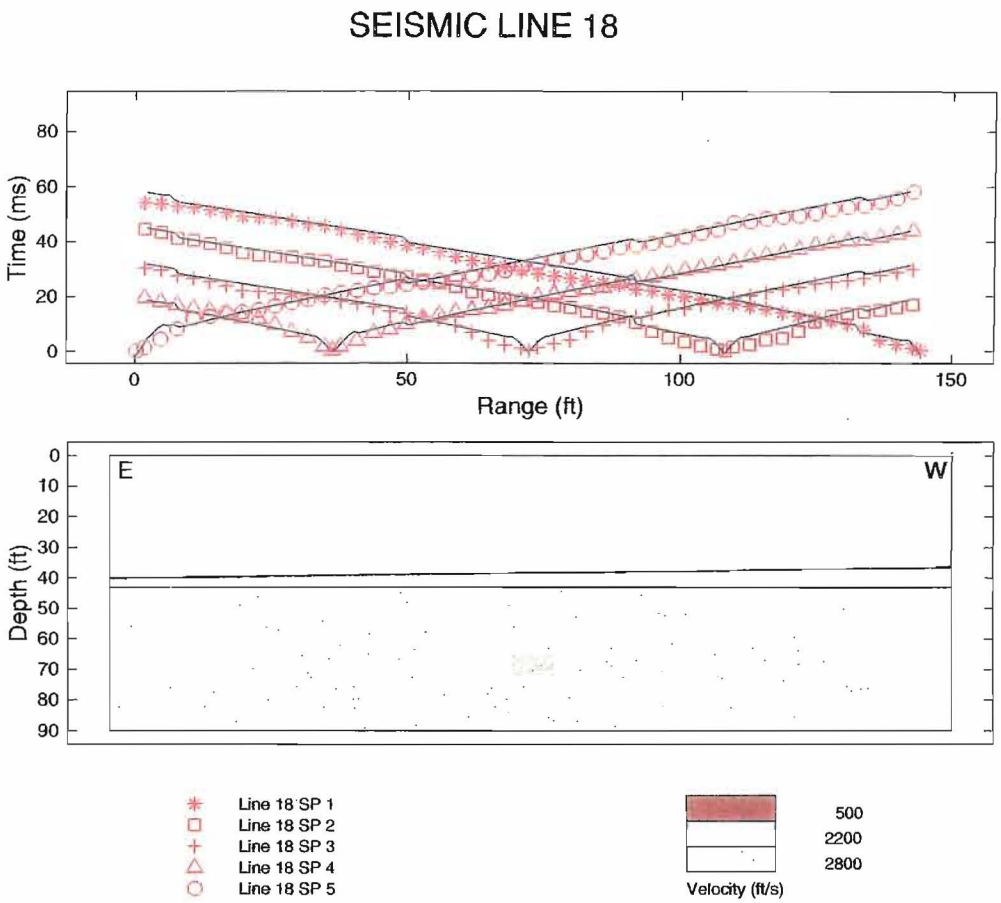

Figure 8.19: Travel times (red symbol observed, blue line computed), and corresponding model for line 18.

8.2.3 Western Paved Area

The data acquired in WPA was among the best compared to the other areas. This happened because the negative factors affecting the quality of the survey seemed to be minimized in WPA as the asphalt layer here was very thin and fragile, the noise during the data acquisition small and the attenuation of the medium lower. For instance Line 7 provided almost exceptional data (Fig 8.21) for this kind of survey. At this line the calculated velocity for the tuff was 2700 ft/s. The same value was also obtained from Line 28, which is located about 75 ft east of Line 7. The maximum depth of the mapped trench as was determined in Line 7 and Line 28 was 10.5 ft and 8.5 ft respectively, with the topography almost identical in both lines. Line 27 that ties Lines 7 and 28 was in agreement at the crossing points. Line 27 also determined the gently dipping, eastern boundary of the trench. The velocity of the tuff disclosing by Line 27 was 2800 ft/s, a hundred ft/s more than those in Lines 7 and 28.

Located in the middle of WPA, Line 26 disclosed a simple prismatic model with boundaries almost at right angles, and seismic velocity 1300 ft/s. However as opposed to previous location, the tuff here appears to be layered. The first layer with thickness 3.8 ft can be split into two parts; the northern part with velocity 2400 ft/s and the southern one with the lower velocity of 2000 ft/s because of the mixing with construction material during the leveling of the site. The capping layer at this site (with the very low velocity of 550 ft/s) is also thicker than at the north side. Underneath it follows a slightly south-dipping tuff-layer with velocity 2700 ft/s.

Line 25, 400 ft West of Line 26, suggested a similar model but with an extra layer. This layer that immediately follows the first one, appears to have even higher velocity, about 3000 ft/s. At this profile also, the first layer has thickness 4.5 ft,

and the velocities are 2500 ft/s for the northern part and 2700 ft/s for the southern one, while the second is 18 ft thick and finally the last one has an estimated velocity of about 3200 ft/s. The three layers can be taken as a differentiation of the same Unit-3 of the Tshirege member.

Line 24 was shot perpendicular and from the middle of Line 25, reaching the west end of WPA. The constructed model suggests three layers with velocities 2300, 2900, and 3200 ft/s and mean thickness 6 and 15 ft correspondingly. The trench begins in the middle of the line and has an average depth of about 12 ft with velocity 1000 ft/s. Tables 8.10, 8.11, 8.12, 8.13, 8.14, and 8.15 summarize the refraction results for WPA with models shown in Figures 8.20, 8.21, 8.22, 8.23, 8.24, and 8.25.

Table 8.10: Velocity model for line 28

Layer	Mean thickness (ft)	Velocity (ft/s)
1st	1.0	550
trench	7.5	1200
3rd	–	2700

Table 8.11: Velocity model for line 7

Layer	Mean thickness (ft)	Velocity (ft/s)
1st	0.5	550
trench	8.0	1200
3rd	–	2700

Table 8.12: Velocity model for line 27

Layer	Mean thickness (ft)	Velocity (ft/s)
1st	0.7	450
trench	5.0	1200
3rd	–	2800

Table 8.13: Velocity model for line 26

Layer	Mean thickness (ft)	Velocity (ft/s)
1st	2.0	550
trench	15.0	1200
3rd	5.0	2000
4th	6.0	2400
5th	–	2700

Table 8.14: Velocity model for line 25

Layer	Mean thickness (ft)	Velocity (ft/s)
1st	0.5	550
trench	15.0	1200
3rd	6.0	2500
4th	5.0	2700
5th	10	2900
6th	–	3200

Table 8.15: Velocity model for line 24

Layer	Mean thickness (ft)	Velocity (ft/s)
1st	1.5	600
trench	18.0	1000
3rd	7.0	2300
4th	10.0	2900
5th	–	3200

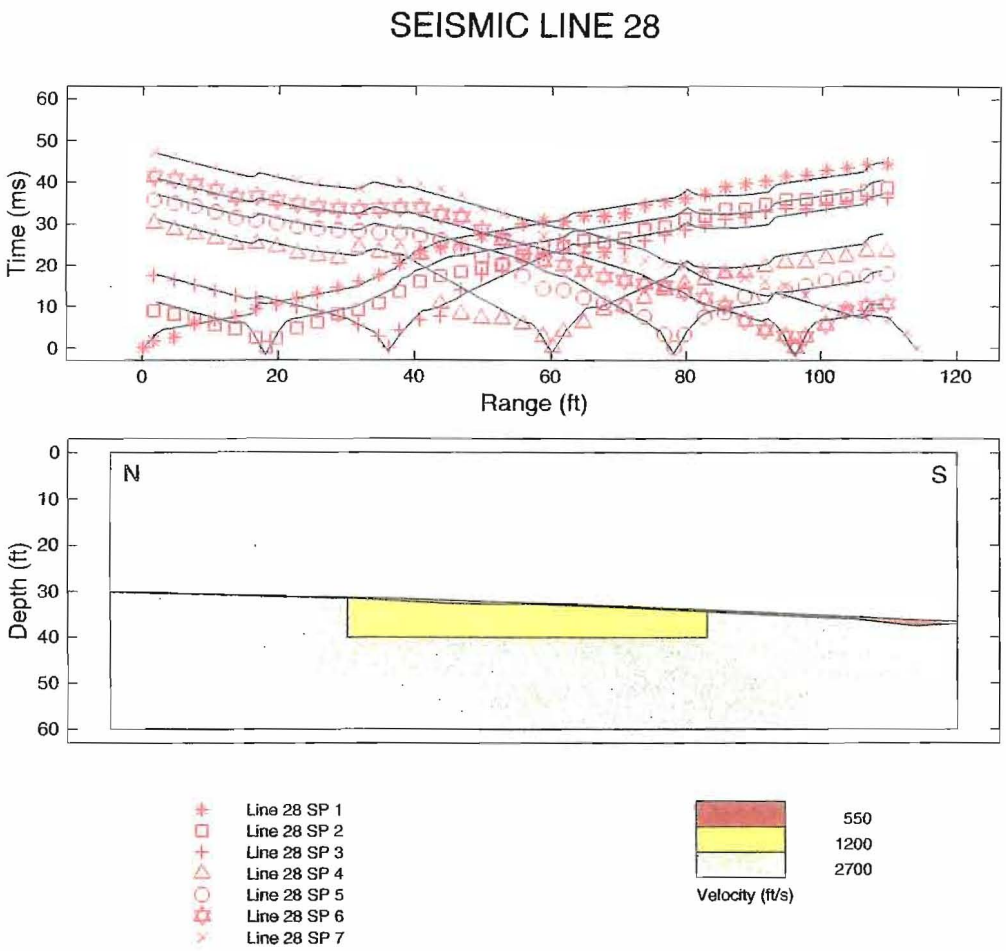

Figure 8.20: Travel times (red symbol observed, blue line computed), and corresponding model for line 28.

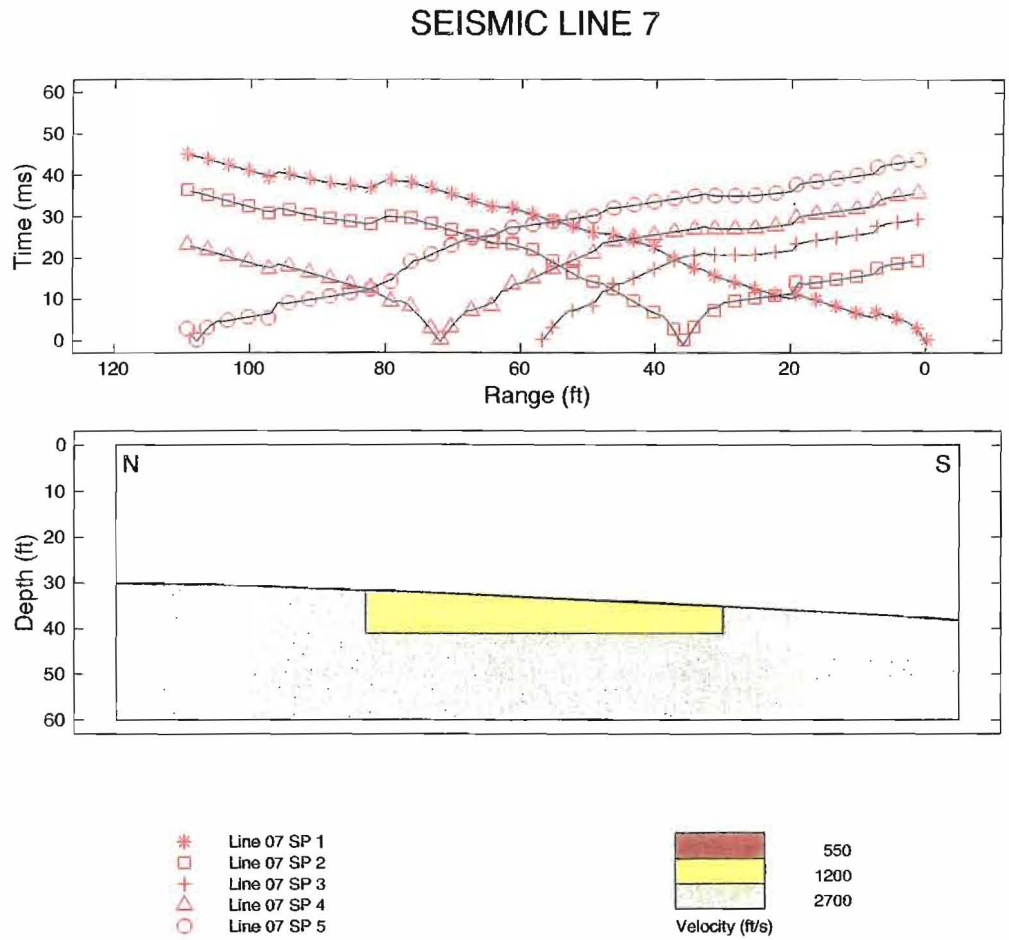

Figure 8.21: Travel times (red symbol observed, blue line computed), and corresponding model for line 7.

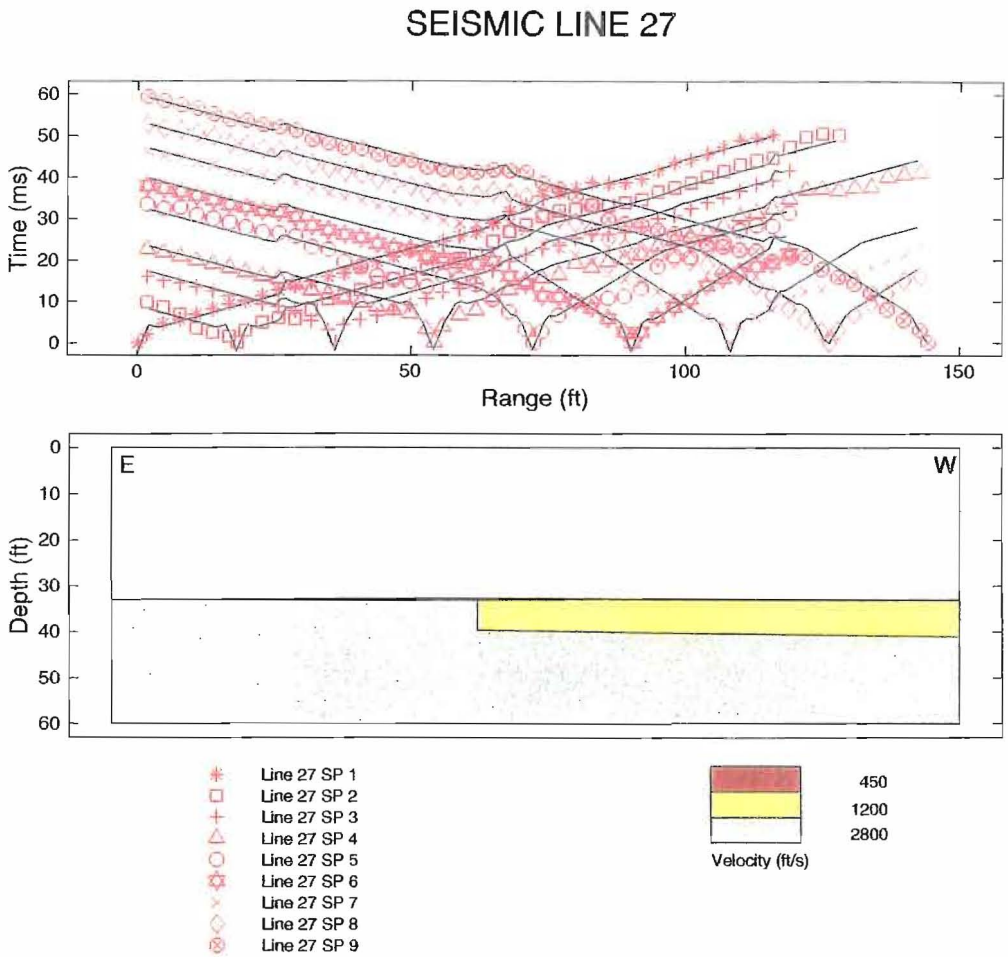

Figure 8.22: Travel times (red symbol observed, blue line computed), and corresponding model for line 27.

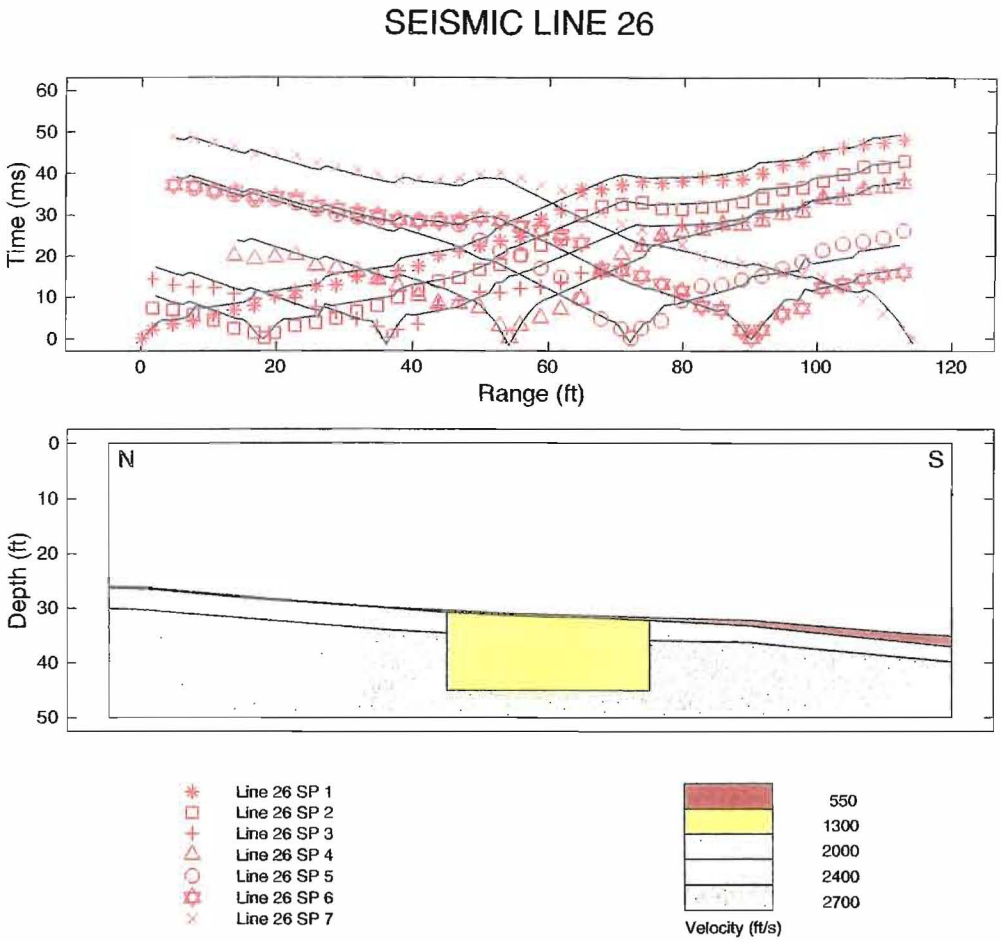

Figure 8.23: Travel times (red symbol observed, blue line computed), and corresponding model for line 26.

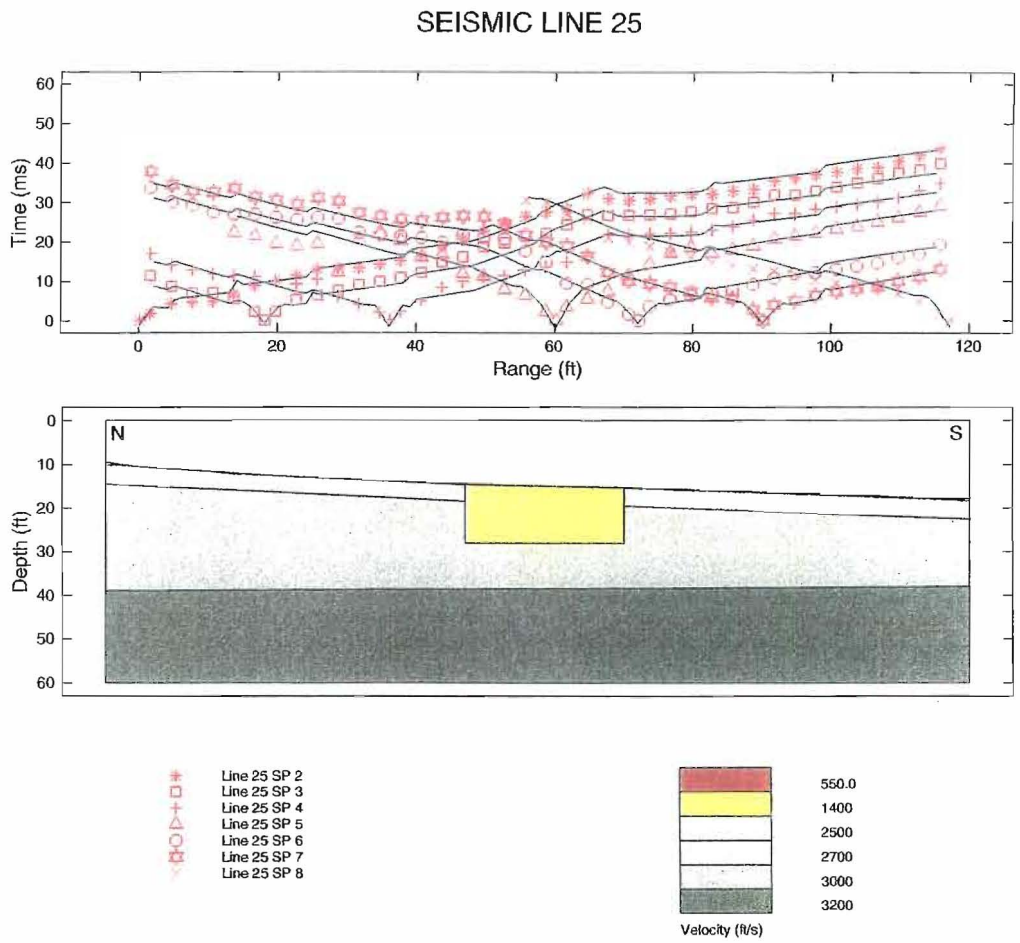

Figure 8.24: Travel times (red symbol observed, blue line computed), and corresponding model for line 25.

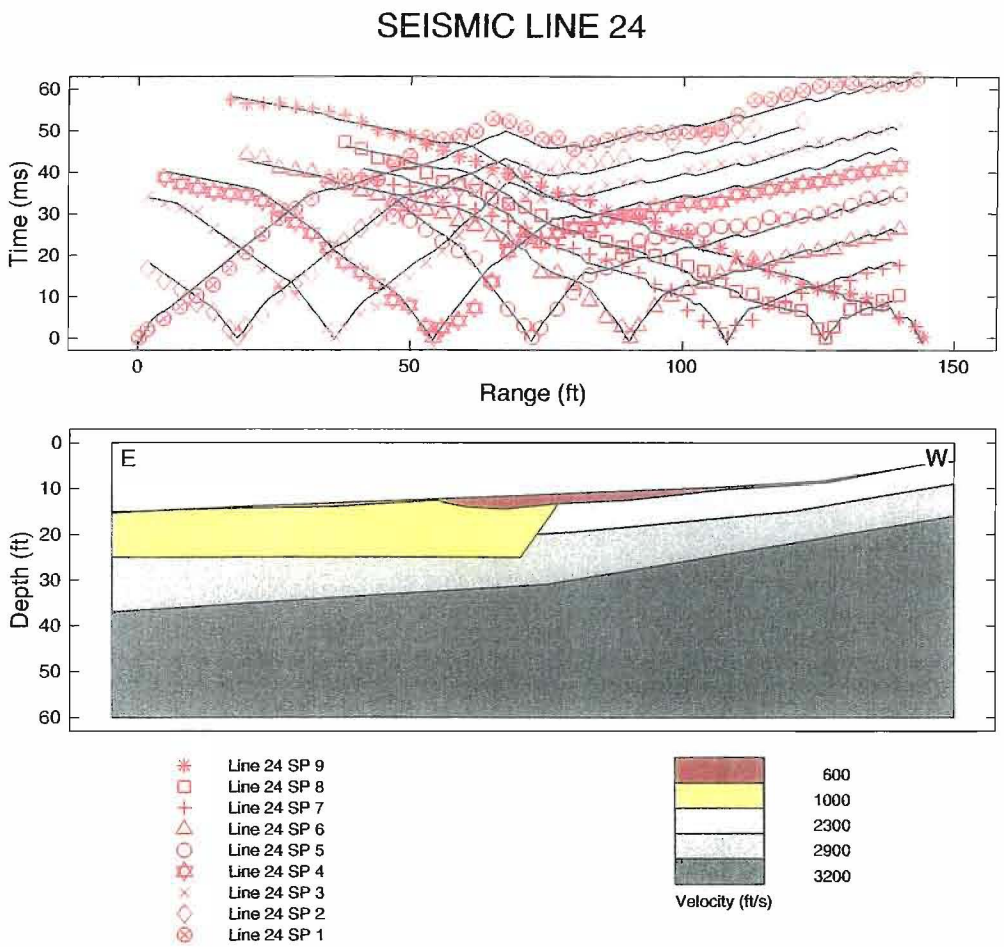

Figure 8.25: Travel times (red symbol observed, blue line computed), and corresponding model for line 24.

8.2.4 Western Unpaved Area

Finally at WUA two profiles, Line 23 and Line 22, were sufficient to paint a representative picture. The final models suggest a simple two-layer structure and a fill or soil layer. There is no trench presence at this location. At Line 22 close to the east end (90 ft from the first shot point) the weathering layer was noticeably thicker (Fig 8.27). In contrast seismic line 23 (Fig 8.27) shows no indication of any such thickness increase. The Bandelier tuff appears as a two-layer unit with velocities 2000 and 3200 ft/s, while the thickness of the first layer has an average value of about 10 ft (tables 8.16 and 8.17).

Table 8.16: Velocity model for line 23

Layer	Mean thickness (ft)	Velocity (ft/s)
1st	1.0 – 2.0	450
2nd	5.0 – 8.0	2000
3rd	–	3200

Table 8.17: Velocity model for line 22

Layer	Mean thickness (ft)	Velocity (ft/s)
1st	0.5 – 2.0	450
2nd	3.0 – 20.0	2000
3rd	–	3200

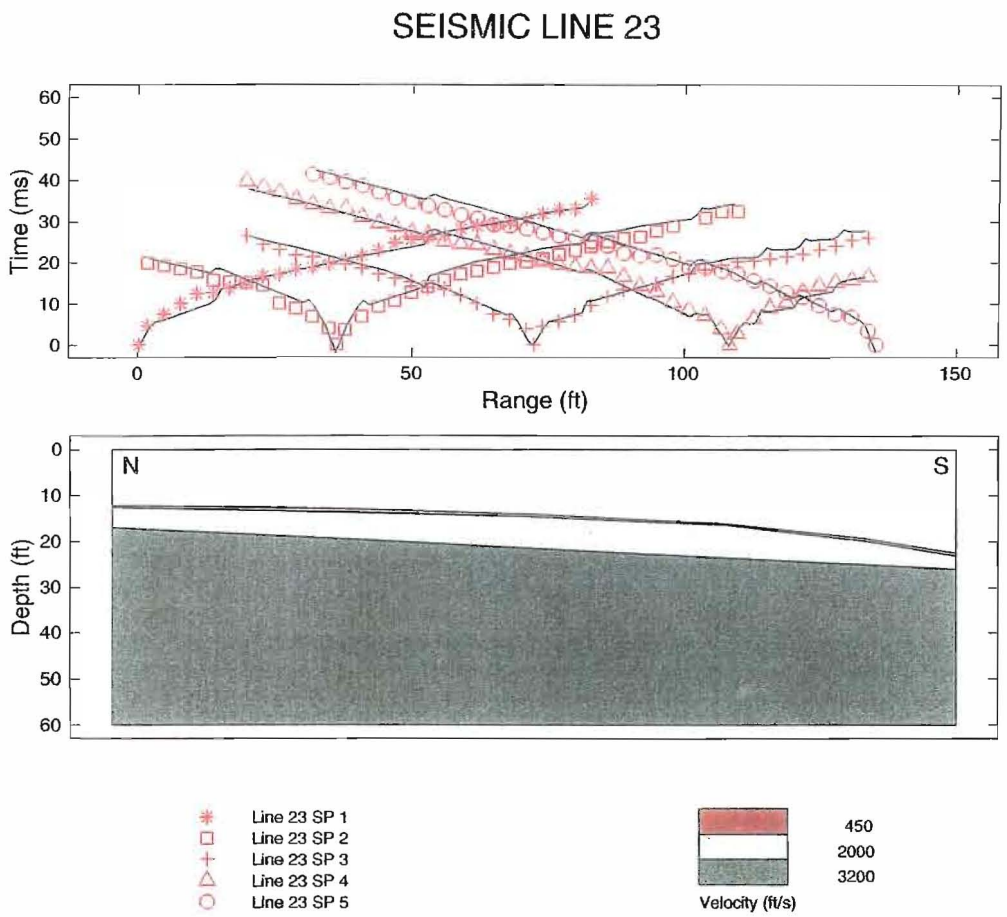

Figure 8.26: Travel times (red symbol observed, blue line computed), and corresponding model for line 23.

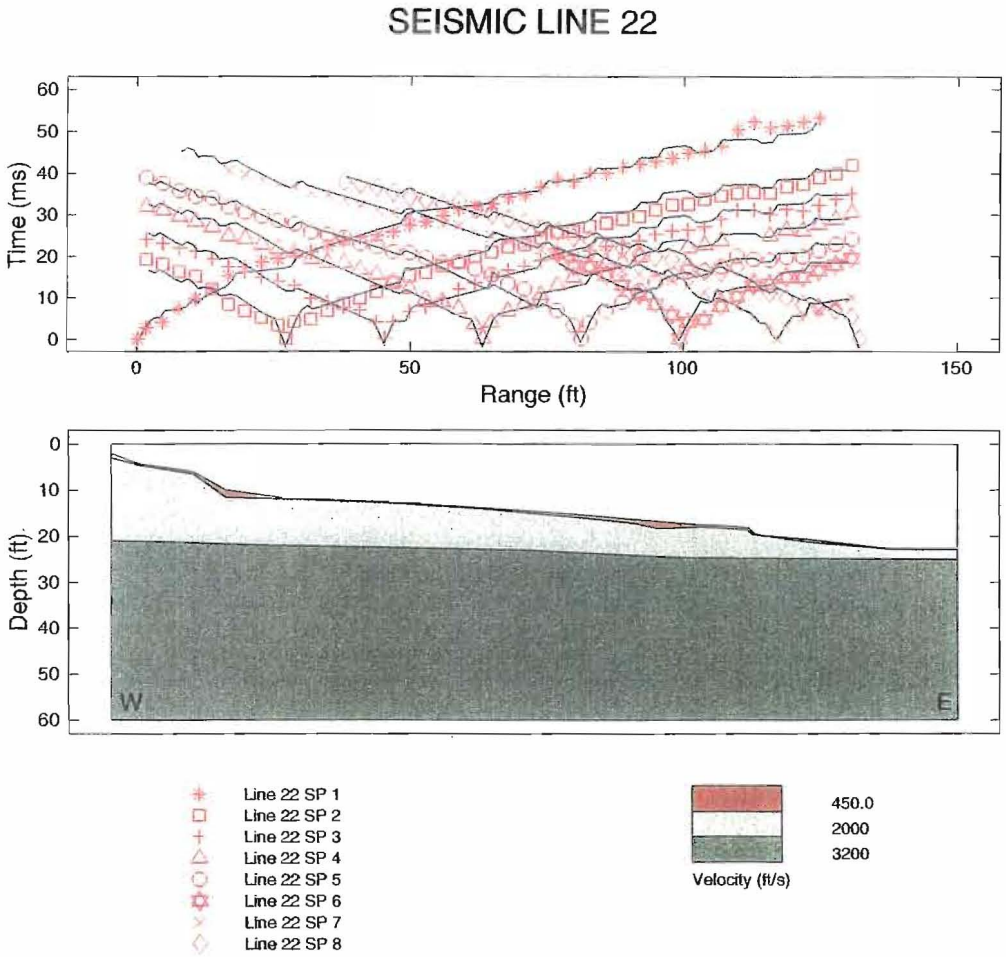

Figure 8.27: Travel times (red symbol observed, blue line computed), and corresponding model for line 22.

Chapter 9

Conclusions and Recommendations

The final models and conclusions that are drawn from the whole survey should take into consideration both seismic and magnetic interpretations. The combined results of magnetic and seismic surveys give a very detailed view of trench boundaries and contents. The approach we use to do this follows the familiar scheme; each MDA-B subdivision is interpreted individually and possible connections between them are made based on the models.

EUA

Starting from the Eastern Unpaved Area, both seismic and magnetic models suggest the existence of one big, elongated trench, which is covered by two layers. The layers correspond to the two experimental caps, and on top of the cap overlays a very thin low-velocity layer. The thickness of the experimental caps as they are shown in the seismic models for Lines 5, 6, 3 and 2 varies along the area. This is in agreement with the three profiles as there are defined by Nyhan and Barnes (1989). The hypothesis of one big elongated trench is supported by the magnetic data (Fig 6.15) and partially from the seismic Line 4. From the magnetic data we can also clearly see the eastern termination of the trench but at the western end there is

no such an evidence. The trench seems to continue toward the paved eastern area (EPA) that is a natural continuation to the west. Unfortunately Line 20 could not be modeled due the noisy character of the seismograms. Thus the east end of the trench is solely determined by the magnetic data with an estimated accuracy of about $\pm 15 ft$. As it was explained in chapter 8 the modeled magnetic anomaly E is due to an accumulation of prismatic bodies at shallow depth. Indeed, it was common practice for LANL to place waste material in wood boxes. However, in MDA-B there was no attempt to keep the various material separated. According to Rogers report (Rogers, 1977) and an internal LANL memo, most of the material in MDA-B consisted of rags, paper, glassware, rubber gloves, and metal apparatus placed in wood boxes or cardboard boxes sealed with masking tape or even wrapped with paper. Also ,from a later photo in pit 8, area G (Fig. 9.2)we can suspect a possible assemblage for these boxes. Magnetic modeling of anomaly E at EUA (Fig. 8.7, 8.8) conforms highly with this model.

EPA

In the Eastern Paved Area the magnetic data (Fig. 6.5 and 6.7) support the previous hypothesis of the continuation of the trench. The maps also suggest that the rectangular-shaped anomaly that is also parallel to the fence stops at easting 370 ft. This complies with the existing old air-photo taken during the construction time and showing this trench open. From both seismic and magnetic models we can see that at the north-west end the trench forms a ramp lowering toward east, that probably served as the access entrance. The magnetic sources are scattered in the intermediate available space. Anomaly A (fig 6.6) seems to be located at the southern edge of the trench while anomaly D may continue beyond EPA toward EUA. According to the

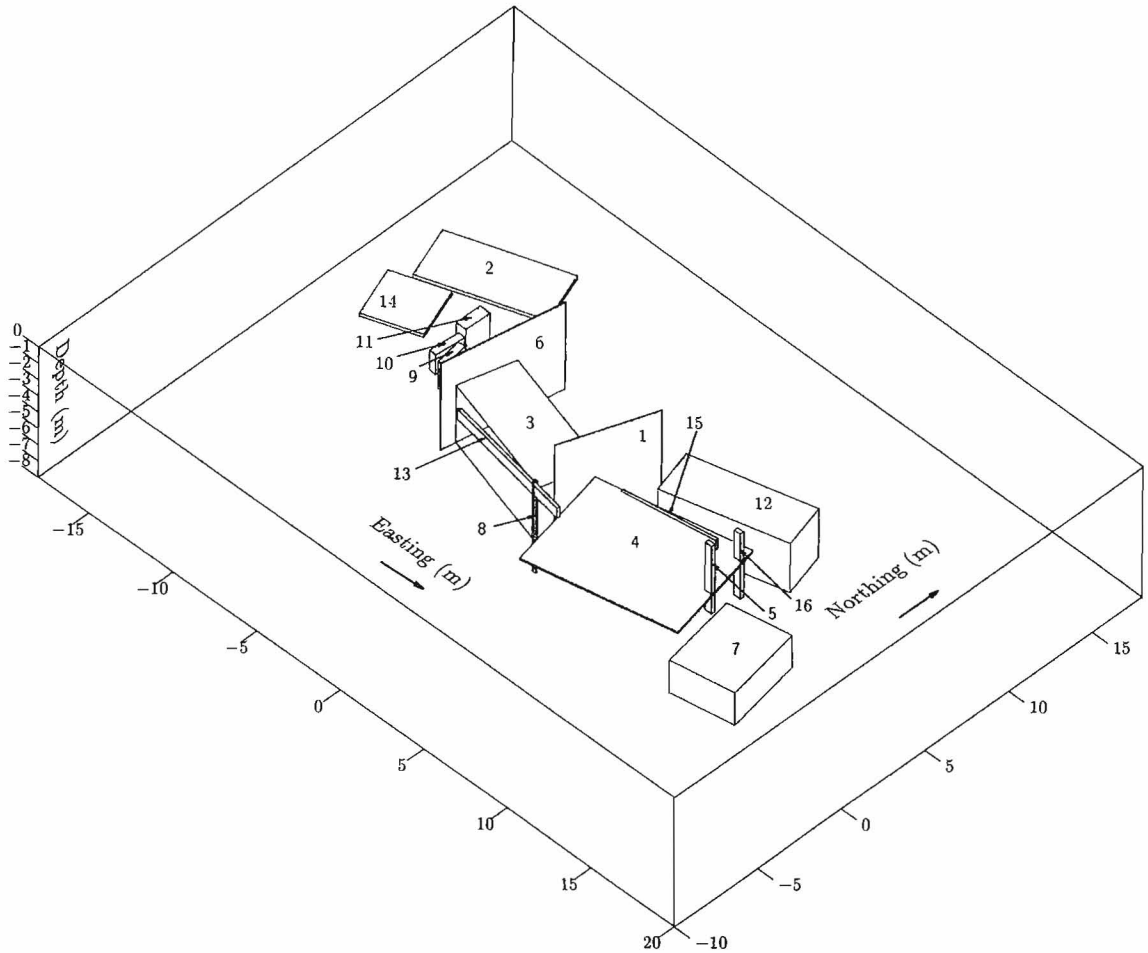

Figure 9.1: Magnetic model for magnetic anomaly E. (See also Fig 6.13)

seismic models the formed trench is parallel to the fences with an average width of about $40ft$, and average depth $12ft$ (tables 8.4,8.5,8.6,8.7,8.8). The final model for EPA can be seen in figure 9.3

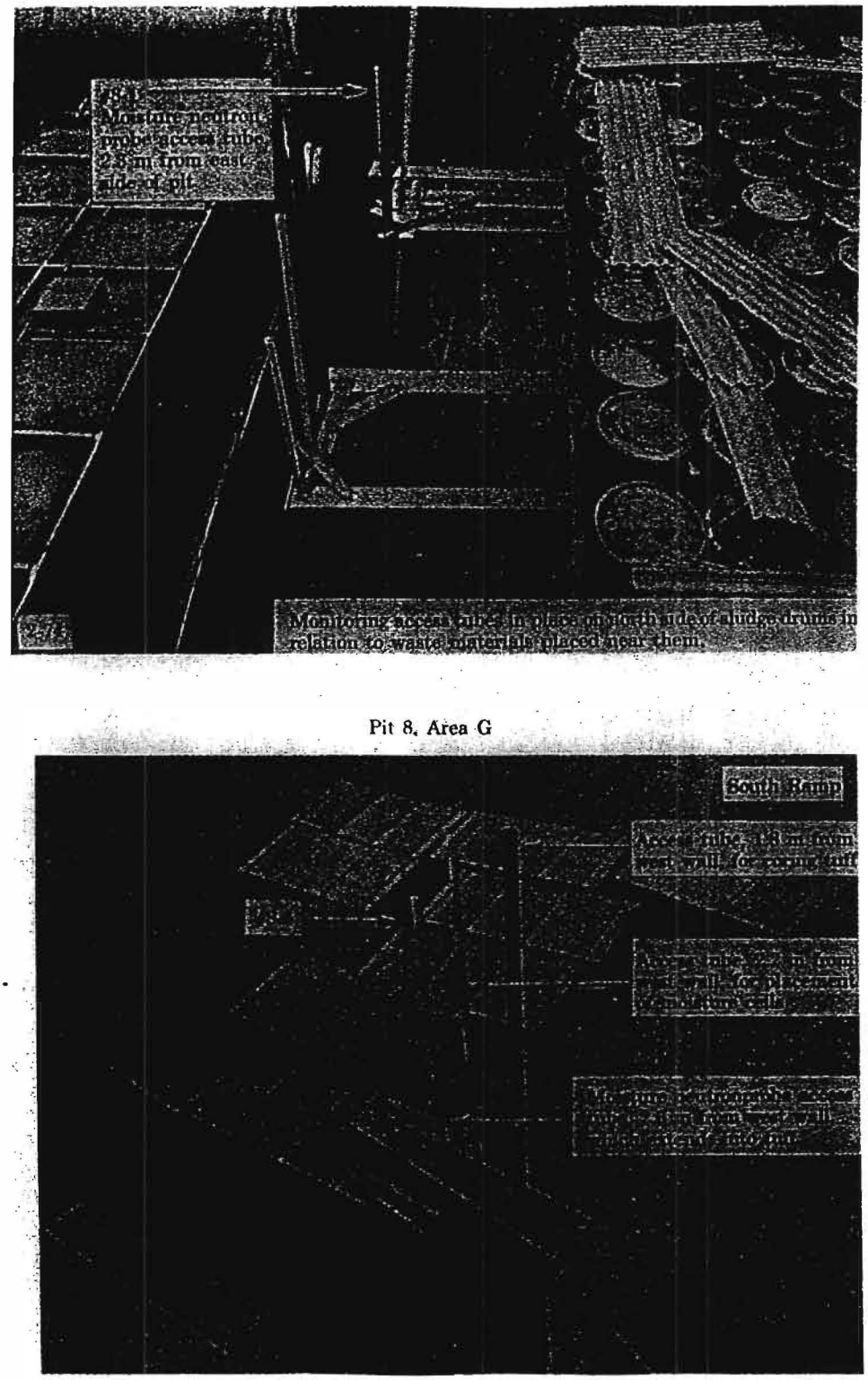

Figure 9.2: Wood boxes, drums and access tubes for monitoring in Pit 8, area G.

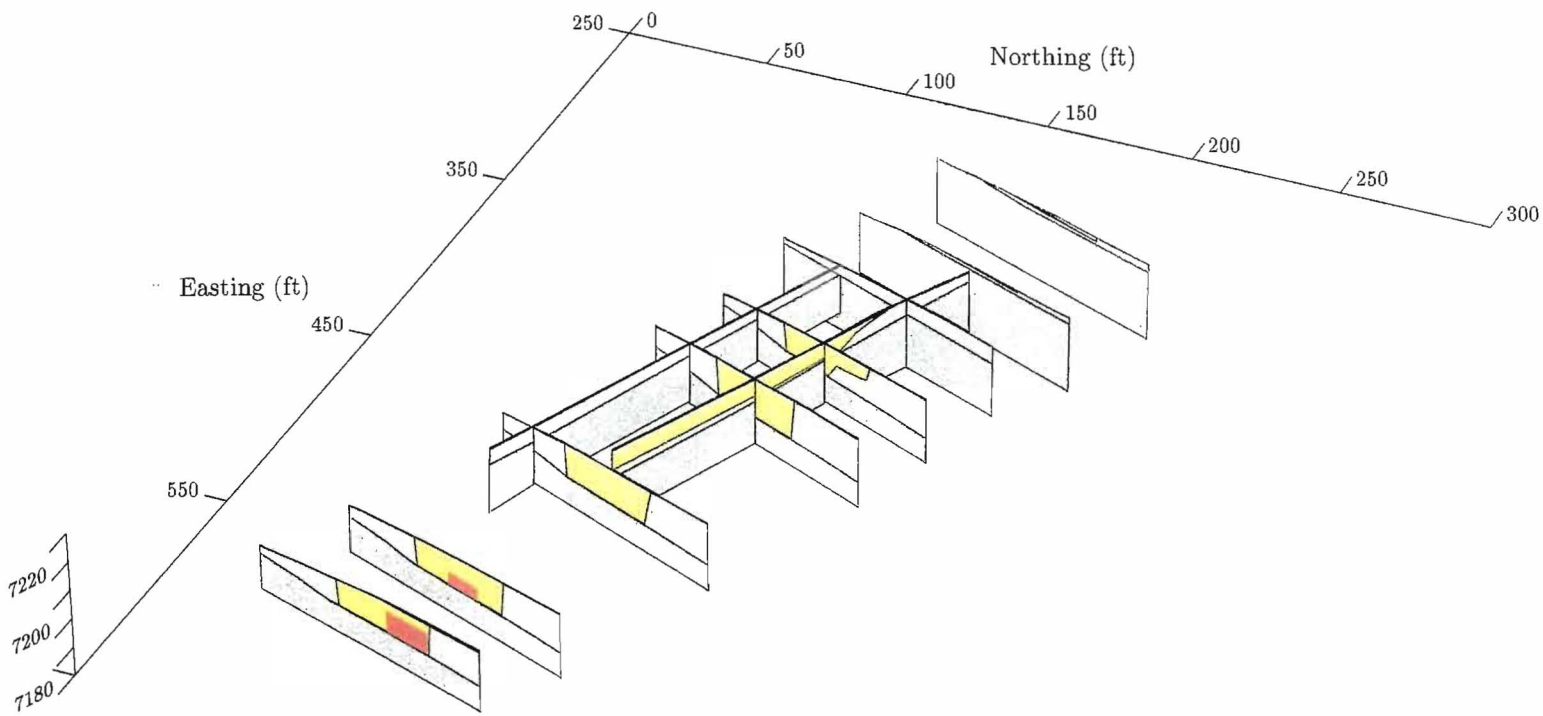

Figure 9.3: Interpreted seismic model for EPA.

WPA

Being the largest area of the site, WPA seems to host three separated trenches. Starting from east to west the first pit appears right after the "bending" point of MDA-B close to the middle of the site. The eastern end probably served as an access entrance for dumping the wastes. Also at the same end, the modeled magnetic anomaly 4 (Fig 9.4, 8.5, 8.6) suggests a distribution of shallow thin magnetic bodies somehow different than in anomaly E (Fig 9.1). The lack of deeper sources and the shape of the anomaly suggests that the later is mainly due to shallow, thin metallic plates (e.g. sheets that might had been used to deflect infiltrating water away from the wastes). The second trench, immediately next to the first one, starts after a

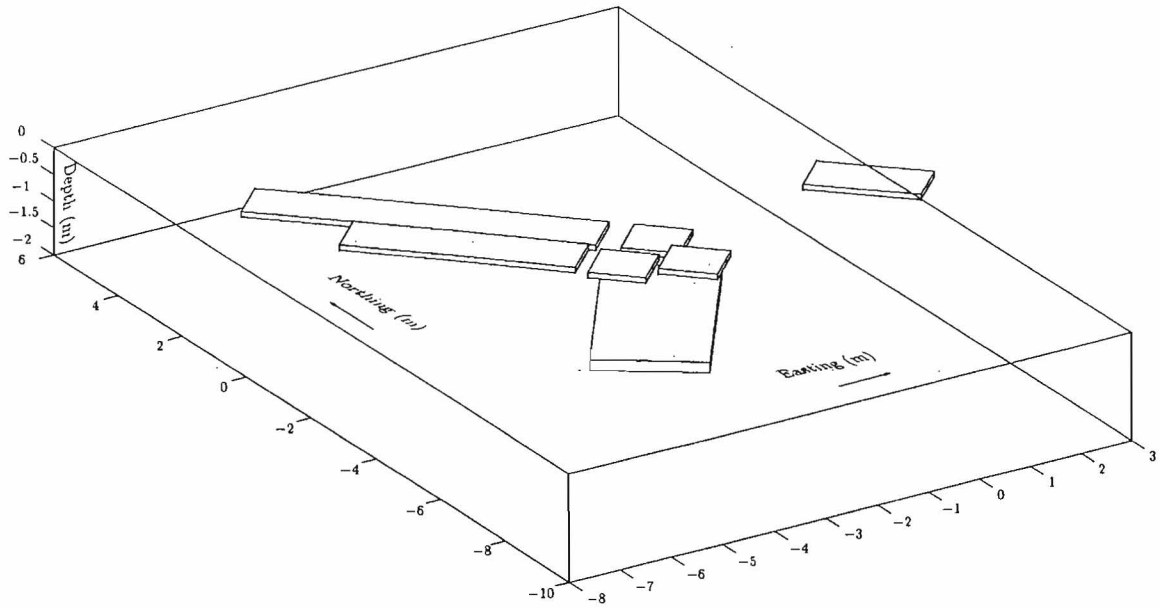

Figure 9.4: Magnetic model for magnetic anomaly 4.

distance of a few feet ($\sim 15ft$) and it appears to be deeper and narrower. With a development of about $300ft$ this is the least "mapped" portion of the site. The shape and extension of the second trench (Fig 6.7, 8.23) is based on the seismic Line 26

(depth, width) and the magnetic data (width, length). Figure 9.5 shows the models produced from the seismic survey only for these two trenches.

The third trench (Fig 9.6), aligned with the other two, extends up to the end of WPA and just enters the fenced portion of it. Its calculated length (from the magnetic data) is also $300ft$ and conforms with an old memo (Rogers, 1977) for MDA-B on July 5, 1945

"... suggest that a trench 15 ft wide and 300 ft long be bulldozed out as deep as possible before hard rock is encountered, starting just east of the now covered CM[R] disposal pits located SE of the coal storage yard, and running parallel to and about 40 or 50 ft north of the DP -power lines. ... it could be progressively filled and covered from the west end toward the east ... "

Finally, as it was mentioned, there is no detectable pit in WUA. A possible usage for WUA might have been the disposal of toxic chemicals in small, shallow, sub-meter wide trenches. This size is not big enough to allow accurate seismic detection neither does its construction (absence of magnetic sources) yield enough magnetic anomaly. Figure 9.7 shows the combined seismic models for the whole MDA-B (see also table 9.1).

Table 9.1: Synopsis of trenches dimensions

	Length (ft)	Mean Height (ft)	Width (ft)
1st	324	15	45
2nd	452	14	44
3rd	393	8	52
4rd	295	15	29
5rd	296	16	27

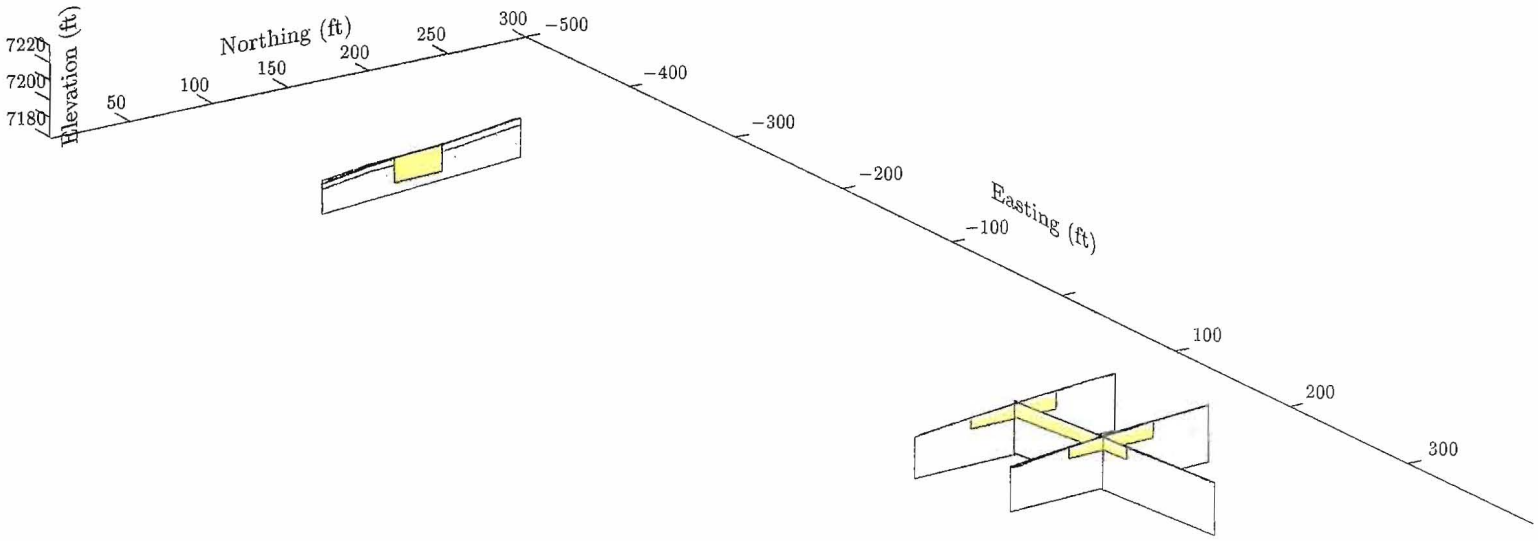

Figure 9.5: Interpreted seismic model for WPA.

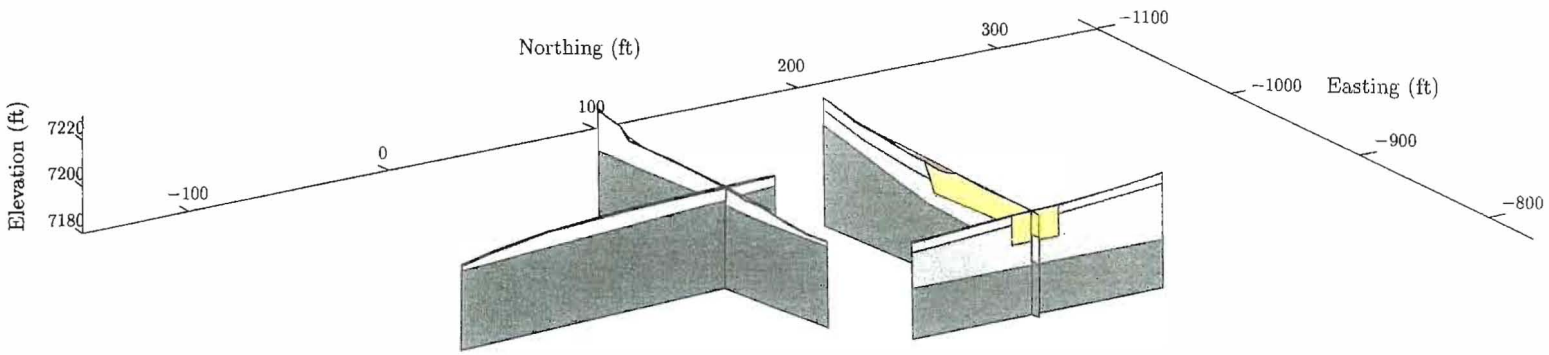

Figure 9.6: Interpreted seismic model for Eastern end WPA and WUA.

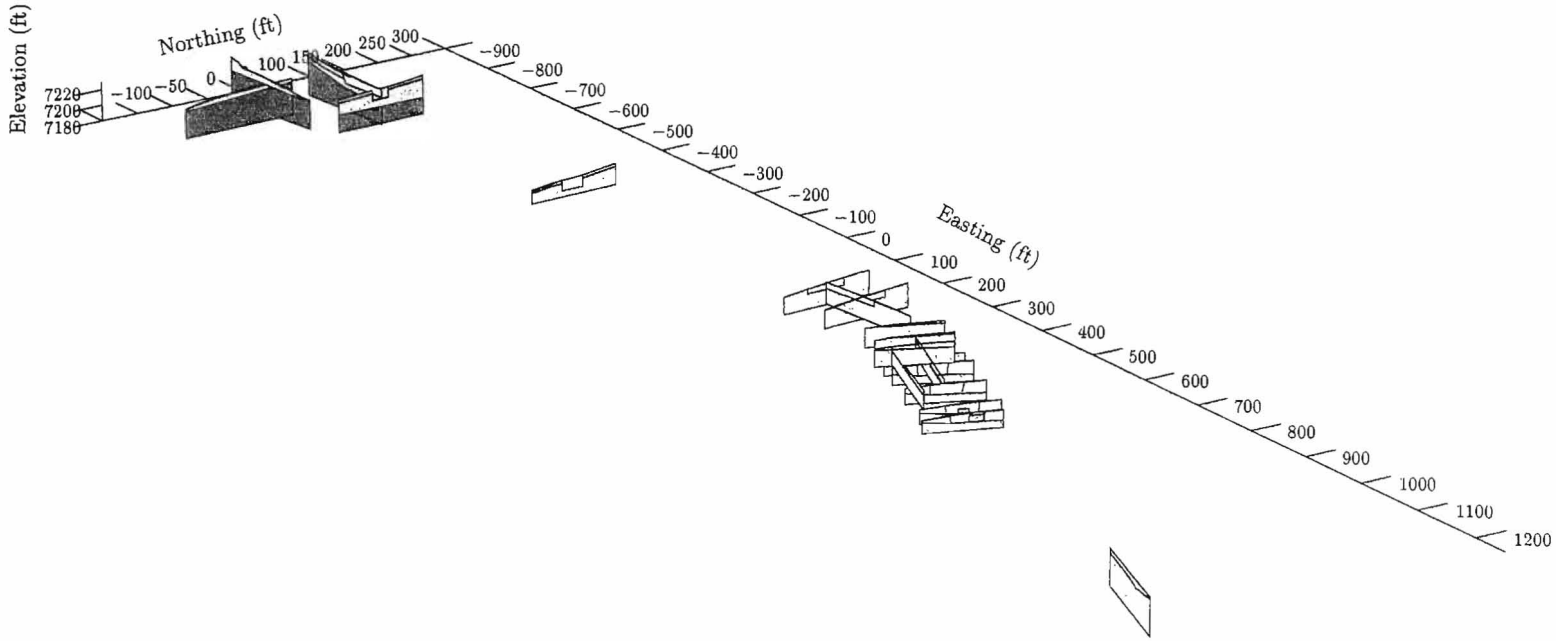

Figure 9.7: Fence diagram of the seismic models at MDA-B (Lines 7-29)

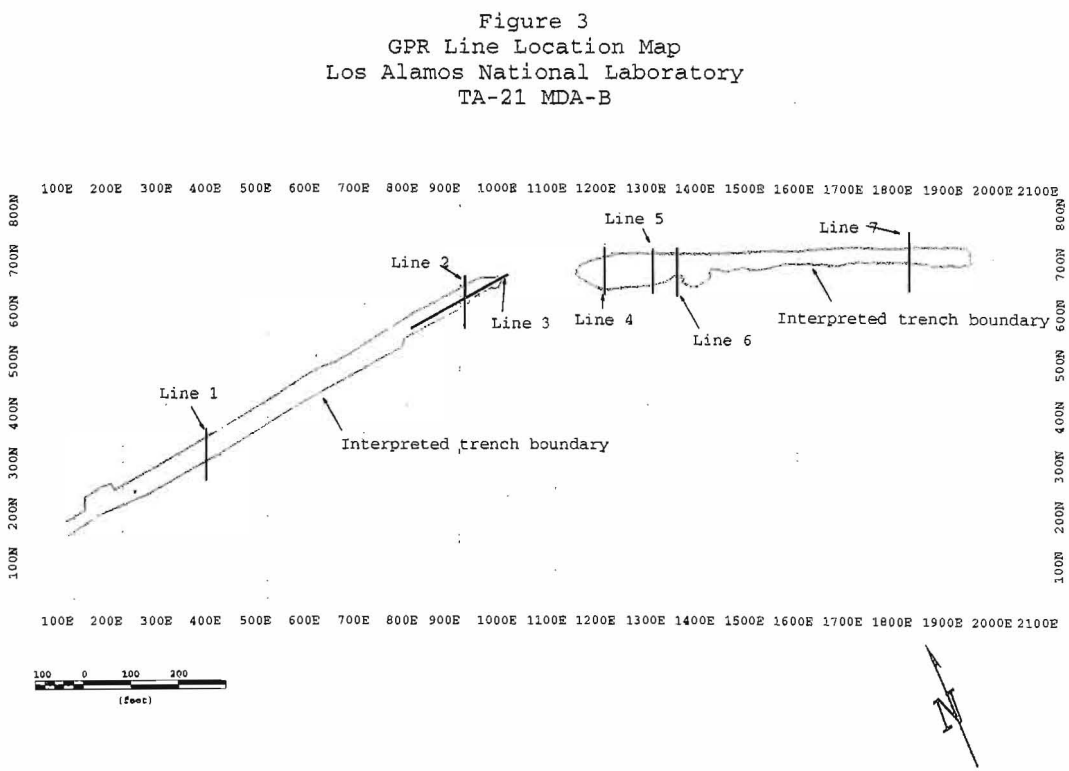

Figure 9.8: BGA interpretation of the trench boundary for MDA-B. Source: BGA report, 1998.

Conclusions-Suggestions

We presented the results from the geophysical investigation done at MDA-B. The main objective of this work was to detect, map and interpret reliably any trench with MDA-B. The survey was initially open to any geophysical method that could probably accomplish this objective. However early on, it was realized that neither seismic reflection nor ground penetrating radar or electromagnetic methods could work properly in this case. As an example we can refer to previous work done in the site by SAGE and BGA (Fig 3.3). The proposed model from BGA for instance (Fig 9.8) lacks the desired resolution and accuracy. The idiosyncrasy of MDA-B and its puzzling content forced the application of other techniques. A reasonable first approach was the acquisition of a magnetic map. The magnetic data then served as a guide for the rest of the survey. It finally proved in practice that seismic refraction can successfully and reliably deal with this situation overcoming all the difficulties mentioned so far. Moreover the models produced from the refraction data helped to constrain the ambiguity of the magnetic interpretation. In figures 9.9 and 9.10 we can see the final constructed models in two and three dimensions correspondingly (trenches 1, 2, 3, 4, 5, and the small square pit (s) next to trenches 1 and 2).

Concluding we can say that:

- Seismic refraction method worked very well in this context. Indeed, seismic refraction can work in difficult situations where many of the other methods may fail.

- Trench dimensions were determined with about 1 m accuracy using mostly seismic refraction data.

- The shape and the number of the trenches was discovered from the shape and the character of the magnetic data. This is partly because of the lack of sufficient refraction data.

- The biggest part of the magnetic anomaly related to the trenches is due to shallow metallic objects (often $1 - 3m$ depth .

Some suggestions that spring from the overall results of this work may concern the furthermore improvement and the applicability of the techniques that have been used. In general the resolution of the seismic refraction method is highly connected with the correct measuring of the first-break arrivals. These, in turn, are affected by the S/N ratio. Any action that may increase this ratio, either during the data acquisition or after in the signal processing tasks could make seismic refraction more popular in the real world. Now, more specific for this survey the main pitfall might be the lack of enough seismic data. Additional seismic lines can be shot to determined all the boundaries of the trenches, especially in the middle of WPA section where we had only one seismic profile. Also we can re-shoot some lines mostly at the EUA where external noise made many lines uselessness for further modeling. Working in a real case problem is not the same as doing laboratory work. Unexpected difficulties, or even considering the ability to acquire high quality data makes this work harder but also more challenging and exciting for the researcher.

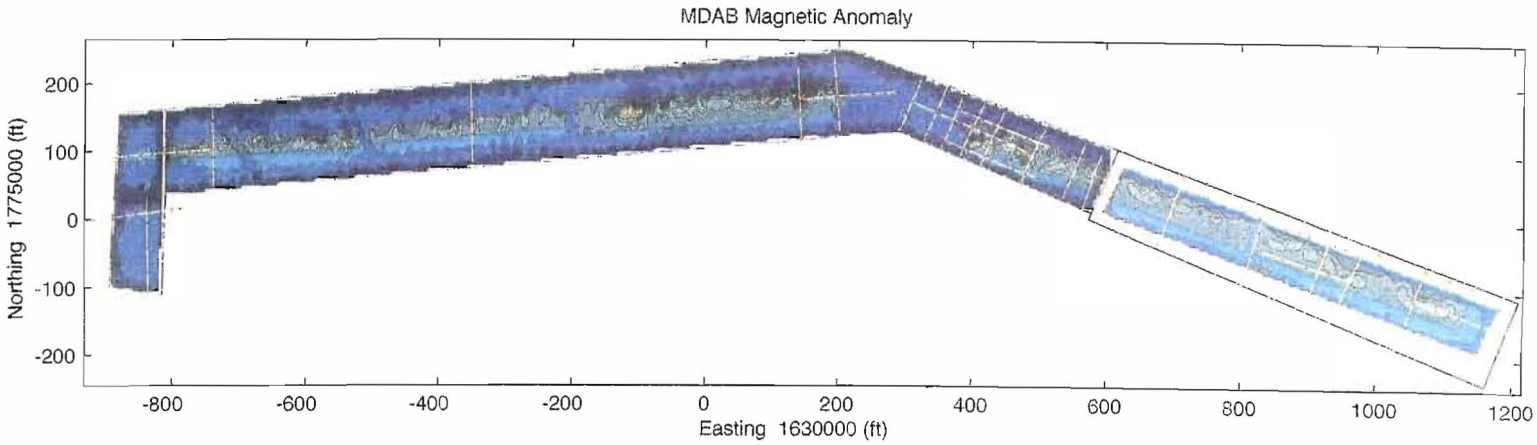

Figure 9.9: Final interpretation of the trench boundaries for MDA-B.

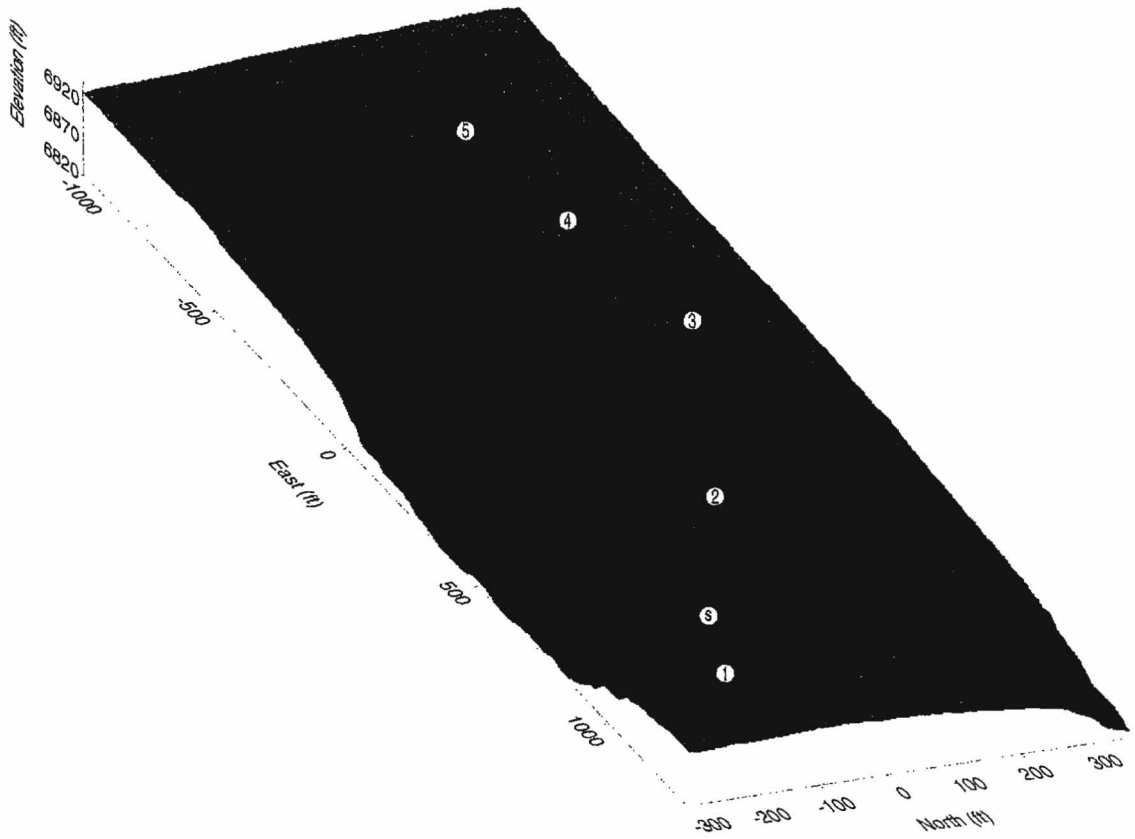

Figure 9.10: Three dimensional perspective view of the trench boundaries for MDA-B.

Appendix A

Matlab code

```
function t=mprism(x0,y0,z0,x1,y1,z1,x2,y2,mi,md,fi,fd,m,thet)
%
% Total-field magnetic anomaly at (x0,y0,z0) due to an infinitely
% extended rectangular prism.
% Sides of prism parallel to x, y, z axes, and z is vertical down.
% Bottom of prism extents to infinity.
% To provide the anomaly of a prism with finite thickness, call the
% mprism two times and set t=t1-t2.
%
%Requires subroutine dircos.  Method from Bhattacharyya (1964).
%Prism at depth z1;it extents from x2-x1, y2-y1, and infinitely downward.
%
% Input parameters:
% mi    : inclination of Magnetization.
% md    : declination of       "
% fi    : inclination of Ambient field.
% fd    : declination of       "
% m     : intensity   of Magnetization (A/m).
% thet: azimuth(declination) of x-axis. (e.g. if thet=0  => x->North
%                                            if thet=90 => y->North)
% Output parameters:
% Total-field anomaly t, in nT .
%
% Units are irrelevant but must be consistent (e.g. m, kg/m^3).
%
% Blakely, R. J., (1995), Potential Theory in Gravity and Magnetic
% Applications, Cambridge, New York.
```

```
% Matlab implementation: Ioannis Thavoris, UTD, Spring 1998.
%
%% Input example:
%%    mi=60.0;md=0.0;fi=60.0;fd=0.0;thet=0.0;m=500.0;
%%    x0=0.0;y0=0.0;z0=0.0;
%%    x1=-0.5;y1=-0.5;z1=1.0;
%%    x2=0.5;y2=0.5;
%
cm = 1.0e-7; t2nt=1.0e9;
%
%
% Call the dircos function to compute direction cosines from
% inclination and declination for Magnetization.
incl=mi;decl=md;azim=thet; [ma,mb,mc]=dircos(mi,md,thet);
%
%ma
%mb
%mc
%
% Call the dircos function to compute direction cosines from
% inclination and declination for Ambient field.
incl=fi;decl=fd;azim=thet; [fa,fb,fc]=dircos(fi,fd,thet);
%    fa=a;fb=b;fc=c;
%
fm1=ma*fb+mb*fa; fm2=ma*fc+mc*fa; fm3=mb*fc+mc*fb; fm4=ma*fa;
fm5=mb*fb; fm6=mc*fc; alpha = [x1-x0,x2-x0]; beta  =
[y1-y0,y2-y0]; h=z1-z0; t=0; hsq=h^2;
%
%
for i=1:2
    alphasq=alpha(i)^2;
    for j=1:2
      sign=1.0;
      if i~=j
         sign=-1.0;
      end
      r0sq=alphasq+beta(j)^2+hsq;
      r0=sqrt(r0sq);
      r0h=r0*h;
      alphabeta=alpha(i)*beta(j);
```

```
      arg1=(r0-alpha(i))/(r0+alpha(i));
      arg2=(r0-beta(j))/(r0+beta(j));
      arg3=alphasq+r0h+hsq;
      arg4=r0sq+r0h-alphasq;
      tlog=fm3*log(arg1)/2.0 + fm2*log(arg2)/2.0-fm1*log(r0+h);
      tatan=-fm4*atan2(alphabeta,arg3)-fm5*atan2(alphabeta,arg4)...
         +fm6*atan2(alphabeta,r0h);
%
      t=t+sign*(tlog+tatan);
%
     end
end t=t*m*cm*t2nt;
%
return
%-----------------------------------------------------------------

function [a,b,c]=dircos(incl,decl,azim)
%
%  Dircos computes direction cosines from inclination and declination
%
% Input parameters
%    incl       :  inclination in degrees; positive below horizontal
%    decl       :  declination in degrees; positive east of true north
%    azim       :  azimuth of x axis in degrees; positive east of north
%
% Output parameters
%    a, b, c    :  the three direction cosines
%
% Blakely, R. J., (1995), Potential Theory in Gravity and Magnetic
% Applications, Cambridge, New York.
% Matlab implementation: Ioannis Thavoris, UTD, Spring 1998.
%
d2rad=0.017453293;
%
xincl=incl*d2rad; xdecl=decl*d2rad; xazim=azim*d2rad;
%
a=cos(xincl)*cos(xdecl-xazim); b=cos(xincl)*sin(xdecl-xazim);
c=sin(xincl);
%
return
%-----------------------------------------------------------------
```

Bibliography

Ackermann, H. D., Pankratz, L. W., and Dansereau, D. (1986). Resolution of ambiguities of seismic refraction traveltime curves. *Geophysics*, 51:223–235.

Banerjee, B. and Gupta, S. K. (1975). The hidden layer problem in seismic refraction work. *Geophysical Prospecting*, 23:642–652.

Belfer, I., Keydar, S., Kravtsov, A., and Landa, E. (1996). Imaging of the shallow subsurface using refracted and diffracted waves. In *Annual Meeting Abstracts*, pages 884–887. Society of Exploration Geophysicists.

Bhattacharyya, B. K. (1964). Magnetic anomalies due to prism-shaped bodies with arbitrary polarization. *Geophysics*, 24:517–531.

Bhattacharyya, B. K. and Leu, L.-K. (1977). Spectral analysis of gravity and magnetic anomalies due to rectangular prismatic bodies. *Geophysics*, 42:41–50.

Blakely, R. J. (1995). *Potential Theory in Gravity and Magnetic Applications*. Cambridge University Press, New York.

Briggs, I. C. (1974). Machine contouring using minimum curvature. *Geophysics*, 39(01):39–48.

Broxton, D. E. and Eller, P. G. (1995). Earth Science Investigations for Environmental Restoration - Los Alamos National Laboratory Techical Area 21. *Los Alamos National Laboratory, NM,* LA-12934-MS, UC-903.

Broxton, D. E., Heiken, G. H., Chipera, S. J., and Byers, F. M. (1995). Stratigraphy, Petrography, and Mineralogy of Bandelier Tuff and Cerro Toledo Deposits. *Earth Science Investigations for Environmental Restoration - Los Alamos National Laboratory,* NM, LA-12934-MS, UC-903.

Dobrin, M. B. and Savit, C. H. (1988). *Introduction to geophysical prospecting.* McGraw-Hill Book Co., New York.

Dudgeon, D. E. and Mersereau, R. M. (1984). *Multidimentional digital signal processing.* Prentice Hall, NJ.

Ferguson, J. F., Baldridge, W. S., Jiracek, G. R., Conzalez, V., and Pope, P. A. (1998). An Investigation of a Los Alamos National Laboratory, New Mexico,Environmental Restoration Site by the SAGE Field Course . *Eos, Transactions, American Geophysical Union,* 1998, pages 329–335.

Ferguson, J. F., Cogbill, A. H., and Warren, G. (1994). A geophysical-geological transect of the Silent Canyon caldera complex, Pahute Mesa, Nevada. *Journal of Geophysical Research*, 99(B3):4323–4339.

Gerard, A. and Debeglia, N. (1975). Automatic three-dimentional modeling for the interpretation of gravity or magnetic anomalies. *Geophysics*, 40:1014–1034.

Goff, F. (1995). Geologic Map of Technical Area 21. *Earth Science Investigations for Environmental Restoration - Los Alamos National Laboratory,*NM LA-12934-MS, UC-903.

Green, A., Lanz, E., Maurer, H., and Boerner, D. (1999). A template for geophysical investigations of small landfills. *The Leading Edge*, 18(2):248–254.

Green, A. G., Lanz, E., and Maurer, H. (1998). Refraction tomography over a buried waste disposal site. *Geophysics*, 63(04):1414–1433.

Green, R. (1962). The hidden layer problem. *Geophys. Prosp.*, 10(02):166–170.

Green, R. (1974). The seismic refraction method-a review. *Geoexploration*, 12:259–284.

Greenhalgh, S. (1977). Comments on "the hidden layer probem in seismic refraction work. *Geophysical Prospecting*, 25:179–181.

Izett, G. A. and Obradovich, J. D. (1994). $^{39}Ar/^{40}Ar$ age constraints for the Jaramillo Normal Subchron and the Matuyama-Brunhes geomagnetic boundary. *Journal of Geophysics Research*, 99:2925–2934.

Kaufman, A. A. (1992). *Geophysical Field Theory and Magnetic Fields.* Academic Press.

Kellogg, O. D. (1953). *Foundations of Potential Theory.* Dover, New York, NY.

Lankston, R. W. (1990). *High Resolution Refraction Seismic Data Acquisition and Interpretation.* Investigations in Geophysics, Volume 5. SEG, Tusla, OK.

Lankston, R. W. and Lankston, M. M. (1986). Obtaining multilayer reciprocal times through phantoming. *Geophysics*, 51:45–49.

Lanz, E., Maurer, H., and Green, A. G. (1997). Characterization of a composite landfill: A multidisciplinary approach. In *Annual Meeting Abstracts*, pages 776–779. Society Of Exploration Geophysicists.

Mateeva, A. (2000). Estimating the influence of random noise on picked traveltimes. Center of Wave Phenomena, CWP-344 Annual Project Review 2000, Colorado School of Mines, Golden, CO.

McQuown, M. S. (1998). Results of Integrated Geophysical Investigation, Los Alamos National Laboratory, Report to LANL.

Naidu, P. S. and Mathew, M. P. (1998). *Analysis of geophysical potential fields.* Advances in Exploration Geophysics 5. Elsevier, Amsterdam-Lausanne-New York-Oxford-Shannon-Singapore-Tokyo.

Nyhan, J. and Barnes, F. (1989). Development of a prototype plan for the effective closure of a waste disposal site in Los Alamos, New Mexico. *Los Alamos National Laboratory, NM,* LA-11282-MS, UC-721.

Nyhan, J. W., Hakonson, T. W., and Lopez, E. A. (1986). Corrective Measures Technology for Shallow Land Burial at Arid Sites: Field Studies of Biointrusion Barriers and Erosion Control. *Los Alamos National Laboratory, NM,* LA-10573-MS, UC-708.

Parasnis, D. S. (1986). *Principles of Applied Geophysics.* Chapman and Hall, London.

Peters, L. J. (1949). The direct approach to magnetic interpretation and its practical application. *Geophysics*, 14:290–320.

Pope, P. A., Eeckout, E. V., Rofer, C., Baldridge, W. S., Ferguson, J. F., Jiracek, G. R., Balick, L., Josten, N., and Carpenter, M. (1996). Environmental waste side characterization utilizing aerial photographs, remote sensing and surface geophysics. *Nuclear Hazardous Waste Managment International Meeting: Spectrum '96, Seattle, WA.*

Press, F. and Dobrin, M. (1956). Seismic wave studies over a high speed surface layer. *Geophysics*, 21:285–298.

Purtymun, W. D. and Kennedy, W. R. (1966). distribution of moisture and radioactivity in the soil and tuff at the contaminated waste pit near Technical Area 21, Los Alamos National Laboratory, NM. *U.S. Geological Survey open file report* 1966.

Reneau, S. L. (1995). Geomorphic studies at DP Mesa and vicinity. *Los Alamos National Laboratory, NM,* LA-12934-MS, UC-903.

Rogers, M. A. (1977). History and Environmental Setting of LANL Near-Surface Land Disposal Facilities for Radioactive Wastes Area A, B, C, D, E, F, G, and T. *Los Alamos National Laboratory, NM,* 1977.

Schneider, W. A., Ranzinger, K. A., Balch, A. H., and Kruse, C. (1992). A dynamic programming approach to first arrival traveltime computation in media with arbitrarily distributed velocities. *Geophysics*, 57:39–50.

Scott, J. H. (1973). Seismic refraction modeling by computer. *Geophysics*, 38:271–284.

Smith, D. N. and Ferguson, J. F. (2000). Constrained inversion of seismic refraction data using the controlled random search. *Geophysics*, (13):1622–1630.

Smith, R. L. and Bailey, R. A. (1966). The Bandelier Tuff, A study of ash-flow eruption cycles from zoned magma chambers. *Bulletin of Volcanology*, 29:83–104.

Spector, A. and Grant, F. S. (1975). Statistical models for interpreting aero-magnetic data. *Geophysics*, 40:1014–1035.

Steeples, D., Green, A., McEvilly, T., Miller, R., Doll, W., and Rector, J. (1997). A workshop examination of shallow seismic reflection surveying. *The Leading Edge*, 16:1641–1647.

Talwani, M. (1965). Computation with the help of a digital computer of magnetic anomalies caused by bodies of arbitrary shape. *Geophysics*, 30:799–817.

Telford, W. M., Geldart, L. P., and Sheriff, R. E. (1996). *Applied Geophysics.* Cambridge University Press, New York.

Tewari, H. C., Dixit, M. M., and Murty, P. R. K. (1995). Use of traveltime skips in refraction analysis to delineate velocity inversion. *Geophysical Prospecting*, 43:793–804.

Whiteley, R. and Greenhalgh, S. (1979). Velocity inversion and the sallow seismic refraction method. *Geoexploration*, 17:125–141.

Wohletz, K. H. (1995). Measurament and analysis of rock fractures in the Tshirege member of the Bandelier Tuff along Los Alamos Canyon adjacent to TA-21. *Earth Science Investigations for Environmental Restoration - Los Alamos National Laboratory,* NM, LA-12934-MS, UC-903.

Zurflueh, E. G. (1967). Applications of two-dimensional linear wavelength filtering. *Geophysics*, 32:1015–1035.

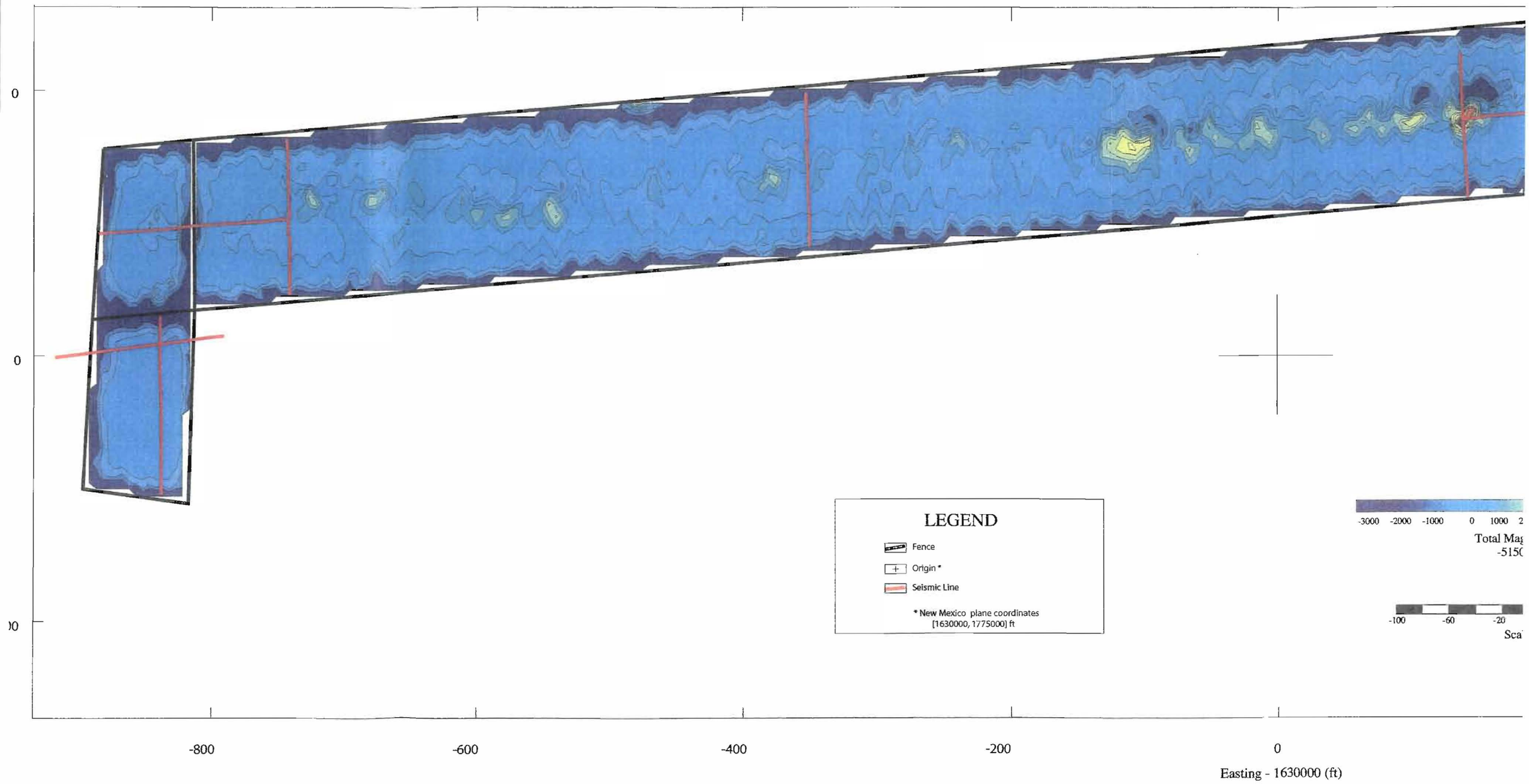
0
0
00
-800
-600
-400
-200
0
Easting - 1630000 (ft)
LEGEND
Fence
Origin *
Seismic Line
* New Mexico plane coordinates
[1630000, 1775000] ft
-3000 -2000 -1000 0 1000 2
Total Mag
-5150
-100 -60 -20
Sca

Magnetic Anomaly Map

TA-21 MDA-B
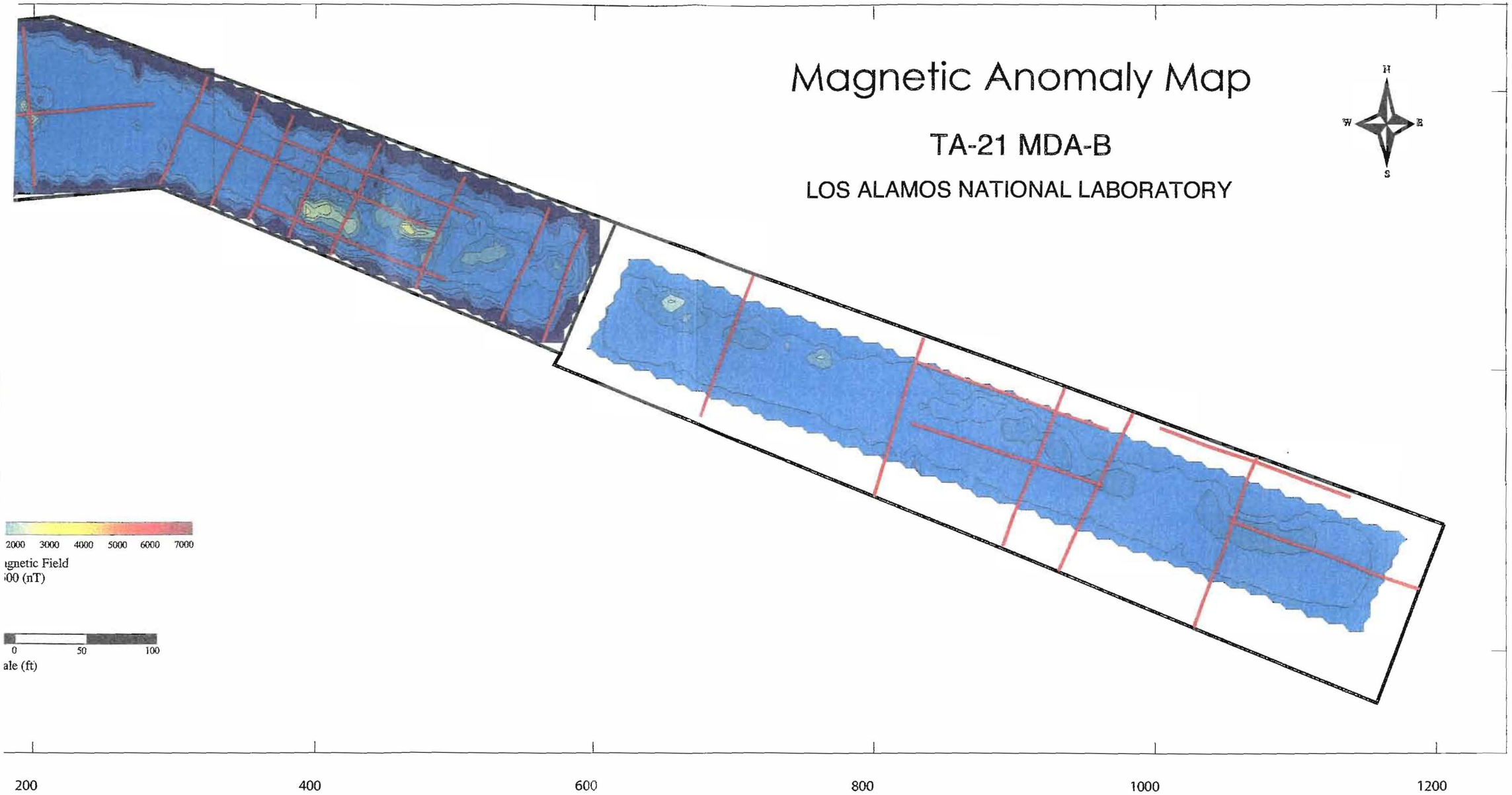
LOS ALAMOS NATIONAL LABORATORY